A FIRST PRINCIPLES BASED APPROACH TO STABILIZE Cu_2S FOR EFFICIENT SOLAR ABSORBER MATERIAL

By

Sajib Kumar Barman

Presented to the Faculty of the Graduate School of

The University of Texas at Arlington in Partial Fulfillment

of the Requirements

for the Degree of

DOCTOR OF PHILOSOPHY

THE UNIVERSITY OF TEXAS AT ARLINGTON

May 2019

Acknowledgements

First, I would like to express my sincere gratitude to my advisor, Professor Muhammad Nurul Huda for guiding me throughout my time at The University of Texas at Arlington. I appreciate his patience for my work and encouraging me to continue my research even at my toughest times.

I would like to thank my committee members, Professor Ali R. Koymen, Professor Qiming Zhang, Professor Suresh C. Sharma, and Professor Raymond Atta-Fynn for their interests in my research work and supporting me to carry out my research.

I also would also like to thank the previous and current members of our research group Dr. Pranab Sarker, Dr. Cedric Mayfield (late), Dr. Sarah Christine Hernandez, Dr. Shafaq Amdani Moten, Mr. Prashant Khatri, Mr. Hori Pada Sarker, Mr. Edan Bainglass, Mr. Hussain Jabreel Alathlawi, and Ms. Noura Dawas Alkhaldi for being very helpful throughout my research work. Their valuable suggestions were intriguing and helped me in many ways to broaden my research experience.

I am grateful to the Department of Physics of The University of Texas at Arlington for the support I have received as a graduate student. I thank our Chair Professor Alex Weiss for his encouragement and continuous support. I am thankful to all our physics office staffs, specially Ms. Stacey Cody, Ms. Holly Zander, Ms. Nieshea Crow, and Mr. Victor Reece for their administrative support, and Dr. Suman Satyal for being a supportive lab coordinator.

I would like to thank National Renewable Energy Laboratory for the support to initiate this work on Cu_2S, and National Science Foundation for funding later to keep this project going on.

I am very grateful to my parents and siblings for supporting me with their best to complete my post graduate studies abroad. Last but not the least, I am very much thankful to my wife, Shuvra Sarker for her commitment to keep me in track for the completion of my doctoral degree.

April 20, 2019

This work is dedicated to my loving wife, Shuvra Sarker,
to my parents, Shafali Barman and Subal Barman,
and to my siblings, Sathi and Joydev.

Abstract

A FIRST PRINCIPLES BASED APPROACH TO STABILIZE Cu_2S FOR EFFICIENT SOLAR ABSORBER MATERIAL

Sajib Kumar Barman, PhD

The University of Texas at Arlington, 2019

Supervising Professor: Muhammad Nurul Huda, Ph.D.

Cu_2S is an important low-cost, earth-abundant and non-toxic material which has shown its potential in the field of photovoltaics. Experimentally known band gaps of this material vary between 1.1-1.2 eV, which are suitable for applications in photovoltaics as solar light absorbers. Cu_2S based thin film solar cells showed nearly 10% efficiency in the past. However, it exhibits complex phase behavior; Cu_2S can be found in several different phases depending on its Cu-deficiency in the structures. In general, all the phases of this material suffer from spontaneous Cu-vacancy formations and Cu-diffusions in the crystal. The excessive or uncontrollable vacancy formation in the crystal structure makes the material to behave as a degenerate semiconductor. As a result, the performance of Cu_2S based thin film solar cells deteriorates at ambient conditions over the time. To make efficient use of this material, reduction of Cu-vacancy formation and Cu-diffusion inside the crystal are the two most important challenges at the present.

Out of all the experimentally known phases, low chalcocite is the most stable stoichiometric phase at or below room temperature. Recently, density functional theory-based crystal database search has revealed a new stoichiometric phase, acanthite, which has higher thermodynamic stability in the ground state than the low chalcocite. In this work, we have found from room temperature molecular dynamics calculations, that these two have similar features in their crystal structures up to several nearest neighbor distances. Also, the electronic signatures of acanthite and low chalcocite Cu_2S are comparable. Hence in this work we have argued that, instead of low chalcocite, the acanthite phase can be, in fact, used to model complex alloying of Cu_2S since it has a simpler crystal structure and would serve for cost-effective computational studies.

We present density functional theory (DFT) based systematic studies on Ag and Sn doping in the both acanthite and low chalcocite phases of Cu_2S. We show that Ag or Sn doping in Cu_2S is thermodynamically favorable and can help to reduce the vacancy formation probability. The diffusion-energy barrier calculation reveals that an Ag atom doped at a Cu place can help to control Cu^{1+} ion diffusion inside the crystal. Ag:Cu_2S band structures show that Ag doping increases the band gap by a favorable amount, which may help to maximize the photo-conversion efficiency. To further compensate the formation of Cu vacancies, we looked for another alloying element. After a several elemental-searches by DFT calculations, we have decided on Sn. For Sn doped Cu_2S, we show that Sn introduces defect states at or near the Fermi level in band structures. However, such Sn doping effects can be compensated with suitable Cu-vacancies in the crystal. Finally, from the chemical potential landscape analyses, the results reported here show that the Cu_2S can be stabilized with Ag or Sn doping.

Table of Contents

List of Illustrations

List of Tables

Chapter 1

Introduction

1.1 Addressing Global Warming and Pacifying with Clean and Renewable Energies

It is evident that energy consumption has a direct correlation to the advent of civilization. To meet the accelerating need of energy consumption every year, fossil fuels such as petroleum, natural gas, and coal are the primary sources as of now. According to U.S. energy information administration, more than 78% of energy resources in U.S. is derived from fossil fuel [1], which eventually results in detrimental global warming and hence the climate change. As evident, climate change has direct damaging impacts on earth environment [2,3], and the health of global population, other living organisms and overall economic growth of the world [4–8]. As a result, replacing fossil fuel is of utmost importance to save the planet Earth and its living bodies.

Following the determination to alleviate Earth's deteriorating health, an urgent need triggered decades ago to find replacements with clean and renewable energies. The most commonly known clean and renewable energies are solar energy, wind power, hydroelectric energy, biomass, hydrogen storage and fuel cell, and geothermal power. Out of these, the sun light is the most abundant in nature. Hence making use of it can be the best way to not only meet global energy demand but also to pacify damaging effects of climate change. Two of the popular ways for harnessing solar energies are direct solar-to-electricity and solar-to-hydrogen productions, where the technologies involved in these

cases are known as photovoltaics (PV) and photo electrochemical (PEC) water splitting, respectively. Under ambient sun light conditions, efficient solar absorber materials with suitable energy band gaps are necessary to be used in either PV or PEC cell for maximum device performance. Since PV cells converts sun light directly to electricity which can be fed to external circuit for direct usages, as of now, it is only feasible for the daytime. On the other hand, hydrogen produced by PEC cells can be stored and are available for usages in the hours of darkness. According to National Renewable Energy Laboratory (NREL) of USA, right now the record solar to electricity conversion efficiency for multijunction PV cell is 46%, whereas for single-junction GaAs thin film solar cell it is 29.1%. For the single junction PV cell, this efficiency is close to the limiting theoretical value of 30% at energy band gap of 1.1 eV, known as Shockley-Queisser limit [9]. More recent calculations show that this efficiency limit is 33.7% at energy band gap of 1.34 eV [10,11] under solar illumination with the AM 1.5G spectrum. For PEC cells, analogous calculations for such detailed balance limit are not very straight forward due the complex and multicomponent nature of devices. Several approaches and simulations were attempted [12–18], where a study has concluded that the limiting efficiency for an ideal single junction PEC device is 30.6% at a bandgap of 1.59 eV under solar illumination with the AM 1.5G spectrum [12]. Even though PEC cells have sought cheap hydrogen fuel productions due to high conversion efficiency, its commercialization as of now is far from reality while its counterpart, PV cells are dominating solar cell markets. Note that, the technologies involved in the scenario must consider cost-effectiveness so that commercial operations can be affordable and distributed easily for consumption. Therefore, our goal here is to devote on the aspects of PV cells, particularly studying and

tuning quantum mechanical properties of cost effective, Earth abundant and non-toxic solar absorber materials for maximum photoconversion efficiency. In general, fundamental electronic properties that we will be addressing in this work can be equally applicable to the similar class of solar absorber materials for PEC water splitting, albeit for PEC application the absorbers will be subjected to additional electronic criteria [19].

1.2 Principle of a PV Cell

A typical single junction photovoltaic cell as in Figure 1. 1, is made when a p-type and an n-type material are brought together, and a p-n junction is formed. At this junction, electrons from n-type side diffuse to p-type side. Similarly, holes from p-type side diffuse to n-type side. This diffusion of electrons and holes in opposite direction creates a thin layer of space charge region or depletion layer that sets an electric field from n- to p- type side of the junction. When light falls on the cell, photons from the sun light excite electrons from the valence band to the conduction band in the semiconductor. For efficient absorption of sunlight, the band gap of the semiconductor should match the visible light energy range where the sun's energy output is maximum on earth. This impose a maximum limit on the band gap of the semiconductor, which is about 1.5 eV. The electron-hole pairs created by light absorption in both sides of the cell as can be seen in Figure 1. 2. These electron-hole pairs are then induced to separate by the electric field set across the depletion region. Hence, electrons can be collected to the cathode and holes to the anode and fed to a circuit with a load. This is how electric current is generated in a PV cell.

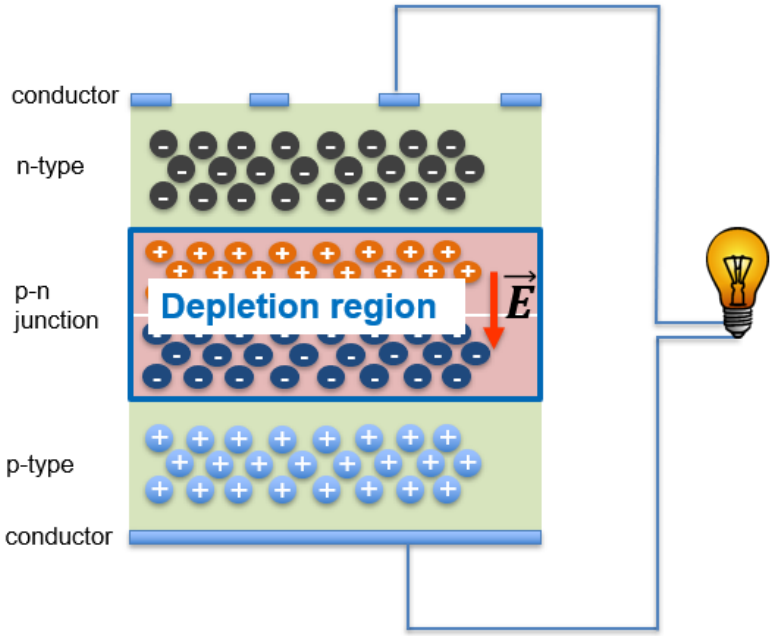

Figure 1. 1 A schematic of a single junction photovoltaic (PV) cell.

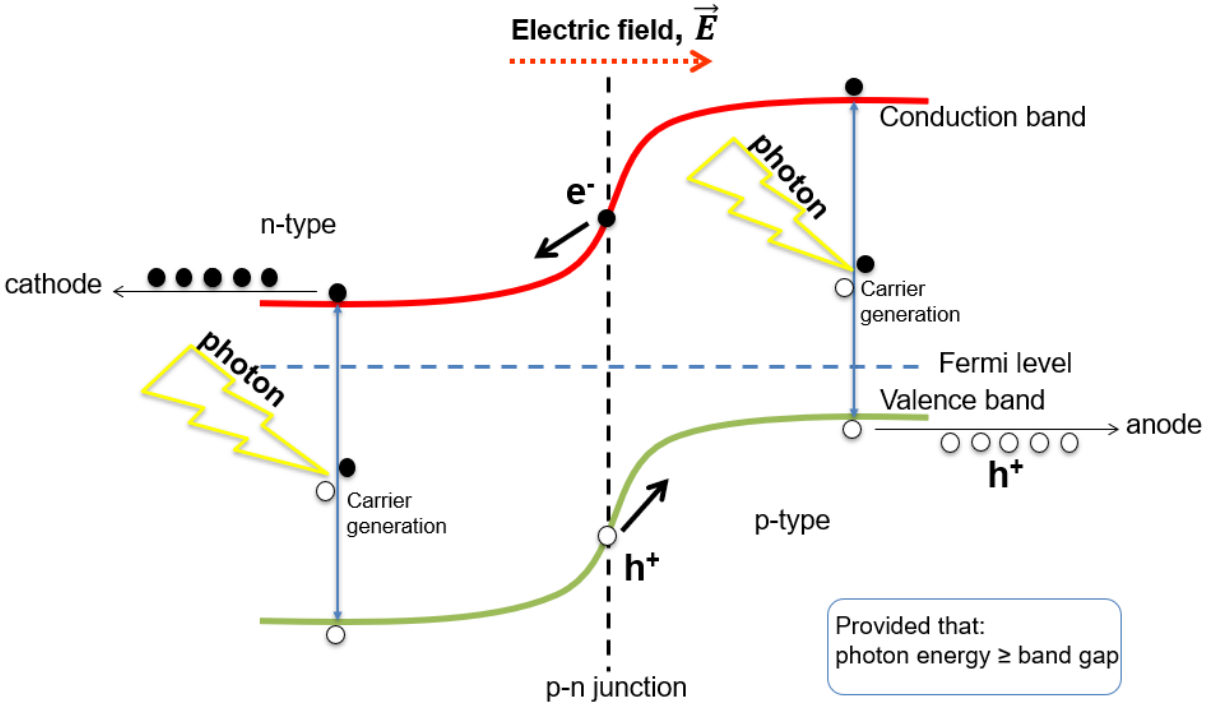

Figure 1. 2 A schematic of the band diagram of a single p-n junction PV cell.

1.3 Prospects and Challenges with PV materials

Currently, Si based solar cells, with a band gap of 1.1 eV, dominate 90% of the PV market. But pure grade Si is not as cost-effective as to meet global demand even though c-Si based single p-n junction solar cell has shown efficiency close to 27% [20]. Other efficient materials such as $Cu(In,Ga)(S,Se)_2$ and $Cu_2ZnSn(S,Se)_4$, respectively, both regarded as prominent solar cell absorbers, have shown nearly 20% [21] and 12.6% [22] efficiency, respectively for solar-light-to-electricity production. However, Ga and In are relatively less abundant and more expensive. On the other hand, CZTS based thin film solar cells previously emerged as a cost-effective alternative since Cu, Sn, and Zn are Earth abundant. However, pure and defect-free synthesis of CZTS is quite challenging. Similar ionic radii and tetrahedral coordination of Cu and Zn lead these cations swap their lattice sites in the crystal structures. With any of these defects single phase synthesis of CZTS is thermodynamically not possible [23]. Furthermore, high temperature synthesis procedures introduce defects to the crystal and electronic structures which eventually result in low device performance [24]. Stabilizing CZTS by adding more dopants in the crystal does not meet the overall device efficiency as well. Attempts to lessen such imperfections by doping Ba at Zn site previously showed evidence of controlling coordination environment in the chalcogenide family $BaCu_2SnSe_xS_{4-x}$ (BCTSSe), but the resulting conversion efficiency does not meet expectation [25]. Hence, it is necessary to examine closely the Cu^{+1} based materials to understand their stability, and design complex materials from the scratch. In that context, two such basic materials are Cu_2O

and Cu_2S. These are also two promising solar-absorber materials owing to their suitable band gaps, low cost synthesis process, non-toxicity and Earth abundance [26,27].

Cu_2O has been utilized as a light-absorbing layer due to its 2.1 eV band gap resulting in power conversion efficiencies of ~5 % [28] for heterojunction solar cells even though efficiencies of Cu_2O Schottky-barrier solar cells are less than 1 % [29]. However, the theoretical conversion efficiency can reach up to 22% according to Shockley-Queisser's detailed balance limit [9]. Cu_2O has a very low Cu-vacancy formation energy and can usually form two types of Cu vacancies; one with more localized state (split vacancy) another with delocalized state (simple vacancy) over the Fermi level, even though a previous theoretical calculation concluded that both defects are localized in nature. Cu_2S has a much favorable direct band gap of 1.2 eV and has shown nearly 10% [30] solar-to-electricity conversion efficiency for single junction solar cells. Interestingly, both Cu_2O and Cu_2S are known as p-type materials due to Cu vacancies formations. However, in Cu_2S split-vacancies for Cu have not been reported so far. It was found that Cu vacancies are thermodynamically favorable to form at both Cu rich and poor conditions [31–36]. In addition, uncontrollable Cu diffusion in Cu_2S crystals makes the solar cell device performance to degrade over long time. Also, naturally occurring minerals of Cu_2S have complex crystal structures and very low symmetry for Cu ions in the systems. Due to the Cu vacancy formation tendency and diffusion in the system, various non-stoichiometric $Cu_{2-x}S$ phases are also available. Out of all the experimentally known phases of Cu_2S, low chalcocite is the most stable one in room temperature. Recently, a relatively simple phase of Cu_2S is identified by crystal database search and computational modeling, which has acanthite like crystal structure and thermodynamically

more favorable than low chalcocite in the ground state [37]. The discovery of this acanthite like crystal structure of Cu_2S provides wider access to model complex low chalcocite phase leading to easier pathways to alloy other materials at Cu sites and search for favorable alloyed crystals with lower Cu vacancy formation tendency and suitable electronic structures.

1.4 Literature Review on Cu_2S and its limitations in PV application

Cu_xS ($1 \leq x \leq 2$) exits in various mineral forms. There exist four different crystalline phases below 90°C which are known as low chalcocite (Cu_2S) [38,39], djurleite ($Cu_{1.96}S$) [40], digenite ($Cu_{1.8}S$) [41], and anilite ($Cu_{1.75}S$) [42]. This material also exists in a solid-liquid hybrid form above 104°C, which is called high chalcocite or hexagonal phase [43], and at cubic phase above 436°C. Out of all the experimentally known phases, low chalcocite is the most stable stoichiometric phase at or below room temperature [35,36]. Both experimental and theoretical band gaps of this phase was reported close to 1.2 eV [35] that resulted theoretically calculated single-junction PV efficiency based on this material more than 30% [35,44–46]. However, experimentally it was observed that the spontaneous Cu vacancy formation transformed the stoichiometric phase to a heavily p-doped (Cu-deficient) djurleite phase ($Cu_{1.96}S$) and led to low device performance [47]. An estimated free carrier concentration in such case is more than 10^{20} cm^{-3} [48]. A relatively new report also shows high hole concentrations in Cu_2S thin film grown by atomic layer deposition, which can be of the order of 10^{21} cm^{-3} [49]. Transformation to different Cu deficient phases eventually introduces defects in the electronic structures and therefore low photo-absorption. In that case, maintaining p-type

doping level in this material is of utmost importance. With the advancement of sophisticated synthesis processes and the state-of-the-art theoretical methodologies, it is becoming easier to find routes for dealing such situations now a days. As a result, interest in this material for efficient and stable applications in photovoltaics is increasing again [48,50–55]. A recently published study by Riha *et al* has presented a promising experimental mechanism to stabilize Cu_2S one atomic layer at a time by inserting a single layer of Al_2O_3 in between Cu_2S and TiO_2 thin films. The study also reported significantly reduced carrier concentration in that process under ambient condition [56]. Since the formation of stable $Cu_{2-x}S$ film is a difficult task, development of different techniques for stabilization are ongoing, among these a recent publication reported that elemental stacked layer deposition method is one of the useful one for growing nanostructured Cu_2S film for photovoltaic application [50]. That study reported crystalline Cu_2S formation for multilayer thin film grown on glass substrate by physical vapor deposition with band gaps 1.65 to 1.85 eV. Besides, economical synthesis process for Cu_2S thin film by chemical bath deposition technique with 1.94 eV band gap is also being reported [57]. Since, historically, Cu_2S has been used in thin film photovoltaic devices, such reports are very hopeful for the PV application of this material. Thimsen *et al* reported that a nonthermal plasma process used to synthesize Cu_2S nanocrystals were stable in the ambient for more than two months [58]. In addition to stabilizing Cu_2S crystals, there has been efforts beyond thin film solar cells, such as core−shell nanorod array devices based on CdS-Cu_2S, which show power conversion efficiencies up to 3.8% with promising stability in air [59]. However, a comprehensive study on the diffusion kinetics of Cu ions inside the material has not been done yet either experimentally or theoretically although several

recent theoretical studies have been attempted on the crystal phase stabilities and electronic structure properties of Cu^{+1} based materials, particularly on binary compounds for higher stabilization, enhanced quantum mechanical properties [60–69], where very few of these contain studies on the low chalcocite phase [35–37]. Alongside the studies on the bulk phases, interest on the 2D-monolayer aspect of this material is emerging [68,70]. One such 2D-monolayer, named as δ-Cu_2S was reported by Guo *et al*, which showed 1.26 eV direct band gap, high electron mobility of up to 6880 $cm^2 V^{-1} s^{-1}$ and promising oxidation resistance. However, the energy band gap of this material shows significant quantum size effect. The hybrid functional calculated band gap decreases significantly with increasing number of layers, and the bulk phase of that does not have any band opening [68]. Since low chalcocite is an Earth abundant mineral, understanding this material thoroughly and hence figuring out pathways to control its intrinsic properties still warrant more attention before moving on completely to other phases and dealing with their difficult synthesis processes. It is evident that substitutional or interstitial doping can tune the quantum mechanical properties of materials, which have already been observed both for Cu_2X (X= S, Se, Te) as well [61–65,67], These studies also confirm that density functional theory (DFT) based first-principles calculations are quite capable to simulate not only experimental findings but also predict many of the important features to lessen experimental costs. However, it is important to note that DFT sometimes underestimates the band bags of semiconductors but adding on site Coulomb interaction with available post DFT methods, such as DFT + U are good enough for almost accurate description of the band structures for Cu-chalcogenides [71].

1.5 Goal of this Work

As mentioned above, Cu_2S suffers from spontaneous Cu-vacancy formation and diffusion in the crystal, which transform this p-type material to a degenerate semiconductor leading to deteriorating device performance in the long run, our goal is to reduce Cu vacancy formation in the crystal and control the diffusion of vacancy forming Cu ions. The strategy adopted in this work is to alloy Ag in the theoretically predicted acanthite structure of Cu_2S and search for thermodynamically favorable alloyed structures, calculating their Cu vacancy formation energies and diffusion barrier. Afterwards, to complement Ag alloying we searched for several other alloy strategies. Since one of our goal is to look for cost-effective alloying, we then employ similar studies with Sn doping at Cu sites, as substitutional doping of Sn showed the promise to compensate the Cu-vacancies effectively. In addition, we compared the outcomes with doping in low chalcocite crystals for comparative assessments.

In the following chapters, required methodologies and systematic studies are presented. In chapter 2, the density functional theory which is the theoretical framework of this work is discussed briefly. In chapter 3, the stability enhancement mechanism of Ag alloyed acanthite Cu_2S is presented in detail. Following this, thermodynamic and electronic structure calculations for Sn alloyed Cu_2S is discussed in chapter 4 with a view to finding a cost-effective alternative than Ag, which would result similar stability enrichment in Cu_2S crystals with suitable electronic properties for photovoltaic applications. In chapter 5 and 6, an overall conclusion and future direction of this work are given, respectively.

Chapter 2

Methodology

2.1 Density Functional Theory

Density functional theory (DFT) is the theoretical framework of this work and implemented with state-of-the-art simulation package "VASP" in supercomputing systems at Texas Advanced Computing Center (TACC) in Austin, TX.

It is one the most successful theory now-a-days and has been implemented for more than last two decades to study the electronic and crystal structures of condensed matter. More than 15000 publications are being published each year within the DFT framework all over the scientific communities [72]. In the following sections, the density functional theory will be discussed briefly.

2.1.1 Introduction

The most fundamental and accurate study of matter is the key to the understanding of the condensed matter or solid-state physics. This type of study can lead to the discovery of the intrinsic properties of condensed matter and the effect of various type of defects. Density functional theory (DFT) is such a tool which can help to the field of study where researchers have been using this for nearly last two decades successfully. Presently, it is the most successful and promising approach to compute the electronic structure of matter. However, its applicability ranges from atoms, molecules and solids to nuclei and the quantum and classical fluids. Its key entity is the electron density and this theory is designed to provide the ground state properties of materials. For example, DFT

predicts a great variety of molecular properties: molecular structures, vibrational frequencies, atomization energies, ionization energies, electric and magnetic properties, reaction paths, and so many other properties related to the basics of condensed matter physics, chemistry and other related engineering fields. Also, this theory originally has been generalized to deal with many different situations: spin polarized systems, multicomponent systems such as nuclei and electron hole droplets, free energy at finite temperatures, superconductors with electronic pairing mechanisms, relativistic electrons, time-dependent phenomena and excited states, bosons, molecular dynamics, etc.

The original work of density functional theory was pictured on two papers by Hohenberg and Kohn, and Kohn and Sham published on 1964 and 1965 respectively.

Two original papers of DFT

- Inhomogeneous Electron Gas, P. Hohenberg and W. Kohn, Phys. Rev. 136, B864 (1964).
- Self-Consistent Equations Including Exchange and Correlation Effects, W. Kohn and L.J. Sham, Phys. Rev. 140, A1133 (1965).

2.1.2 The Many-Particle Problem

The most important problem in the field of condensed matter theory is to deal many-particle systems within quantum mechanical scheme. Density functional theory deals with such large systems of interacting particles and provides mathematical scheme to solve the relevant many-particle Schrödinger equations. A typical Schrodinger equation of a system of atoms and molecules is

$$\mathcal{H}\Psi = \mathcal{E}\Psi \tag{2.1.1}$$

Where the Hamiltonian in non-relativistic case can be written as

$$\begin{aligned}\mathcal{H} = & \frac{-\hbar^2}{2}\sum_I \frac{\nabla_I^2}{M_I} \\ & + \frac{1}{2}\sum_{I\neq J}\frac{z_I z_J e^2}{4\pi\epsilon_0|R_I - R_J|} \\ & -\frac{\hbar^2}{2m}\sum_i \nabla_i^2 + \frac{1}{2}\sum_{i\neq j}\frac{e^2}{4\pi\epsilon_0|r_i - r_j|} - \sum_{i,I}\frac{z_I e^2}{4\pi\epsilon_0|r_i - R_I|}\end{aligned} \tag{2.1.2}$$

In equation (2.1.2), the indices *i, j* are for used for electrons and *I*, *J* for atomic nuclei, M_I to denote nuclear mass, m for the mass of an electron, r_i and R_I to denote the coordinate of electrons and nucleus, and Z_I denote the atomic number. Since solid material is a strongly coupled system of electrons and nuclei, both electronic and nuclear coordinates have been used to describe the non-relativistic Hamiltonian of the system.

The first term of the Hamiltonian is the kinetic energy of nuclei, 2nd term is for nuclei-nuclei interactions, 3rd term for the kinetic energy of electrons, 4th term for the electron-electron interactions, and the last term to describe the electron-nuclei interactions.

To deal with such a Hamiltonian of the Schrodinger equation, if the system we are interested in is an atom or a small molecule, the number of particles is still rather small,

but if we are dealing with larger systems, describing the wave function of the system explicitly becomes infeasible, which makes it very difficult for the study of the electronic properties of systems. However, since we started with the Hamiltonian of such length, we may make it simpler by employing Born-Oppenheimer approximation. To be noted that solving such an equation (2.1.1), it takes a lot of approximations.

2.1.3 Born-Oppenheimer (BO) approximation

To begin with Born-Oppenheimer (BO) approximation, one must consider the fact that the nuclei are far massive than electrons, and the velocities of nuclei are relatively low compared to that of electrons. Thus, the time scale for the relaxation of electrons is shorter than that of nuclei. In that scenario, the assumption is that the electron cloud is found to be completely relaxed at any given time even though the atoms are still vibrating. Therefore, the BO approximation allows us to separate the electron and atom motion and dealing the terms in equation (2.1.2) related to the electron states separately from the atomic nuclear states. Hence, the many-particle system can be reduced to the following:

$$\mathcal{H} = -\frac{1}{2}\sum_{i} \nabla_i^2 + +\frac{1}{2}\sum_{i \neq j} \frac{e^2}{|r_i - r_j|} - \sum_{i,I} \frac{z_I e^2}{|r_i - R_I|} \qquad (2.1.3)$$

For simplicity, the units are converted to atomic units, where $\hbar = 1, 4\pi\epsilon_0 = 1$.

Thus, equation (2.1.3) represents a strongly interacting gas or liquid of electrons moving in an external potential, and the Hamiltonian acting on the electrons can now be written as

$$\mathcal{H} = T + W + V_{ext} \tag{2.1.4}$$

The first term, T is the kinetic energy operator for the electrons, the 2nd term is the electron-electron Coulomb interaction potential, and the 3rd term is the electron-nuclei interaction potential, also known as the external potential V_{ext} . The external potential refers to the fact that electrons move in the field set by the nuclei.

Now, the Schrodinger equation becomes

$$\mathcal{H}\,\Psi = [\,T\ +\ W\ +\ V_{ext}\,]\,\Psi = \mathrm{E}\,\Psi \tag{2.1.5}$$

The corresponding total energy now can be found as the expectation value of the Hamiltonian, which is

$$\mathrm{E} = \langle \Psi | \mathcal{H} \,|\, \Psi \rangle \tag{2.1.6}$$

Thus,

$$\mathrm{E} = T + W + \int d^3r\, V_{ext}(r) n(r) \tag{2.1.7}$$

Here, T and W are the expectation value of the kinetic energy operator and electron-electron interaction operator respectively. $n(r)$ is the electron density. At this stage of the formulation pictured in equation (2.1.7), we need a full descriptive form of the kinetic energy and the electron-electron interaction, which should include both the classical and quantum mechanical nature of electrons and their interactions. Hence, the reason why the quantity $n(r)$ which is introduced here as the electron density play as the key role to the formulation of DFT needs to be understood first. The transition from

wave function formalism to the electron density treatment requires to be discussed briefly in the following section.

Therefore, before we proceed further, it is important to look back at the development and the early foundations of the density functional theory. Hence in the next section, a set of models prior to DFT have been discussed.

2.1.4 Background of DFT

The background and development of DFT consists of a long era for solving the many body Schrödinger equation of a quantum mechanical many body system effectively. The early work on density functional theory can date back to as early as 1927, when Thomas-Fermi model was introduced by replacing the wave function with electron density of a system. Thus, going into details of the density functional theory, it is worth to summarize its forerunners briefly so that an understanding to the development of DFT can be depicted.

Here, the following models are briefly described:

a. Free electron model (FEM)

b. Hartree and Hartree-Fock approach

c. Thomas-Fermi

❖ Free-Electron Model

This model attempted to solve the last equation assuming electrons in metals constitute an ideal gas of fermions. Thus, the electrons are assumed to interact with each other in the same way as do neutral gas molecules in an ideal gas. As an added

feature, it is also assumed that the electrons obey fermion statistics. The ion cores and nuclei are taken as stationary. This model succeeded in describing metals like silver or aluminum surprisingly well even though it failed to describe semiconductors well.

❖ The Hartree and Hartree-Fock Approaches

In Hartree approach, electrons are assumed to be non-interacting. Therefore, each electron i should obey a Schrodinger like equation as follows

$$\mathcal{H}_{\text{eff}}\,\Psi_{\text{i}}(\text{r}) = \left(-\frac{1}{2}\nabla^2 + V_{eff}\right)\Psi_{\text{i}}(\text{r}) = \epsilon_i \Psi_{\text{i}}(\text{r}) \qquad (2.1.8)$$

Where electrons move in an effective potential named as V_{eff}, and the effective Hamiltonian as $\mathcal{H}_{eff}$ .This model obeys Pauli principle and the ground state is determined by the lowest lying eigenstates. However, this model has a great limitation to decide the form of the effective potential V_{eff}.

As a development to this model later came Hartree-Fock approach, where a total wave function for the system is used instead of separate single-particle wave functions $\psi_i(r)$, and by construction, the effect of exchange is built into the model such that when two electron quantum numbers are switched, the wave function changes the sign.

❖ Thomas-Fermi Model

Replacing the wave function with charge density was first introduced by this model in 1927, which was later improved by Dirac. Dirac included a term to describe the exchange energy. The total energy in this approach is

$$E_{TF} = C_1 \int d^3r\, n(r)^{\frac{5}{3}} + \int d^3r\, V_{ext}(r)n(r) + C_2 \int d^3r\, n(r)^{\frac{4}{3}} + \frac{1}{2}\int d^3r d^3r'\, \frac{n(r)n(r')}{|r-r'|} \quad (2.1.9)$$

Where

$C_1 = (3/10)(3\pi^2)^{2/3}$

and

$C_1 = -(3/4)(3/\pi)^{1/3}$

The 1st term of equation (9) describes the kinetic energy, 2nd term for the electron-nuclei interaction energy, 3rd term for the exchange and the last term is for electron-electron Coulomb interaction energy, also known as the Hartree energy. To calculate the kinetic and exchange-correlation energy in this approach, it is assumed that electrons in the system form a homogenous gas. The idea of homogenous electron gas is of fundamental importance for DFT. Thus, the density now can very easily be calculated by dividing the total charge with total volume.

To describe the density functional theory, it will require two steps. First, the DFT theorems provided by Hohenberg and Kohn and then the Khon-Sham formalism which maps many electron representations to single particle treatment. In the following, these are discussed.

2.1.5 Hohenberg-Kohn theorem

- Statement 1

  The ground state expectation value of the Hamiltonian is a unique functional of the exact ground state electron charge density.

  Therefore, the ground state total energy E of a system is a unique functional of electron charge density n(r).

  $E \rightarrow E[n]$

- Statement 2

  The exact ground state density n(r) minimizes the energy functional E[n].

  This statement provides a scheme to find the ground state charge density. For example, if we start with a set of trial charge density and calculate for the total energy, the density which corresponds to the lowest energy is the exact ground state electron density.

❖ Statement 3

If the first two terms of equation (2.1.7) are combined, then that can be considered as a universal functional in the sense that it does not depend on the external potential.

Let us rewrite equation (7) as the following

$$\mathrm{E} = T + W + \int d^3r\, V_{ext}(r)n(r) = F[n] + \int d^3r\, V_{ext}(r)n(r) \qquad (2.1.10)$$

Here F[n] is the universal functional and its form does not depend on $V_{ext}(r)$.

$$F[n] = T[n] + W[n] \qquad (2.1.11)$$

At this stage of the work, we need to know the form of $T[n]$ and $W[n]$. But it's not very simple to proceed on. We need to consider both the classical Coulomb interaction and the quantum mechanical nature of electrons in the system. Therefore, the idea of non-interacting homogenous ideal gas hypothesis can be taken into consideration, where the electrons are non-interacting and form a homogenous ideal gas. Then equation (2.1.11) can be written as

$$F[n] = T_S[n] + \frac{1}{2}\int d^3r\, d^3r' \frac{n(r)n(r')}{|r - r'|} + E_{xc}[n] \qquad (2.1.12)$$

Where the first term is the kinetic energy of the hypothetical electron gas, the 2nd term is the classical Coulomb interaction energy between electrons and the last term is the exchange and correlation energy which contains all many-particle effects result from the many-particle contribution to kinetic energy and the Pauli Exclusion Principle. To be noted that, in the term $T_S[n]$, the electron density is same as the actual ground

state density of real system. Now it's possible to calculate the ground state density and the total energy of the system from equation (2.1.10). However, we need to know the forms of $T_S[n]$ and $E_{xc}[n]$ for which we need to proceed to Kohn-Sham formalism in the following section.

2.1.6 Kohn-Sham formalism

This formalism provides a scheme to map many particle problems to a system of non-interacting single particles assuming that the ground state charge densities are same for both real and hypothetical one. If we include the terms of equation (2.1.12) into equation (2.1.10), we get

$$E[n] = T_S[n] + \frac{1}{2}\int d^3r\, d^3r' \frac{n(r)n(r')}{|r-r'|} + E_{xc}[n] + \int d^3r\, V_{ext}(r)n(r) \tag{2.1.13}$$

Applying the variational principle to the energy functional of equation (2.1.13), we get

$$\delta E[n] = 0 \tag{2.1.14}$$

$$\mu = \frac{\delta E[n]}{\delta n(r)} = V_{ext} + \int d^3r' \frac{n(r')}{|r-r'|} + \frac{\delta T_S[n]}{\delta n(r)} + \frac{\delta E_{xc}}{\delta n(r)} \tag{2.1.15}$$

Where μ is the Lagrange multiplier, also known as the chemical potential.

Now we apply the variational principle to the energy functional of the hypothetical system where it is considered that electrons are moving in the field of an effective potential. The energy functional in such case is

$$E[n] = T_S[n] + \int d^3r\, V_{eff}(r)n(r) \tag{2.1.16}$$

After applying the variation to E[n], we get

$$\mu = \frac{\delta E[n]}{\delta n(r)} = \frac{\delta T_S[n]}{\delta n(r)} + V_{eff} \tag{2.1.17}$$

Now from equation (2.1.15) and (2.1.16), it is evident that

$$V_{eff} = V_{ext} + \int \mathrm{d}^3r' \frac{n(r')}{|r - r'|} + \frac{\delta E_{xc}[n]}{\delta n(r)} \tag{2.1.18}$$

Where the last term of the above equation is called the exchange-correlation potential

$$V_{xc} = \frac{\delta E_{xc}[n]}{\delta n(r)} \tag{2.1.19}$$

Now, it can be stated that the effective potential transforms the many-particle problem to a single-particle formulation and the corresponding effective Hamiltonian for such case is

$$\mathcal{H}_{eff} = -\frac{1}{2}\nabla^2 + V_{eff} \tag{2.1.20}$$

And the Schrodinger equation is

$$\mathcal{H}_{eff}\,\psi_i(r) = \left(-\tfrac{1}{2}\nabla^2 + V_{eff}\right)\Psi_i(r) = \epsilon_i\psi_i(r) \tag{2.1.21}$$

The solutions to the above equation are the Kohn-Sham eigenvalues, $\{\epsilon_i\}$ and Eigen functions, $\{\psi_i(r)\}$ and the ground state density in this case is given by

$$n(r) = \sum_{i=1}^{N} |\psi_i(r)|^2 \quad (2.1.22)$$

Here the sum is for N lowest eigenstates of the effective Hamiltonian.

After solving equation (2.1.21), the form of the kinetic energy term $T_S[n]$ can be found as

$$T_S[n] = \sum_{i=1}^{N} < \psi_i \left| -\frac{1}{2}\nabla^2 \right| \psi_i > = \sum_{i=1}^{N} \epsilon_i - \int d^3r V_{eff}(r) n(r) \quad (2.1.23)$$

Then the total energy of the system is

$$E[n] = \sum_{i=1}^{N} \epsilon_i - \frac{1}{2}\int d^3r\, d^3r' \frac{n(r)n(r')}{|r-r'|} - \int d^3r\ V_{xc}[n]n(r) + E_{xc}[n] \quad (2.1.24)$$

At this point of the formulation, there remains no difficulty with the form of $T_S[n]$ but forms of $E_{xc}[n]$. The exact functional for $E_{xc}[n]$ is not available yet, but there have been developed some approximations and used to calculate for the total energy of many-particle systems within DFT framework.

A schematic of the flow chart of the DFT self-consistent loop while solving Kohn-Sham equation for a many body system is presented in Figure 2. 1.

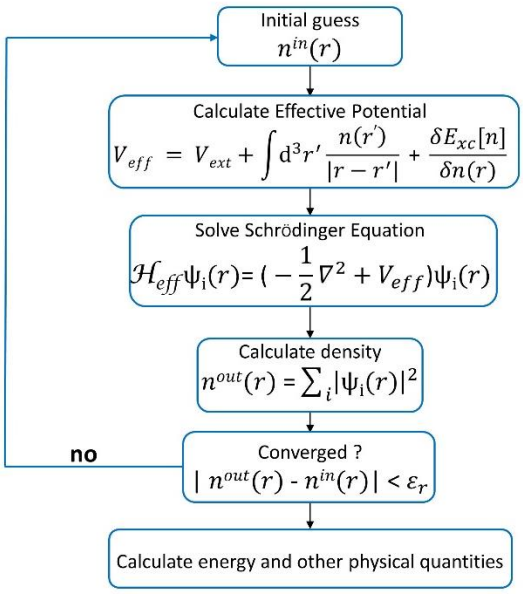

Figure 2. 1 A generic flow chart of DFT self-consistent loop for Kohn-Sham calculation.

2.1.7 Approximations to $E_{xc}[n]$

There are three popular approximations to $E_{xc}[n]$ which are presented in brief in the following.

(a) Local Density Approximation (LDA)

- Derived from homogenous electron gas
- Approximates the energy of the true density by the energy of a local constant density

Then exchange-correlation energy per particle of a homogenous electron gas with density n(r) is given by

$$E_{xc}^{LDA}[n] = \int d^3r\, n(r)\epsilon_{xc}(n) \tag{2.1.25}$$

Where the corresponding exchange-correlation potential can be expressed as

$$V_{xc}^{LDA} = \frac{\delta E_{xc}^{LDA}[n]}{\delta n} \tag{2.1.26}$$

(b) Generalized Gradient Approximation (GGA)

- Where the density undergoes rapid changes, an improvement over LDA is necessary
- Gradient of electron density is considered

The functional looks like in this case is

$$E_{xc}^{GGA}[n] = \int d^3r\, n(r)\, f\big(n(r),\, \nabla n(r)\big) \tag{2.1.27}$$

GGA is a better approximation than LDA and provide more accurate ground state properties of condensed matter.

(c) Hybrid Functionals

This functional incorporates a portion of exact exchange from Hartree–Fock theory with exchange and correlation from DFT, whereas several ways are available for this mixing. HSE06 is such a hybrid functional known as Heyd-Scuseria-Ernzerhof [73–75] functional, and has the following form

$$E_{XC}^{HSE} = \alpha E_X^{SR}(\mu) + (1-\alpha)E_X^{PBE,SR}(\mu) + E_X^{PBE,LR}(\mu) + (1-\alpha)E_C^{PBE} \quad 2.1.28$$

Where E_X^{SR} is the short-range part of the exact exchange and mixed with the short-range part of the GGA exchange $E_X^{PBE,SR}$. $E_X^{PBE,LR}$ is the long-range counterpart of the decaying long-range part of the exact change. In the above equation (2.1.28), α is known as the mixing parameter, and μ controls the short-rangeness of the interaction. Standard values for α and μ are 0.25 and 0.2, respectively.

2.1.8 DF+U

LDA or GGA functional employed DFT calculations often fail to describe strongly correlated systems with localized d or f electrons, which result inaccurate electronic and related properties by a factor of two [76,77]. This can be attributed to the lack of proper treatment of the self-interaction corrections of electrons. On the other hand, hybrid functional employed DFT can predict the electronic properties quite accurately in most of the cases although it's computationally highly expensive. In that case, a computationally cost-effective alternative than hybrid functional employed DFT calculation is to introduce an on-site Coulomb repulsion with a Hubbard parameter. This method is known as LDA/GGA + U method. The approaches developed to include this on-site interaction are known by Liechtenstein's [78] and Dudarev's approach [79]. In this work, Dudarev's approach is used.

Chapter 3

Stability enhancement of Cu_2S against Cu vacancy formation by Ag alloying

3.1 Introduction

Cu_2S has great importance in the field of renewable energy. In thin film solar cells, Cu_2S has proved its potential as a solar absorber material which brought much attention to the scientific community in past years [80–83]. This material is earth abundant and non-toxic. Cu_xS ($1 \leq x \leq 2$) exits in various mineral forms such as chalcocite [5, 6], djurleite [39], dijenite [41], anilite [42] etc. The stoichiometric Cu_2S exits in three different forms at three different temperature ranges. Monoclinic or low chalcocite phase (Figure 3. 1) is formed below 104^0C, hexagonal or high chalcocite phase in between 104^0C and 436^0C and cubic phase at or above 436^0C [38,39]. Among the stoichiometric structures, low chalcocite is the most stable one at room temperature [35,36].

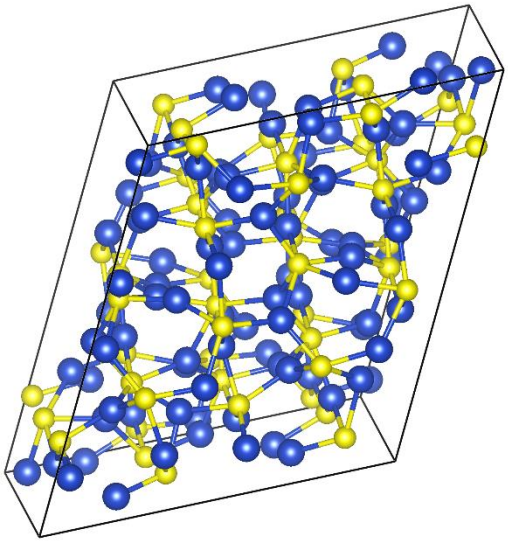

Figure 3. 1 Low chalcocite (monoclinic phase, Cu_2S); Cu in blue and S in yellow.

Even though low chalcocite is the most stable one, it is prone to form Cu vacancies [35,36,47,84–86]. In addition, Cu positions in the crystal unit may not be well defined. At or above 105^0C, this phase transforms into hexagonal or high chalcocite phase. This high chalcocite phase is a solid-liquid hybrid phase [43]. In this phase, Cu sub-lattice is found to remain in liquid phase while S sub-lattice remains in solid phase. This is however a complex crystal structure. In addition, other Cu_xS phases are also complex and show higher tendency to Cu vacancy formations. This vacancy formation trend leads to instability of copper sulfides. In another theoretical study based on DFT theory by Su-Huai et al., among known Cu_xS phases, anilite ($Cu_{1.75}S$) was shown to be the most stable structure at Cu-rich limit [35]. However, that structure is heavily doped with holes due to Cu vacancies. In this work, we look for a suitable structure of Cu_xS near

its stoichiometric composition such as x = 2 which would have less hole concentrations than that in anilite.

In a crystal structure database search and DFT study, a new phase of Cu_xS near stoichiometric composition (x = 2) has been predicted recently which is an acanthite like crystal structure at x = 1.98. This structure was found by replacing Ag atoms of acanthite Ag_2S with Cu atoms. It has been shown that this relatively new predicted acanthite Cu_2S is more favorable to form than low chalcocite structure at 0 K but Cu vacancy formation trend has not decreased, rather higher Cu vacancy formation tendency at x = 1.98 compared to low chalcocite phase has been found [37].

Hence, Cu vacancy formations in the crystal are major challenges toward the use of this material in the field of photovoltaic. Therefore, controlling Cu vacancy related effects are very important in this regard. In this study, we are focusing on two major aspects: (i) reducing Cu vacancy formation and (ii) controlling the diffusion of Cu atoms inside the acanthite Cu_2S crystal. For this purpose, we have alloyed Ag in acanthite Cu_2S so that the stability against Cu vacancy formation in the crystal increases. Hence, the vacancy formation probability is reduced and then the Cu atom's diffusion energy barrier inside the crystal is increased without altering the electronic properties of this material significantly. We have found that Ag alloying with acanthite Cu_2S can help to reduce the Cu vacancy formation tendency in the crystal while the formation of Ag alloyed structure is also thermodynamically favorable. In addition, the energy band gap of Ag alloyed structure is higher than that of pristine structure, which indicates a higher photovoltage is possible due to Ag alloy in acanthite Cu_2S.

3.2 Computational Methodology

The theoretical framework of this study is within the density functional theory (DFT) [18, 19]. The density functional theory is implemented as in Vienna ab-initio simulation package (VASP) [89,90]. We have used projector augmented wave (PAW) method [91,92] in generalized gradient approximation (GGA) also known as Perdew-Burke-Ernserhof (PBE) exchange correlation functional [93]. The energy cut-off for plane wave basis set was 400 eV. Total energies of all the structures have been calculated using VASP code. Before total energy calculations, we let all the structures to relax fully. Each ion has been relaxed until the force is equal or less than 0.01 eV/Å. The allowed error in total energy for global break condition in electronic self-consistent loop is 1E-6 eV and the achieved convergence for total energies based on k-grid is within 1E-5 eV. For a Cu_2S unit cell (12 atoms), 21x9x9 gamma centered k-point sampling has been used for structural optimization and DOS plots while 7x3x3 gamma centered k-point sampling has been used for a 2x2x2 supercell of Cu_2S (96 atoms). Since DFT underestimates band gap and it is well known for the case of transition metals, we have used GGA-DFT+U method for the calculations of band structures and density of states (DOS) plots. Here U is a Hubbard parameter and has been applied on both Cu-d and Ag-d orbitals to enhance on-site Coulomb interaction. In this study, U_{eff} (U - J) = 7 has been used where U = 8 and J = 1. A justification of the choice of U value will be discussed later. For all other calculations such as geometric optimization and total energies, GGA-DFT has been used only.

Since we have studied the stability issue of acanthite Cu_2S systematically, we have calculated formation energies of Ag alloyed acanthite Cu_2S and Cu vacant Cu_2S structures along with band structures and DOS plots. The formation energies of Ag alloyed structures have been calculated using the following formula:

$$E_f = E_{tot}(\text{compound}) - E_{tot}(\text{host}) + n(\mu_{Cu} + \Delta\mu_{Cu}) - n(\mu_{Ag} + \Delta\mu_{Ag}) \quad (3.1)$$

which requires the following to be satisfied

$$\Delta H_{Cu_2S} = 2\Delta\mu_{Cu} + \Delta\mu_S \text{ and } \Delta H(Cu_{2-x}Ag_xS) = (2-x)\Delta\mu_{Cu} + \Delta\mu_S + x\,\Delta\mu_{Ag} \quad (3.2)$$

where $E_{tot}(\text{compound})$ is the total energy of Ag alloyed Cu_2S and $E_{tot}(\text{host})$ is the total energy of pristine Cu_2S cell without Ag. M_{Cu} and μ_{Ag} are the chemical potentials of copper and silver respectively.

The enthalpies of formation of the strucutures have been calculated using by

$$\Delta H_{Cu_{2-x}SAg_x} = E(Cu_{2-x}SAg_x) - (2-x)E(Cu) - E(S) - xE(Ag) \quad (3.3)$$

Here $\Delta H_{Cu_{2-x}SAg_x}$ is the enthalpy of formation of $Cu_{2-x}SAg_x$. $E(Cu_{2-x}SAg_x)$ is the total energy per formula unit for Ag alloyed Cu_2S compounds. $E(Cu)$, $E(S)$ and $E(Ag)$ are total energies per Cu atom, S atom and Ag atom respectively in their stable bulk phases.

The enthalpy of formation of acanthite Cu_2S per formula unit has been calculated using the total energy of a 2x2x2 acanthite Cu_2S supercell and the bulk energies of Cu and S. The enthalpy of Cu_2S per formula unit is $\Delta H_{Cu_2S} = -0.4362\ \text{eV}$. Using this value and Equation (3.2) we get $\Delta\mu_{Cu} = -0.22\ \text{eV}$ and $\Delta\mu_S = 0\ \text{eV}$ at Cu-poor condition while

$\Delta\mu_{Cu} = 0\ \text{eV}\ \text{and}\ \Delta\mu_{S} = -0.4362\ \text{eV}$ at Cu rich condition. The Cu chemical potential has been taken to be equal to the energy of its bulk phase.

3.3 Acanthite Cu_2S

The acanthite Cu_2S structure as in Figure 2, has 8 Cu atoms and 4 S atoms in its unit cell. This structure was derived from acanthite Ag_2S by replacing all the Ag atoms in its unit cell with Cu atoms and was fully relaxed by DFT until the force on each ion was equal or less than 0.01 eV/Å [37]. Cu atoms are in layers along (101) plane and S atoms are arranged around Cu atoms to form trigonal planar along (010) as in Figure 3. 2. For this structure, traditional DFT only calculation shows no band gap. However, a band opening in its band structure is observed if an on-site Coulomb interaction is added on Cu-d with GGA-DFT+U method [79,94]. At U_{eff} = 7, the calculated band gap is 0.86 eV while the experimental band gaps of Cu_xS ($1 \leq x \leq 2$) fall in the range of 1.1-1.2 eV [9, 16]. The band structure is presented in Figure 3. 3. The no band gap with traditional DFT is due to the well-known fact that GGA-DFT underestimates the band gap for materials with partially filled 3d bands.

In Table 3. 1, we see that band gap increases with higher U values and the type of the band gap changes from indirect to direct at U = 11. Even though for U values higher than 8, band gap increases considerably, and the minimum of the conduction band tends to move along Z-Γ while the maximum of the valance band remains at Γ point. Finally, the gap becomes completely direct at U = 11. Furthermore, the top of the valance band shifts down toward the more negative of the valance band with the application of higher U

values on Cu-d. This is since highly localized d^{10} orbitals move toward the more negative of the valance band with higher Coulomb repulsion. In addition, the well-known experimental band gap of Cu_2S phases is indirect [96]. Hence, U = 8 and J = 1 (U_{eff} = 7) were chosen for the calculations of band structures and DOS plots. However, no U was applied for other calculations such as ionic relaxations and total energies of various Cu_XS systems.

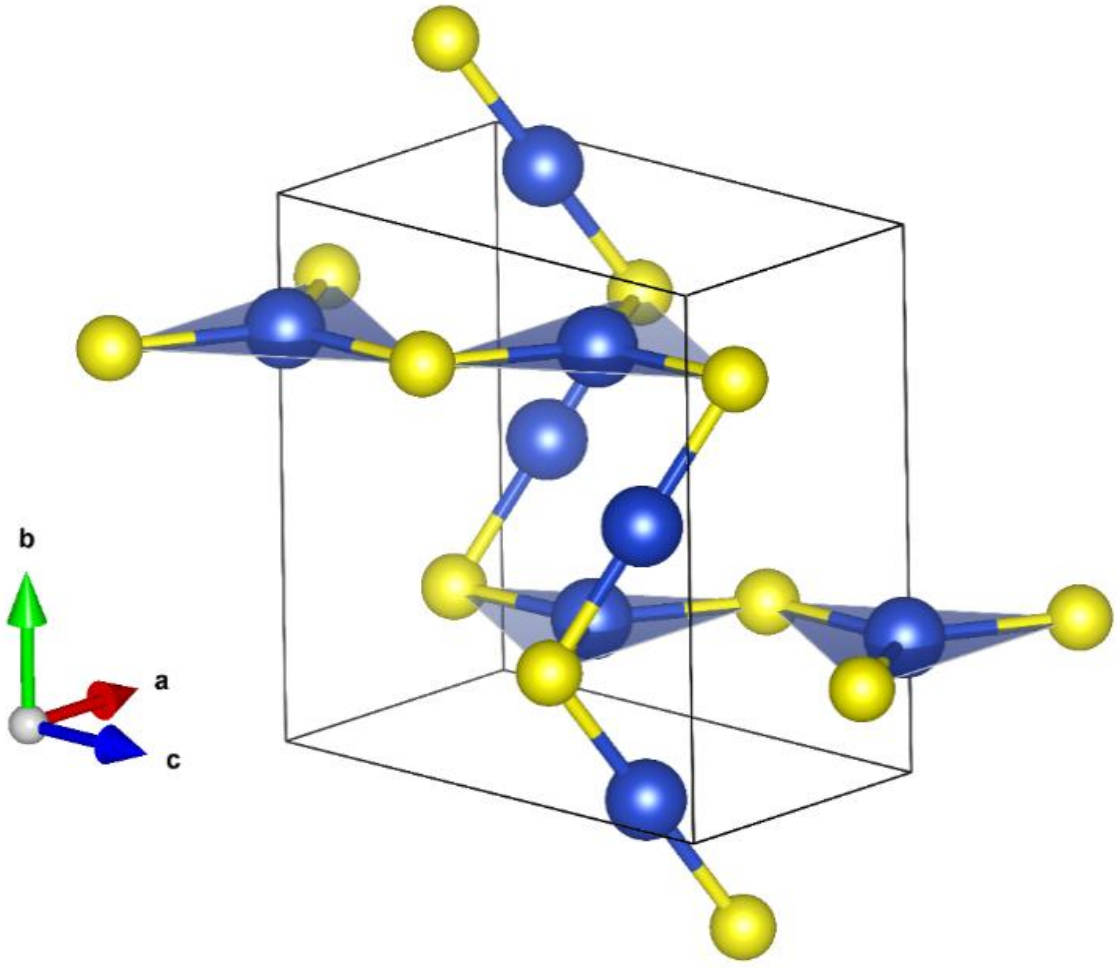

Figure 3. 2 Acanthite Cu_2S unit cell; Cu in blue and S in yellow.

Table 3. 1 Band gaps of acanthite Cu_2S and their types with different U values

U	Band Gap(eV)	Band Type
0.00	No Gap	
3.00	0.10	Indirect
5.00	0.42	Indirect
7.00	0.70	Indirect
8.00	0.86	Indirect
9.00	0.99	Indirect
11.00	1.19	Direct

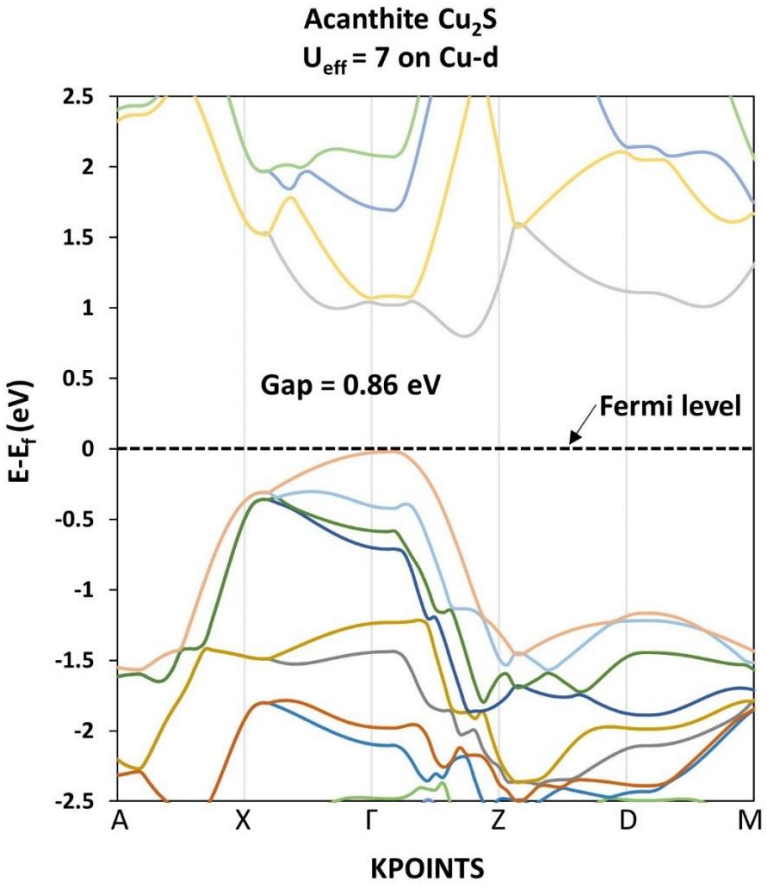

Figure 3. 3 Band structure of acanthite Cu_2S calculated by GGA-DFT+U method. Here, U_{eff} = 7 is applied on Cu-d only, where U = 8 and J = 1. The zero-energy level is defined by subtracting the Fermi energy (E_f).

The band opening can also be viewed from its corresponding DOS plots. The Cu-d orbital which is highly localized near the Fermi level shifts toward the more negative energy of the valance band as in Figure 3. 4, due to enhanced Coulomb repulsive potential. In Figure 3. 4, it can also be seen that the total DOS intercepts the Fermi level and Cu-d orbital is active near the Fermi level when no U is applied. At U_{eff} = 7, Cu-d peak at -0.91 eV moves at -1.79 eV, peak at -2.13 eV moves at -3.57 eV, and shows a band opening as in the band structure.

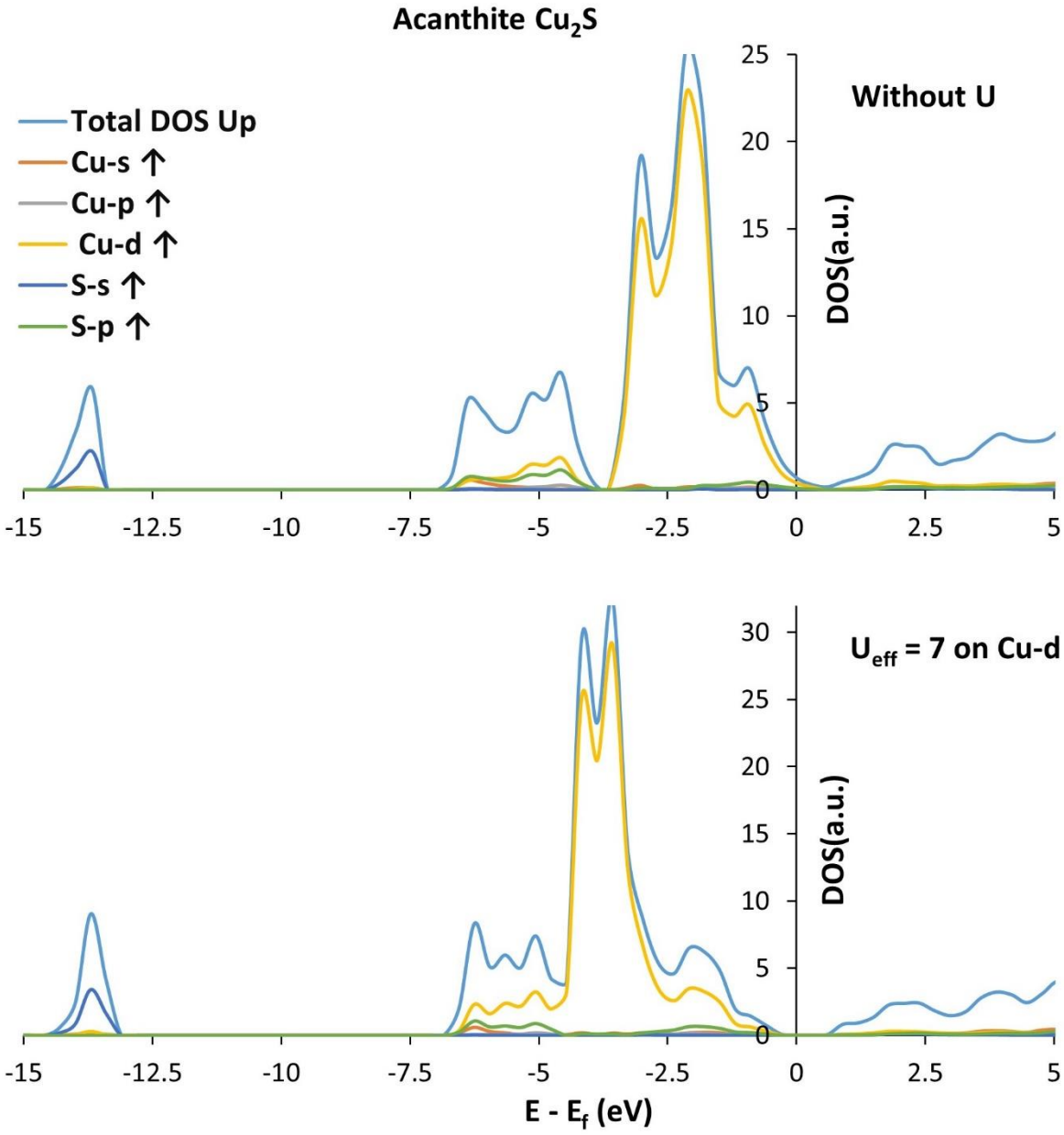

Figure 3. 4 Density of states (DOS) plots for acanthite Cu_2S for U_{eff} = 0 and U_{eff} = 7. The zero-energy level is defined by subtracting the Fermi energy (E_f).

3.4 Cu vacancy

The well-known tendency of forming Cu vacancies in Cu_2S phases leads the material to behave as a p-type material, and higher number of vacancies eventually turn this into a degenerate semiconductor. This vacancy formation tendency can be realized from the defect (Cu vacancy) formation energy. In the pristine structure of acanthite phase, the defect formation energy per Cu vacancy in a supercell is 0.04 eV at Cu rich and -0.18 eV at Cu poor condition. The negative value of formation energy indicates that spontaneous formation of a Cu vacancy is possible at Cu poor condition, while such a vacancy can also easily be formed due to thermal excitation since the defect formation energy at Cu rich condition is very low. The equivalent temperature of 0.04 eV is 464.20 K. From the calculation of defect formation energies, we find that a second vacancy formation is also favorable at Cu poor condition even though the formation energy is 0.06 eV higher than that for a single vacancy. Overall it is seen from Figure 3. 5 that more than 1 Cu vacancy at Cu poor condition are favorable in this structure. In addition, it is to be noted that the formation of a Cu vacancy in an acanthite crystal does not deform the crystal structure much.

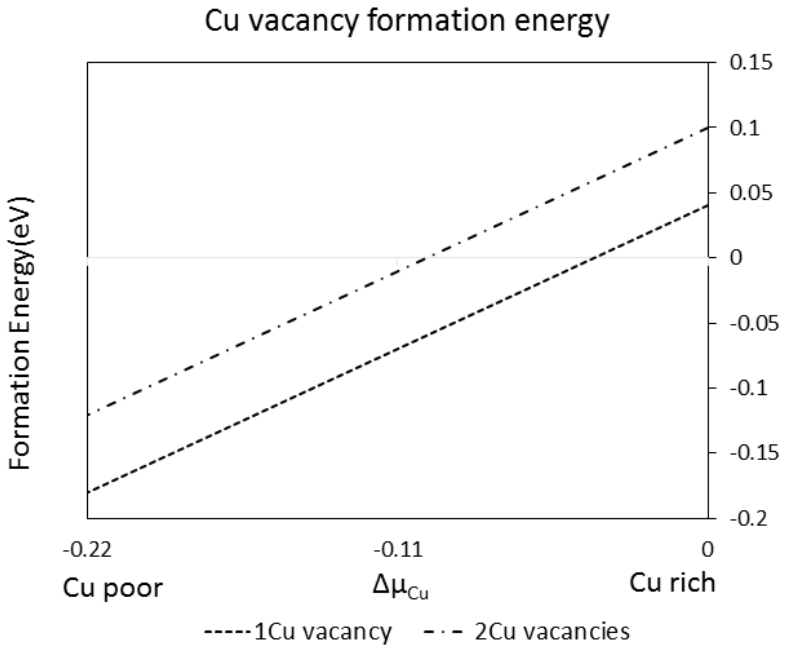

Figure 3. 5 Defect formation energies for 1 and 2 Cu vacancies per supercell in acanthite Cu_2S.

Here, we compare the lattice parameters of a fully relaxed 2x2x2 pristine supercell with a Cu vacant structure. In Table 3. 2, we see that the lattice parameters are almost same with a little change of 0.01 to 0.02 Å for c and b respectively while for α and γ its 0.01° and for β its 0.13°. This little or no change in the crystal structure might be another possible reason for Cu vacancies to be highly favorable in this phase as well.

Table 3. 2 Lattice parameters of 2x2x2 pristine Cu_2S and 1 Cu vacant supercells.

	a(Å)	b(Å)	c(Å)	α(°)	β(°)	γ(°)
Pristine structure, Cu_2S	8.01	14.34	13.72	90.00	89.00	90.00
1 Cu vacant Cu_2S structure	8.01	14.36	13.71	89.99	89.13	89.99

However, the band gap of this defect structure increases from 0.86 eV (for pristine) to 0.93 eV (for defect). From the band structure of this acanthite Cu_2S with defect, as in Figure 6, we see two bands from the top of valance band intercept the Fermi level. The intercepting bands are due to a hole state created from the vacancy and the possible hybridization between Cu-d and S-p near or at the Fermi level. Nevertheless, the band gap is still indirect. This effect can clearly be viewed from the corresponding DOS plot as in Figure 3. 7. The plot shows a possible Cu-d and S-p hybridization at the Fermi level. Due to the Cu vacancy in the crystal, a Cu-d orbital contributes to the conduction band. Hence a hybridization between Cu-s, Cu-d, S-s and S-p is possible which can be seen from the inset of Figure 3. 7.

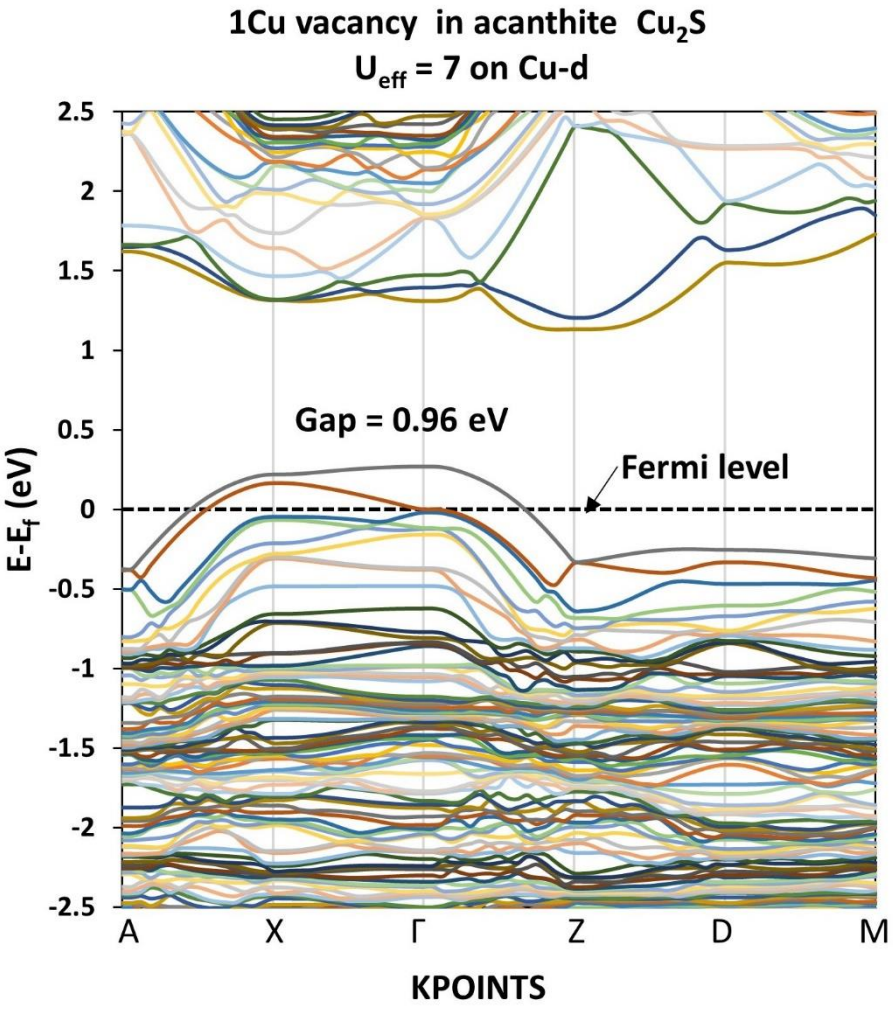

Figure 3. 6 Band structure of a Cu vacant acanthite Cu_2S for U_{eff} = 7 applied on Cu-d. The zero-energy level is defined by subtracting the Fermi energy (E_f).

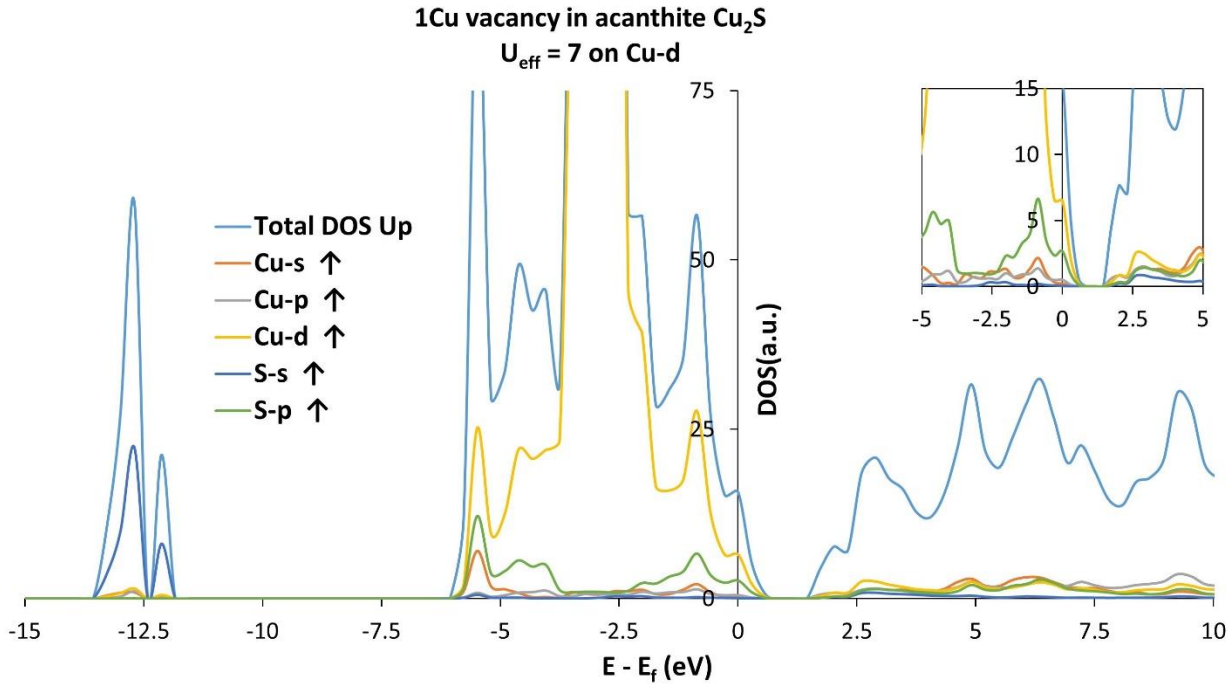

Figure 3. 7 Density of states (DOS) plot of a Cu vacant acanthite Cu_2S supercell. Inset is the magnified DOS for a selected portion. The zero-energy level is defined by subtracting the Fermi energy (E_f).

Even though the newly predicted acanthite Cu_2S is more favorable than low chalcocite at stoichiometric composition, its Cu vacancy formation tendency at x = 1.98 was reported higher than that in low chalcocite [37]. This vacancy formation tendency is a potential hindrance to the prospect of its usages as a solar absorber material. Hence, stabilizing this material against vacancy formation is essential.

To study in detail with this predicted acanthite phase of Cu_2S, we take a 2x2x2 supercell which contains a total of 96 atoms, 64 of them are Cu atoms and 32 of them are S atoms. The structure is shown in Figure 3. 8. In the supercell, Cu layers are seen to form along (101) plane and S atoms are arranged in between consecutive Cu layers.

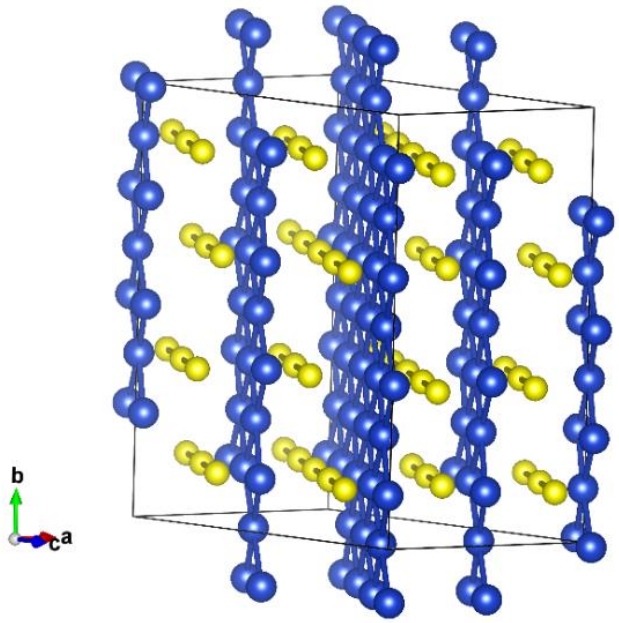

Figure 3. 8 Acanthite Cu_2S supercell; 64 Cu atoms in blue and 32 S atoms in yellow.

3.5 Silver alloy

Since the acanthite phase of Cu_2S is derived from Ag_2S, we alloy Ag in Cu layers in different concentrations. Different arrangements of Ag atoms in a Cu layer are made to have different alloy configurations, as in Figure 3. 9, and we look for the most favorable structures according to their energetics. After that we calculated the energies of Cu vacancy formation in those alloyed structures.

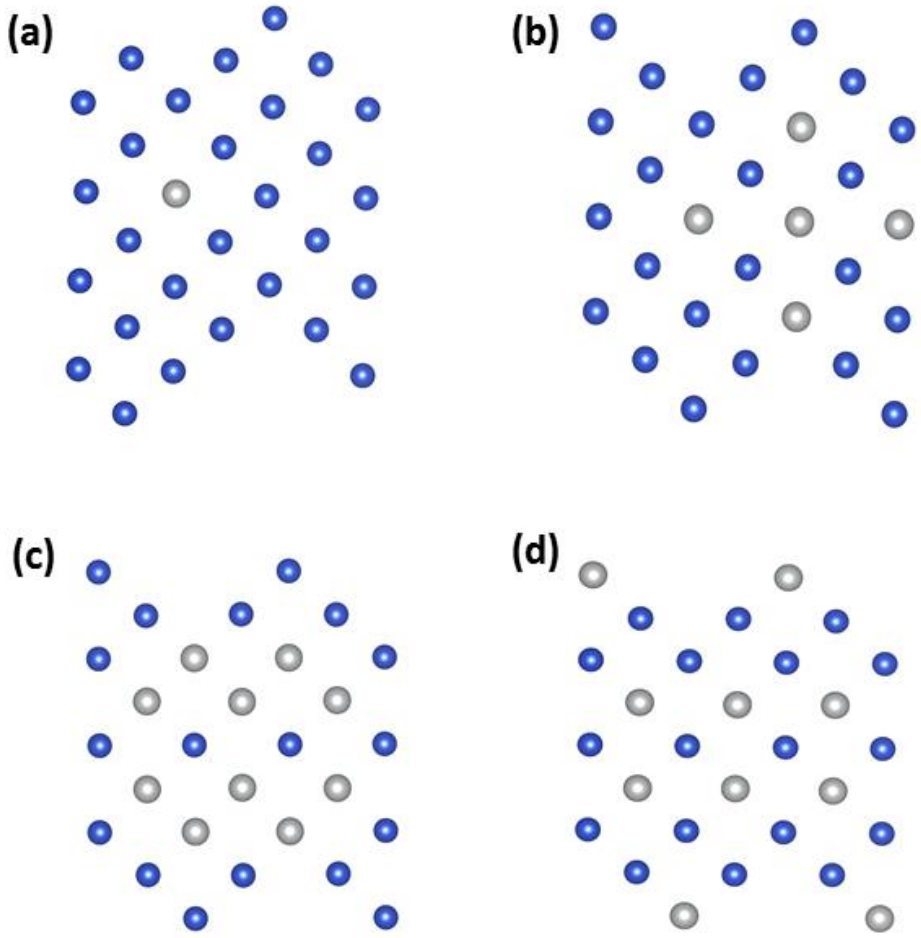

Figure 3. 9 (a) 1 Ag atom, (b) 5 Ag atoms doped in a Cu layer, (c) 10 Ag atoms (str 1) and (d) 10 Ag atoms (str 2) arranged in different configurations in a Cu plane within an acanthite Cu_2S supercell; Cu in blue and Ag in silver.

Since different configurations of Ag-Cu alloy are possible in a Cu layer, here we present two different arrangement of alloys for ten Ag atoms in the structure as in Figure 3. 9(c) and (d) as examples.

Table 3. 3 Formation energies for Ag alloyed structures are presented. For Ag doping, a 2x2x2 acanthite Cu_2S super cell is considered. There are 64 Cu atoms and 32 S atoms in a pristine Cu_2S super cell.

	Alloy formation energy per Ag atom (eV)		Enthalpy of formation per formula unit (eV)
	Cu rich	Cu poor	
Cu_2S			-0.44
1Ag-Cu_2S	0.30	0.08	-0.43
1Ag in 1Cu-vacant Cu_2S	0.04	-0.18	-0.43
1Cu in 1Cu-vacant Cu_2S	-0.04	0.18	-0.44
10Ag-Cu_2S(str1)	0.28	0.06	-0.35
10Ag-Cu_2S(str2)	0.28	0.06	-0.35

The energetics presented in Table 3. 3 shows that the formation energies per Ag atom are very low and their enthalpies of formation are all negative which indicate the Ag alloy formation in acanthite Cu_2S is thermodynamically favorable. The energetics also show that doping of an Ag atom in a structure containing a Cu vacancy is energetically as favorable as an acanthite Cu_2S crystal formation. The enthalpy of formation of a pristine acanthite Cu_2S crystal and an Ag doped crystal are -0.44 eV and -0.43 eV respectively. The enthalpies of an Ag doped in a pristine acanthite structure and in a Cu vacant structure are both -0.43 eV. On the other hand, the energies of formation per Ag atom of Ag doped structures are very low, which are 0.30 eV at Cu rich and 0.08 eV at

Cu poor for 1Ag-Cu_2S while these are 0.04 eV at Cu rich and -0.18 eV at Cu poor conditions for 1Ag in 1Cu-vacant Cu_2S structure. The formation energies for 1Cu in 1Cu-vacant Cu_2S which is analogous to 1Ag in 1Cu-vacant Cu_2S are -0.04 eV at Cu rich and 0.18 eV for Cu poor condition. This indicates that Cu_2S structure intends to retain its pristine structure at Cu rich condition and takes little energy for 1Cu atom to get into a Cu vacant site at Cu poor condition. On the other hand, 1Ag atom can easily be doped into a Cu vacant site at Cu poor condition and requires little energy at Cu rich condition. Hence, it is seen that 1Ag atom can be doped into a Cu vacant site at a controlled Cu environment, meaning that Ag alloy is thermodynamically possible to form. In addition, the energy cost per Ag atom for alloying higher number of Ag atoms goes lower, such as for ten Ag atoms in the structure it is 0.02 eV less than a single Ag atom in the structure at both Cu rich and poor conditions while their enthalpies of formation are both -0.35 eV.

3.6 Cu-vacancy in Ag alloyed Cu_2S

Table 3. 4 Energy of formation per Cu vacancy in acanthite Cu_2S with Ag alloying.

	Defect formation energy per Cu vacancy (eV)	
Cu vacancy in	Cu rich	Cu poor
Cu_2S (1 vacancy/supercell)	0.04	-0.18
Cu_2S (2 vacancies/supercell)	0.10	-0.12
1Ag-Cu_2S (1 vacancy/supercell)	-0.22	-0.44
1Cu-vacant_1Ag-Cu_2S (2 vacancies/supercell)	0.25	0.03
10Ag-Cu_2S(str1) (1 vacancy/supercell)	0.11	-0.11
10Ag-Cu_2S(str2) (1 vacancy/supercell)	0.08	-0.14

In the thermodynamically stable alloyed structures of $Ag_xCu_{2-x}S$, the Cu vacancy formation energies at both Cu rich and Cu poor conditions are calculated and presented in Table 3. 4. The formation energy for a single Cu vacancy in one Ag atom doped Cu_2S is less than that in a pristine Cu_2S, which indicates a defect formation is more favorable in the Ag doped crystal, which may occur due to the impurity related strain. However, a second vacancy in the same structure i.e. in 1Cu-vacant_1Ag-Cu_2S structure is relatively less favorable. The formation energy goes higher by 0.21 eV at both Cu-extreme

conditions. Hence more than one vacancy is not thermodynamically favorable in an already Cu vacant and one Ag atom doped Cu_2S crystal. In structures with higher number of Ag atoms such as 10 Ag atoms as in Figure 3. 9(c) and (d), a vacancy formation is less favorable than a vacancy in pristine acanthite Cu_2S. The vacancy formation energies in the Ag alloyed structure having alloy arrangement as in Figure 3. 9(c) are 0.11 eV at Cu rich and -0.11 eV at Cu poor which are higher than the formation energies per vacancy in pristine Cu_2S for both one and two vacancies per supercell. These are 70 meV and 10 meV higher respectively. In addition, the structure having alloy arrangement as in Figure 3. 9(d) has 40 meV higher energy than a single vacancy in pristine Cu_2S but 20 meV less energy than the case for two vacancies. Overall, the energetics suggest that Ag alloying in acanthite Cu_2S can help to reduce Cu vacancy formation tendencies. As the defect concentrations depend on the formation energies, this implies that at similar thermodynamic conditions, Cu vacancy density in Ag alloyed acanthite Cu_2S will be less than that in the pristine acanthite Cu_2S. A schematic of alloy and defect formation energies is presented in Figure 3. 10.

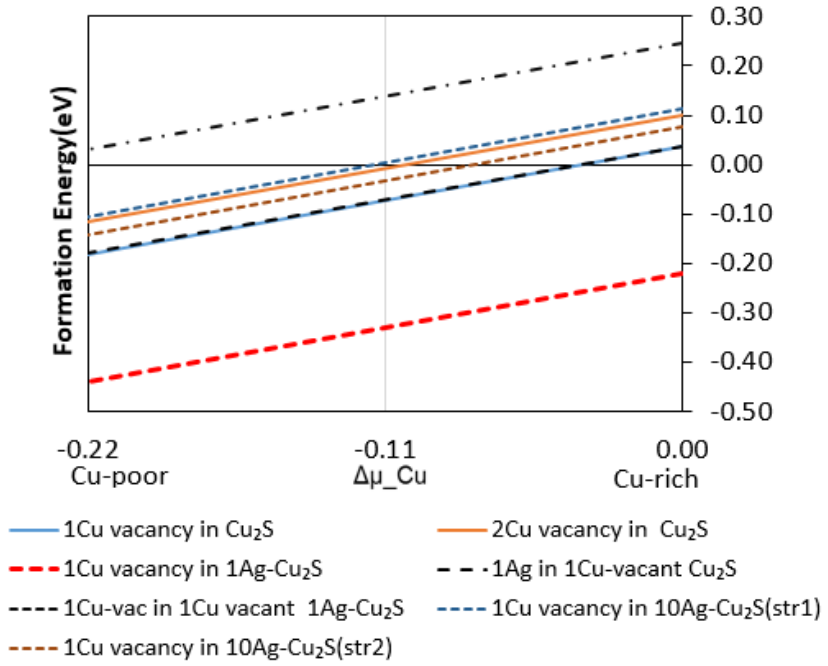

Figure 3. 10 Energy of formation of Cu vacancy in pristine and silver doped acanthite Cu_2S.

It is also important to check the energy band gap of Ag alloyed structures to make sure it is good enough to be used as a photovoltaic material. The band gap of 10 Ag atoms alloyed in Cu_2S supercell is 0.93 eV which is 0.07 eV higher than that of the pristine Cu_2S. However, if a Cu vacancy is considered in this alloyed structure, the direct gap is 0.90 eV which is still higher than the pristine one.

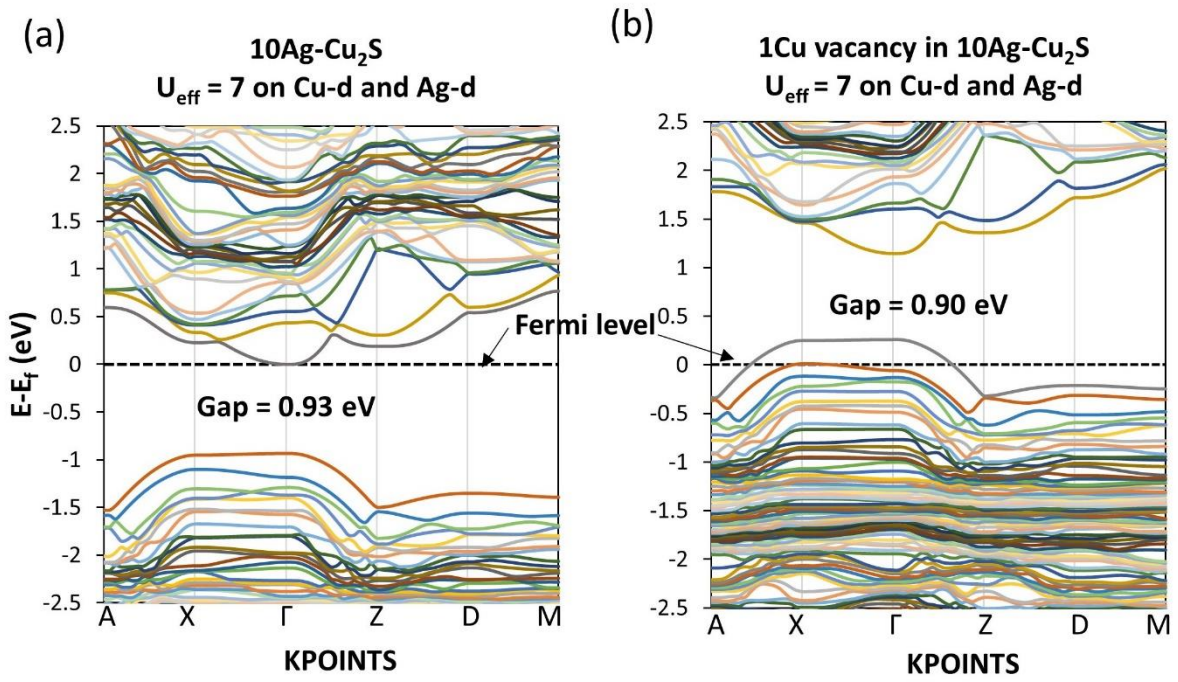

Figure 3. 11 Band structures of (a) 10 Ag atoms alloyed Cu_2S and (b) 1Cu vacancy in 10Ag-Cu_2S supercell. In both cases, U_{eff} = 7 has been applied on Cu-d and Ag-d simultaneously.

The gap as in Figure 3. 11(a) shifts below Fermi level since U has been applied on both Cu-d and Ag-d orbitals which become localized toward the more negative in the valance band. A Cu vacancy in this Ag alloyed structure leaves a hole state in the valance band since Ag atom enters with +1 oxidation state like a Cu atom. Hence, a band from the valance band is found to intercept the Fermi level as in Figure 3. 11(b). However, the number of bands intercepting the Fermi level is less than that in a Cu vacancy containing pristine Cu_2S structure as seen in Figure 6 where two bands intercepted the Fermi level.

3.7 Controlling Cu-diffusion

To analyze the Cu vacancy formation, we studied Cu diffusion inside the crystal. After the vacancy is formed, the vacancy forming atom should leave its original site and travel somewhere else. In this case, the diffusion study can help us to understand the nature of the vacancy formed by Cu atoms, which are moving to different interstitial sites. The diffusion study can also help to recognize paths of diffusion and energies required by atoms to diffuse through different paths. To model such a diffusion path followed by a dislocated Cu atom, we have calculated the diffusion energy barrier while a Cu atom diffuses through a Cu plane for both undoped and Ag atom doped supercells. The results are reported in this section. At first, we take a fully relaxed acanthite Cu_2S supercell and choose a Cu atom to be displaced to different interstitial sites. For some cases, the displaced Cu atom relaxes back to its original position while in other cases it stays to some favorable sites and does not come back to its original position at all. For such a dislocated Cu atom, as in Figure 3. 12, a tunnel in the crystal is chosen to model the diffusion. To do so, a cross marked Cu atom in an undoped crystal (as seen in Figure 3. 12(a)) has been displaced from its original site to different nearby interstitial sites. After full relaxations, we have found that the displaced Cu atom is relaxed back to the original site in most of the cases. In some cases, the displaced atom remains in suitable interstitial sites. For such a case, a stable structure is found when this displaced Cu atom has been placed in the center of a tetragon of four nearby Cu atoms along a tunnel inside the crystal. After full relaxation of that system, we have applied the nudge elastic band (NEB) method to find the minimum energy path (MEP) and calculated the diffusion energy

barrier of that diffused Cu atom. The saddle point along the MEP gives the diffusion energy barrier in this case [97] . The calculated diffusion energy barrier of the Cu atom in the undoped acanthite Cu_2S structure is found to be 0.72 eV. The plot is presented in Figure 3. 13. After the energy barrier is calculated for an undoped acanthite Cu_2S supercell, we intend to compare the result with the Ag doped case. Thus, the next step is to find what would happen to the energy barrier if the dislocated atom has an Ag atom doped in the neighborhood of its original position. For this to be done, an Ag atom is doped in a Cu site near the intended diffusing Cu atom, and the structure is relaxed completely. Then we have displaced the Cu atom to different interstitial sites again to check if a similar tunnel can be found along which the displaced Cu atom would not relax back. When we have got one like the undoped crystal, the elastic band method is applied to find the minimum energy path (MEP) and to calculate for the energy barrier. To be noted, all the initial and final structures were relaxed completely so that the energy calculation is accurate enough and the global break condition for the total energy in electronic self-consistent loop is kept within 1E-6 eV. The diffusing Cu atom in Ag doped crystal is identified with a cross mark as in Figure 3. 12(c) and the final defect structure with displaced stable Cu atom is presented in Figure 12(d). The diffusion energy barrier in this case is 0.77 eV, which is 50 meV higher than that in the undoped acanthite Cu_2S supercell. In the relaxed Ag doped structure, the displaced Cu atom forms a trigonal planar with three S atoms in the tunnel and the doped Ag atom forms a tetrahedra with four nearby S atoms as in Figure 3. 12(d).

The higher diffusion barrier in Ag doped crystal may be attributed to the distortion in the lattice that occurs in the diffusion environment. If we look carefully, it is seen that

the distortion in the diffusion environment is higher for the case of Ag doped structure. The Cu atom next to the diffused one displaces from the original site less in the pristine structure than in the doped Ag atom structure. The doped Ag atom displaces 0.12 Å with respect to the original position while the corresponding Cu atom in the pristine crystal displaces only 0.06 Å. For the Ag atom, it is twice as much as the Cu atom. For a S-Cu-S linear bond in the pristine structure, the S-Cu bond length is 2.18 Å which increases by 0.10 Å after the diffusion takes places. On the contrary the linear S-Ag-S bond breaks down in the Ag doped structure and a tetrahedra forms (as seen in Figure 3. 12(d)) with the diffusion and the average S-Ag bond for that tetrahedra becomes 2.75 Å, which is 0.35 Å higher than initial S-Ag bond length in the S-Ag-S linear arrangement. The higher distortion in the Ag doped structure may also be related to the higher ionic radius of Ag, which is 1.15 Å while that for the Cu is 0.73 Å. This clearly shows that the Ag atom needs to displace more than the corresponding Cu atom while Cu diffusion takes places along the path in the tunnel.

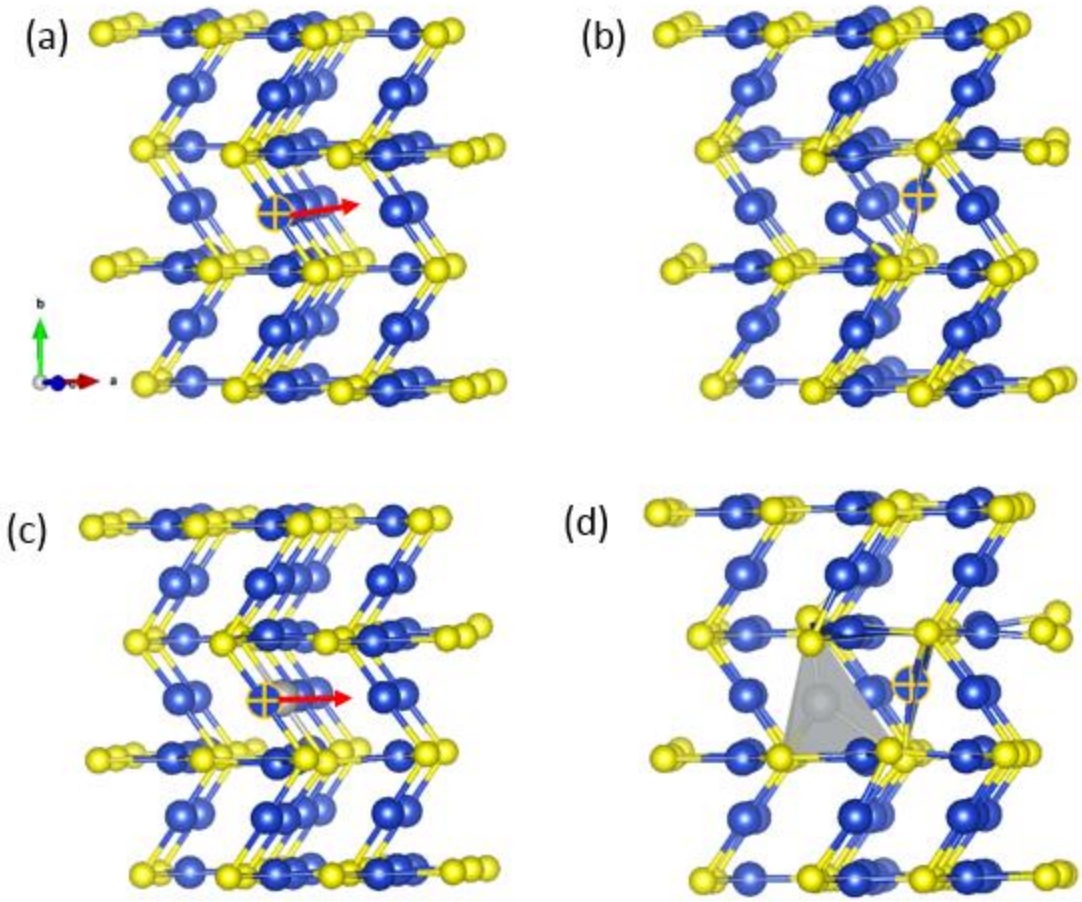

Figure 3. 12 (a) A fully relaxed Cu_2S structure where the cross marked Cu atom is chosen to be displaced from its original position to an interstitial site and the path is denoted with a red arrow, (b) a relaxed structure of Cu_2S after the Cu atom displaced from its original site. The displaced Cu atom makes a planer triangle with three nearby S atoms. (c) A Cu atom next to the cross marked Cu atom is replaced by an Ag atom and (d) a fully relaxed Ag doped structure where the cross marked Cu atom is displaced from its original position and stable at an interstitial site in the tunnel. The displaced Cu atom makes a planer triangle and the Ag atom makes a tetrahedra with nearby S atoms. Cu, S and Ag atoms are in blue, yellow and grey respectively.

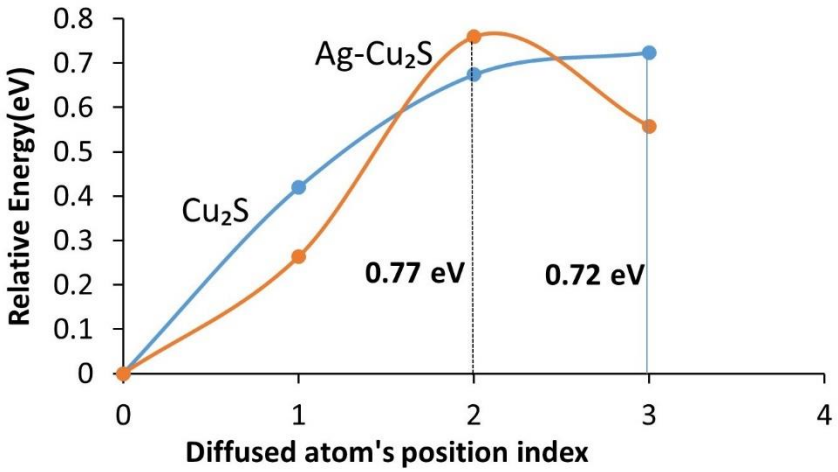

Figure 3. 13 Diffusion energy barrier of a Cu atom inside acanthite Cu_2S with and without Ag atom doped in a nearby site.

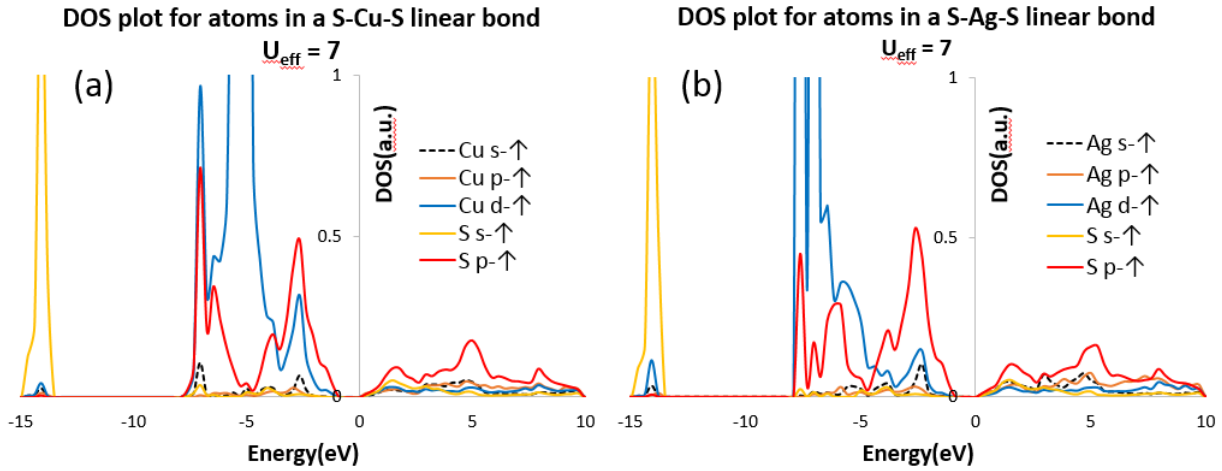

Figure 3. 14 DOS plots for atoms in a (a) S-Cu-S and (b) S-Ag-S linear bonds in an acanthite Cu_2S and Ag-doped Cu_2S crystal structure respectively. The DOS plots are calculated using GGA+U while U_{eff} = 7 has been used on both Cu-d and Ag-d.

From the DOS plots for atoms of S-Cu-S and S-Ag-S linear bonds in the crystal as in Figure 3. 14, it is seen that near the Fermi level S-p and Cu-d hybridization is stronger in the undoped crystal than the S-p and Ag-d hybridization in the Ag doped crystal. At the top of the valance band the Cu-d contribution is higher than Ag-d and Ag-s contribution is higher than Cu-s. It may be the reason that the Ag-S bond is more ionic in nature and Cu-S bond is more covalent. To justify this claim we calculate the charge density difference of the Ag doped crystal structure and find, from the 2D charge density difference plot (Figure 3. 15), that the contour lines around the Ag atom are more spherical meaning that the valance charge are centered around Ag more than that around a Cu atom. The more ionic bonding nature in S-Ag may require higher energy for a Cu atom to diffuse in the Ag doped environment since it requires higher energy for a bonded Ag atom to displace from its original site to facilitate a nearby Cu atom to diffuse. This higher diffusion energy in an Ag doped structure may limit the Cu diffusion inside the acanthite Cu_2S crystal.

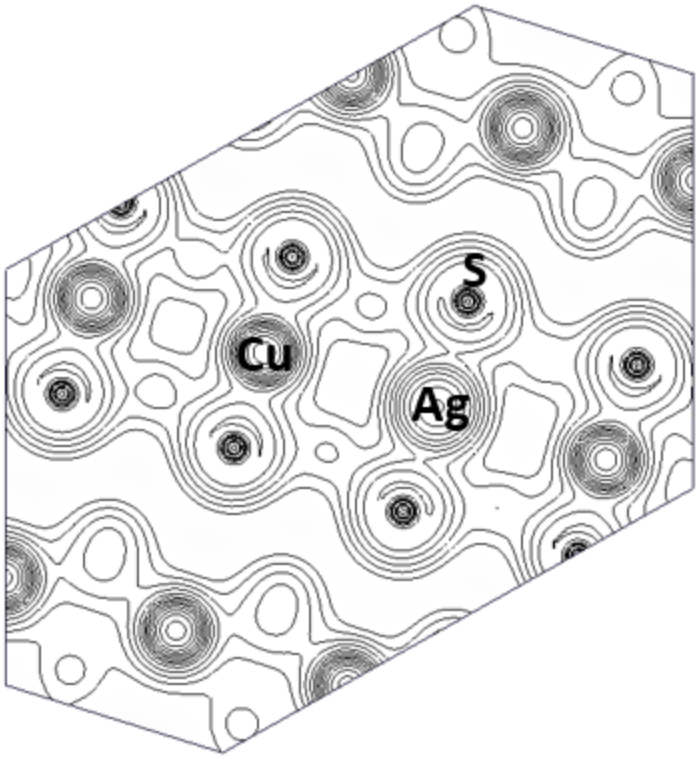

Figure 3. 15 2D charge density contour plot of an Ag atom doped Cu-S plane in acanthite Cu_2S crystal structure.

3.8 Conclusions

The focus of this study was to address the stability issue due to Cu vacancy formations in Cu_2S. To minimize Cu vacancy formations, two issues were addressed: Cu vacancy formation possibility and the Cu atom's diffusion. Reduced Cu diffusion is important since Cu vacancy forms within the bulk and if the vacancy forming Cu atom can be controlled with Ag doping so that Cu atom cannot leave the vicinity of the vacancy site, then it would most likely be recombined with the vacancy. In our study we have found that

Ag alloying with Cu in the acanthite phase of Cu_2S can help to reduce the vacancy formation probability and the alloy formation is also found to be thermodynamically favorable. From the energy barrier calculation, it was also evident that Ag atom doped in Cu place can help to reduce diffusion inside the crystal. The energy band gap of Ag alloyed structure which has less vacancy formation tendency is 0.93 eV which is higher than that of the pristine Cu_2S. This is an indication that Ag alloying may help to increase the band gap to maximize the photo conversion efficiency. Overall, Ag alloying in this regard will help to expand the capability of Cu_2S in photovoltaic applications.

Chapter 4

Thermodynamic stabilities and electronic structures of Sn doped Cu_2S

4.1 Introduction

Cu_xS ($1 \leq x \leq 2$) is an important low cost, non-toxic and earth abundant material. It has many stoichiometric and non-stoichiometric phases. There exist four different crystalline phases below 90°C. They are low chalcocite (Cu_2S) [38,39], djurleite ($Cu_{1.96}S$) [40], digenite ($Cu_{1.8}S$) [41], and anilite ($Cu_{1.75}S$) [42]. This material also exists in a solid-liquid hybrid form above 104°C, which is called high chalcocite or hexagonal phase [43], and at cubic phase above 436°C. Out of all the experimentally known phases, low chalcocite is the most stable stoichiometric phase at or below room temperature [35,36], and mostly known for its prospective photovoltaic application even though Cu vacancy induced instability was observed at Cu_2S active layer in Cu_2S/CdS heterojunction devices under ambient conditions [47,98–101]. In early 1980s, Cu_2S/CdS based thin film solar cells showed nearly 10% efficiency [102,103], but deterioration in device performance in the long term limit led to reduced interest later. Owing to not only earth abundance and non-toxicity but also suitable electronic properties, interest in this material for efficient and stable applications in photovoltaics is increasing again [48,50–55], where promising experimental mechanism to stabilize Cu_2S one atomic layer at a time has been reported [56]. In addition, our reported theoretical study on a newly identified bulk phase of Cu_2S which has an acanthite like crystal structure [37] has shown that Ag alloying can help to reduce the Cu vacancy formation tendency without altering

the electronic properties of the system [104]. However, finding a cost-effective alternative to Ag warrants more studies on the stability and electronic properties while alloying other materials at cationic sites. In this study, we will first establish that acanthite phase of Cu_2S which has a relatively simpler crystal structure can indeed be used to model low chalcocite phase. This will allow us to model complex doping, and alloying structures in low chalcocite supercells. We then dope Sn for Cu sites in this acanthite structure of Cu_2S and compare similar studies on low chalcocite. Sn has electronegativity of 1.96 and covalent radius of 139 pm while those for Cu are 1.90 and 132 pm, respectively.

Low chalcocite phase contains 96 Cu and 48 S atoms in its monoclinic unit cell, space group $P2_1/c$, has a complex crystal structure. The unit cell has symmetrically inequivalent 24 Cu and 12 S atoms. Hexagonal-closed-packed S atoms mainly build the frame of this structure while Cu atoms occupy triangular interstices [39]. On the other hand, DFT predicted acanthite phase of Cu_2S which was found thermodynamically more favorable in the stoichiometric limit than the low chalcocite phase in their ground states has only 8 Cu and 4 S atoms in its monoclinic unit cell [37]. In this structure, S atoms are five-fold coordinated with Cu atoms, different than the coordination in low chalcocite. However, half of the Cu atoms occupy triangular interstices like low chalcocite and other half form linear S – Cu – S bonds. The crystal structure of acanthite phase is presented in Figure 4. 1. The figure presents three planes of the crystal structure in a 3x2x2 supercell representation. In contrast to low chalcocite phase, the atoms in the acanthite phase have higher symmetry. Such higher crystalline order in acanthite phase facilitates higher control for doping other materials. Even though the crystalline order in low chalcocite is

less than acanthite phase, there is evidently some correspondence on atomic sites order between the two phases. The geometric correspondence is presented in Figure 4. 2. From Ab-initio molecular dynamics simulations at room temperature (27°C) for 3 ps, as modeled for both acanthite and

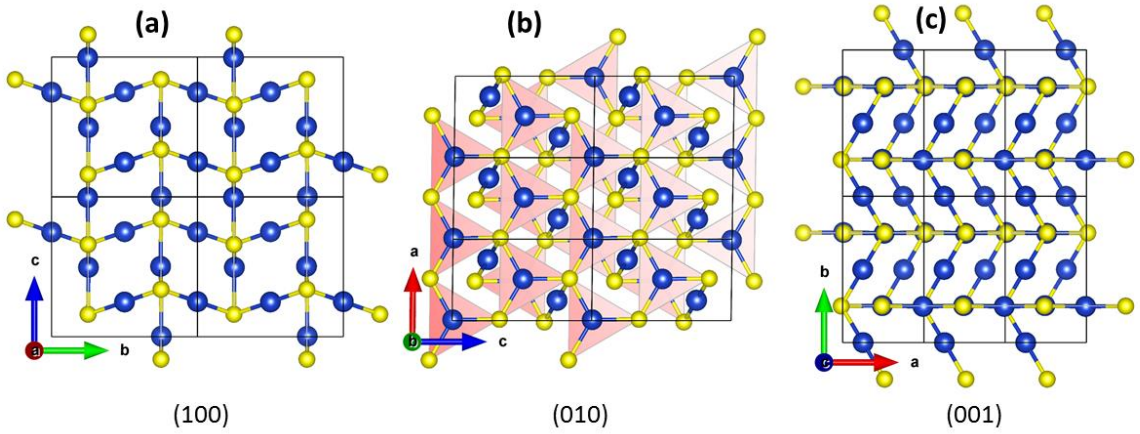

Figure 4. 1 The crystal structure of acanthite Cu2S along (a) (100), (b) (010), and (c) (001) planes. Cu and S atoms are in blue and yellow, respectively. For better visual, a 3x2x2 supercell is presented. Each box in solid black line represent a unit cell. S atoms are five-fold coordinated while half of the Cu atoms occupy triangular interstices and the other half forms S-Cu-S linear bonds in this structure.

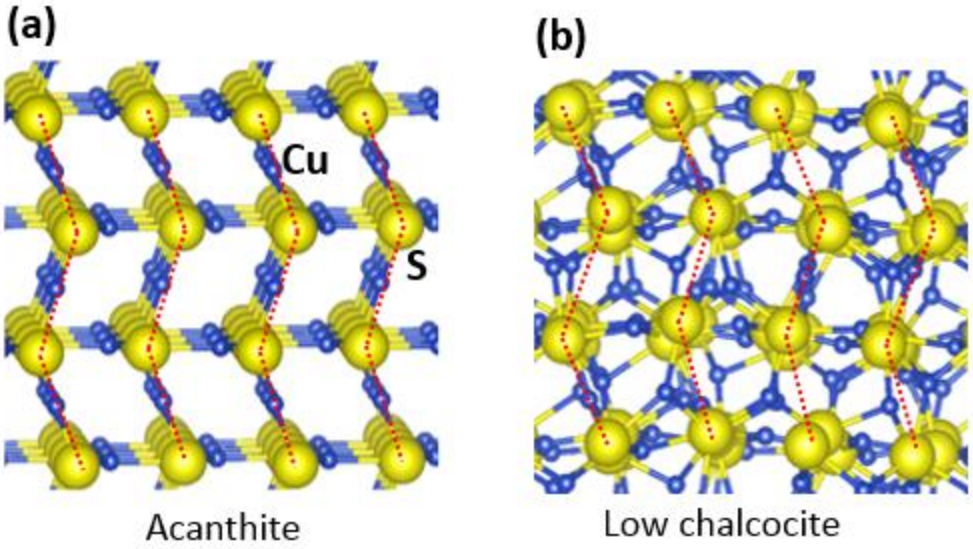

Figure 4. 2 Ionic arrangements of Cu and S atoms in (a) acanthite and (b) low chalcocite phases of Cu_2S. Cu and S ions are in blue and yellow, respectively. The figure shows that S ions mainly build the frame of the phases, where Cu ions are arranged in between S. In acanthite phase, S is well decorated with highly symmetric Cu. For low chalcocite phase, ions are distorted from highly symmetric sites. However, the layered arrangement of S ions is similar for both cases.

low chalcocite phases in Figure 4. 3, we have found that the packing of atoms in neighboring shells follow a similar trend for both structures. The total and partial radial distribution function (RDF) calculated for both, as in Figure 4. 4, evidently show that the atoms are packed in a similar fashion. Our calculated cumulative RDF, as in Figure 4. 5, also confirms the structural order, other than Cu atoms in low chalcocite phase beyond second nearest neighbor, follow almost a similar trend. The details for the average nearest neighbor (nn) distances up to 5^{th} nn can also be found in Figure 4. 6.

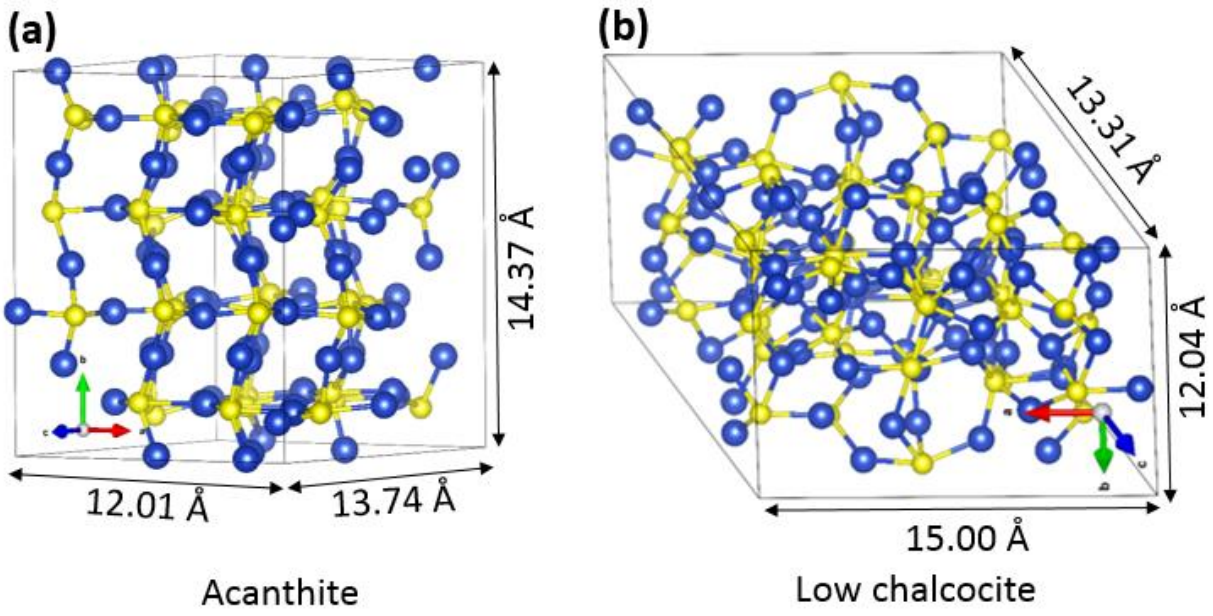

Figure 4. 3 Atomistic representation for Cu_2S (a) acanthite and (b) low chalcocite phases after Ab-initio molecular dynamics (AIMD) simulations at 300 K for 3 ps. Cu and S atoms are in blue and yellow, respectively. Both supercells contain 96 Cu and 48 S atoms. The maximum nearest neighbor distance is 2.54 Å for both structures, and the minima are 2.01 Å for acanthite and 2.06 Å for low chalcocite.

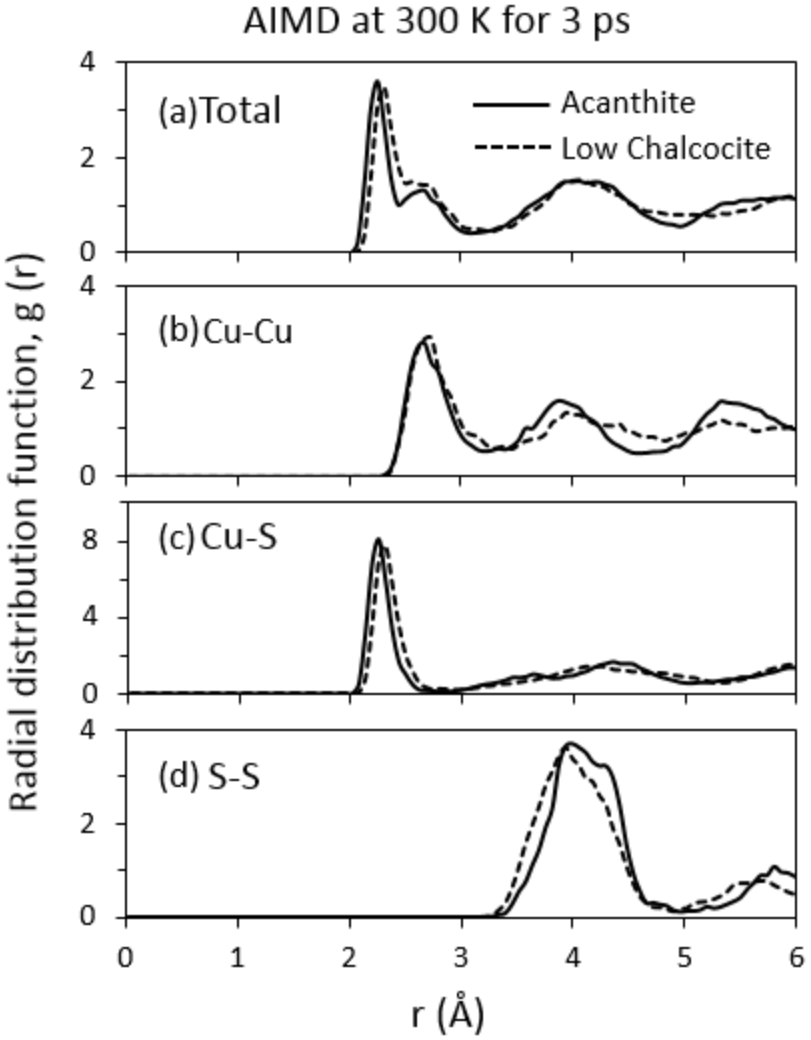

Figure 4. 4 The radial distribution function (RDF), g (r) for both acanthite and low chalcocite phases of Cu_2S: (a) total, (b) Cu – Cu, (c) Cu – S, and (d) S – S. Solid and dashed lines are for acanthite and low chalcocite phase, respectively. Ab-initio molecular dynamics were carried out for both phases at 300 K for 3 ps to examine the structural properties. The size of the supercells allows proper computation for radial distribution function up to r ~ 6 Å. Both structures show good correspondence on peak positions for both total and partial RDFs, meaning that the packing of atoms in neighboring shells follow a similar trend. This figures also shows that the effective width of atoms for both structures are very close. This can be understood from the minimum nearest neighbor distances as well. They are 2.01 Å for acanthite and 2.06 Å for low chalcocite.

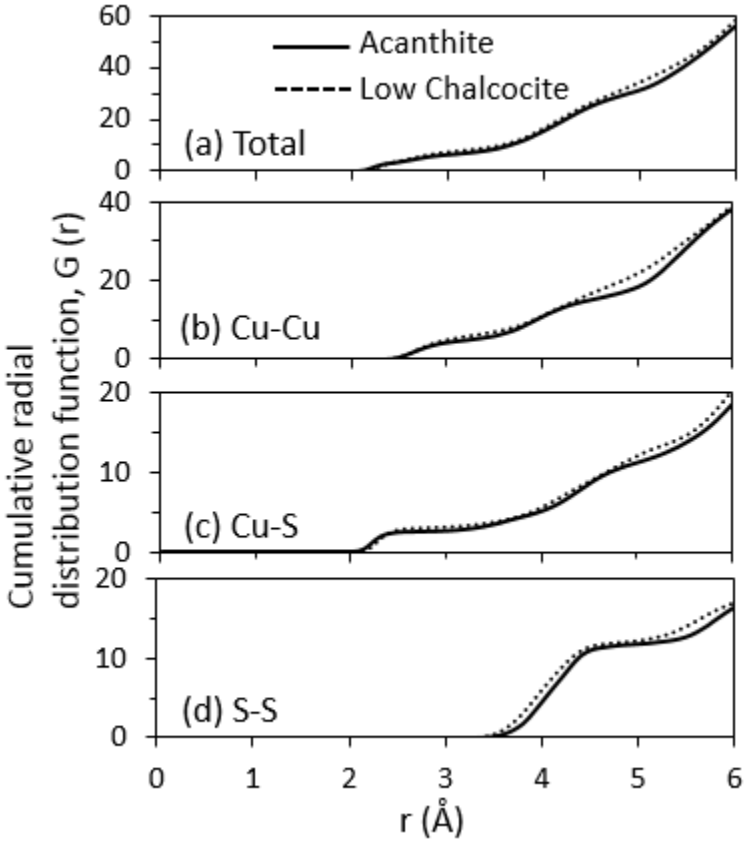

Figure 4. 5 The cumulative radial distribution function (RDF), G (r) for both acanthite and low chalcocite phases of Cu_2S: (a) total, (b) Cu – Cu, (c) Cu – S, and (d) S – S. Solid and dashed lines are for acanthite and low chalcocite phase, respectively. Ab-initio molecular dynamics were carried out for both phases at 300 K for 3 ps to examine the structural properties. The size of the supercells allows proper computation for radial distribution function up to r ~ 6 Å. The stepwise curves in the figure refer to good crystallinity. In particular, Cu – Cu partial G (r) curves show that Cu atoms in acanthite possess higher structural order beyond second nearest neighbor. For both phases, S atoms are highly ordered which is evident from (b) and (c). However, irrespective to the degree of crystallinity, both phases show overall good structural correspondence.

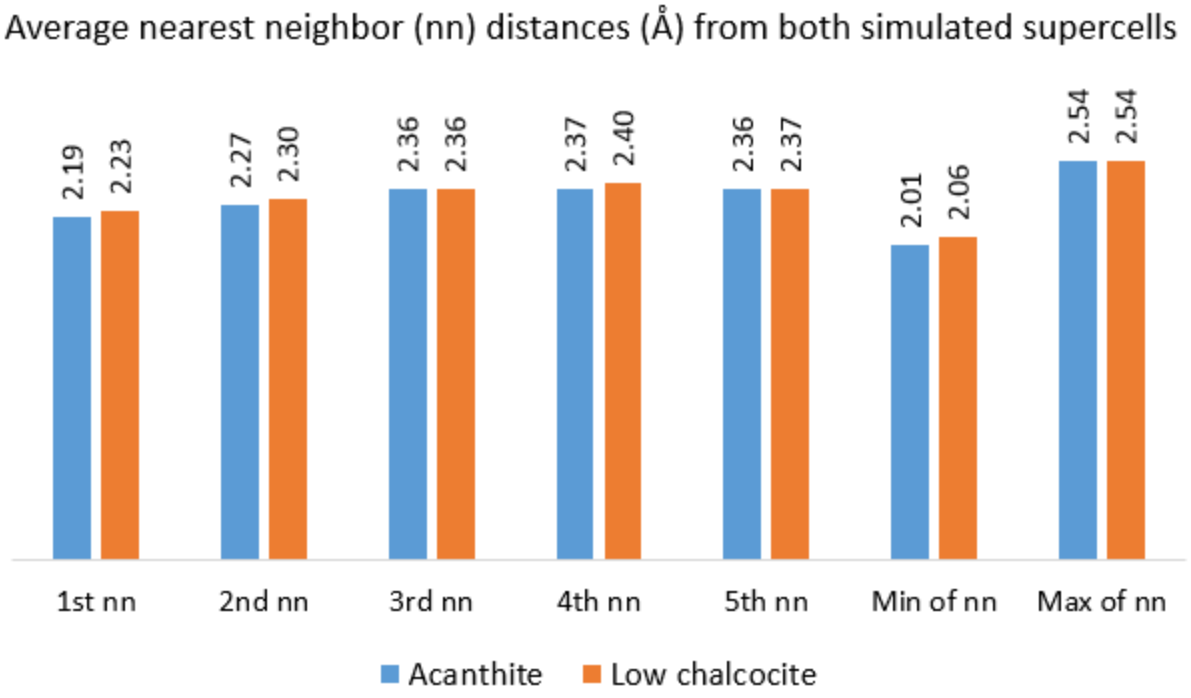

Figure 4. 6 Average nearest neighbor (nn) distances between atoms in acanthite and low chalcocite phases of Cu_2S, up to 5th nn along with the minimum and maximum values of nn.

For a single defect study involving a Cu site in low chalcocite crystal structure would require 24 inequivalent Cu sites to be dealt in 24 separate calculations. Such scenario increases the computational cost. In contrast to that, only two separate calculations are necessary for a single defect study in acanthite phase. To investigate if doping in two separate phases would result in similar outcomes, especially for the electronic structures and energy landscape, we have tested Sn doping in low chalcocite phase as well and compared with the cases of acanthite phase. This can be found in the later part of this manuscript. Hence, in this work, we are going to consider the acanthite phase for the defect and possible alloy studies. The study focuses on the stability and

electronic properties for substitutional Sn doping for Cu sites in the acanthite phase of Cu_2S.

4.2 Computational Methodology

The theoretical framework of this work is based on the density functional theory (DFT) [87,105] implemented with the projector augmented wave method (PAW) [91,106] as in Vienna ab initio simulation package (VASP) [89,90]. All the calculations in this work were spin polarized and the generalized gradient approximation (GGA) functional by Perdew–Burke–Ernserhof (PBE) [93,107] was used for the exchange-correlation energy. All the structures in this work were geometrically optimized without any symmetry constraint. The convergence criteria for the electronic self-consistent loop was set equal to or less than 1E-06 eV. All the ions were relaxed until the Hellman-Feynman force was equal to or less than 0.01 eV/Å. The kinetic energy cut off for the plane wave basis set was 520 eV. Cu $3d^{10}$ $4s^1$, S $3s^2$ $3p^4$ and Sn $4d^{10}$ $5s^2$ $5p^2$ are the valance electrons configurations considered for this work. Since it is well-known that GGA-DFT underestimates band gaps, we have applied the rotationally invariant form of GGA + U, formulated by Dudarev et al. [79], which adds a Hubbard parameter U with the standard GGA to enhance the on-site Coulomb interaction. In our study, U parameter is used for electronic structure calculations only. U_{eff} (U – J) = 7 is applied on Cu *d,* and 4 on Sn *p*. The justification for the U value on Cu *d* can be found from a previous study as in ref. [104]. The band structures for all the acanthite structures were calculated along A(1/2,1/2,0) - X(0,1/2,0) - Γ(0,0,0) - Z(1/2,0,0) - D(1/2,0,1/2) - M(1/2,

0.496, 0.512) high symmetry points. The symmetry points for an acanthite Cu_2S crystal structure was calculated by AFLOW [108]. The Brillouin zone for all the supercells was sampled by a 7x3x3 gamma centered k-mesh. For visualization, VESTA [109] was used throughout the work.

A 2x2x2 supercell of acanthite Cu_2S was considered to model Sn alloyed structures. The pristine supercell contains 64 Cu and 32 S atoms. For Sn substitution in Cu places, one to ten Sn atoms were considered and doped in different combination and configurations to search for thermodynamically stable $Cu_{2-x}Sn_xS$ structures. The energies of formation for $Cu_{2-x}Sn_xS$ structures were calculated using the following formula:

$$E_f = E_{tot}(Cu_{2-x}Sn_xS) - E_{tot}(Cu_2S) + n(\mu_{Cu} + \Delta\mu_{Cu}) - n(\mu_{Sn} + \Delta\mu_{Sn}) \quad (4.1)$$

which requires following Equation (4.4.2) and (4.) to be satisfied

$$\Delta H_{Cu_2S} = 2\Delta\mu_{Cu} + \Delta\mu_S \quad (4.2)$$

$$\Delta H_{Cu_{2-x}Sn_xS} = (2-x)\Delta\mu_{Cu} + x\Delta\mu_{Sn} + \Delta\mu_s \quad (4.3)$$

Where $E_{tot}(Cu_{2-x}Sn_xS)$ and $E_{tot}(Cu_2S)$ are total energies of Sn alloyed and pristine Cu_2S supercell structures, respectively. μ_{Cu}, μ_{Sn} and μ_S are the chemical potentials for Cu, Sn and S respectively, which were taken to be equal to the energy per atom in their bulk states. *n* is the number of atoms taken out or doped in the system. The energy of formation gives a thermodynamic measure for the energy cost of Sn doping in a host

structure. The formation enthalpies for pristine and $Cu_{2-x}Sn_xS$ structures were calculated by

$$\Delta H_{Cu_2S} = E(Cu_2S) - 2\mu_{Cu} - \mu_S \quad (4.4)$$

$$\Delta H_{Cu_{2-x}Sn_xS} = E(Cu_{2-x}Sn_xS) - (2-x)\mu_{Cu} - x\mu_{Sn} - \mu_S \quad (4.5)$$

Where $E(Cu_2S)$ and $E(Cu_{2-x}Sn_xS)$ are the total energies of the pristine and alloyed systems per formula unit. The formation enthalpy provides information about the thermodynamic stability of a system. The lower is the enthalpy of a system, the higher is the thermodynamic stability.

For the investigation of the structural properties, ab-initio molecular dynamics (AIMD) simulations were carried out for both acanthite and low chalcocite phases of Cu_2S with PBE-GGA functional as implemented in VASP. Since a low chalcocite unit cell contains 96 Cu and 48 S atoms, to compare the dynamical evolution of acanthite phase with low chalcocite, a 3x2x2 acanthite supercell of Cu_2S containing the same number of atoms was made. Both systems could evolve at 300 K for 3 ps. The simulations were carried out in NVT ensembles and the temperature was set with Nose-Hoover thermostat. The Brillouin zone was sampled with only Γ-point for both structures.

4.3 Sn doping in Cu_2S: $Cu_{2-x}Sn_xS$

One to ten number of Sn atoms are doped in different configurations on a Cu plane of 28 atoms in 2x2x2 acanthite supercells. Since doping sites may have numerous

combinations, and testing all possible cases would be computationally expensive, we doped Sn atoms from nearest to furthest Cu sites possible in this case. Based on DFT calculated formation enthalpies and energies of formation, ground state energy structures for different Sn concentrations were found. Since our test structures are limited in numbers, the least energy structures for higher Sn concentrations may not be the actual ground state structures. However, the structures filtered from the energy landscape should give enough information if Sn doping in this phase is thermodynamically favorable. For a single Sn doping, two inequivalent Cu sites can be considered. A Cu atom in the crystal may either form an S – Cu – S linear bond or occupy an interstitial triangular site with three S atoms at vertices. The calculated formation enthalpy difference per formula unit between these two structures of $Cu_{1.97}Sn_{0.03}S$ is very small, only 2 meV. For higher Sn concentrations, at least ten test structures were made. Then total energies of the fully relaxed systems were calculated. The formation enthalpies (calculated from Equation 4 and 5) and energies of formation (Equation 4.1) are presented in Figure 4. 7. The energies of formation per Sn atom at Cu rich and poor conditions were calculated for the least energy structures only. Figure 4. 7(b) shows that Sn doping at Cu poor is always favorable than Cu rich condition and becomes thermodynamically favorable when number of Sn atoms is equal to or higher than 4. As Sn concentration increases, the energy cost for Sn doping decreases. In this study, the most stable structure is found for 10 Sn atoms doped structure, $Cu_{1.69}Sn_{0.31}S$. To check if Sn doping in low chalcocite phase follows a similar trend, we doped one to three Sn atoms for different Cu sites and found that Sn doping formation energy decreases as Sn concentration increases for both Cu rich and poor conditions. The energy landscape is presented in Figure 4. 8.

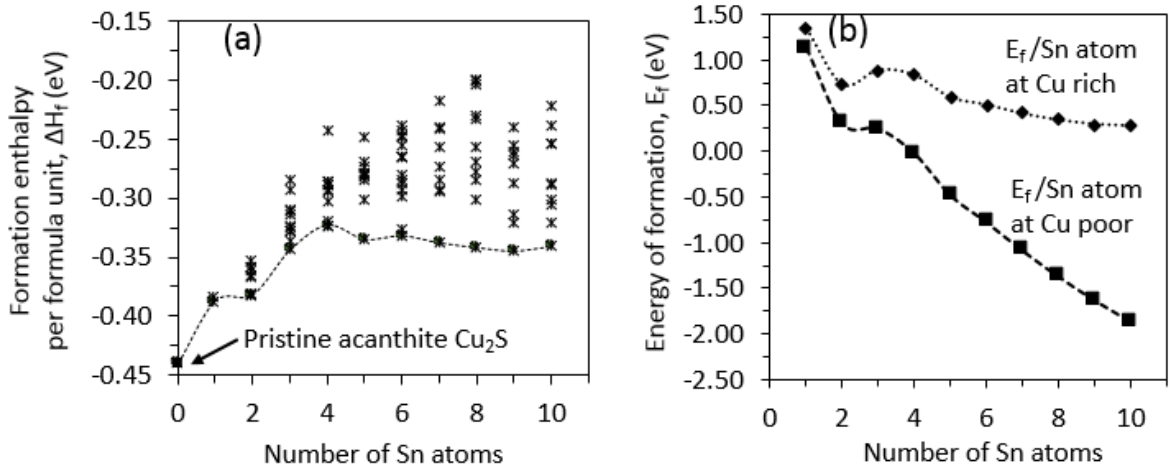

Figure 4. 7 (a) Formation enthalpy per formula unit, and (b) energy of formation per Sn atom per supercell at Cu rich and poor condition for $Cu_{2-x}Sn_xS$ structures. Formation enthalpy per formula unit is the lowest for the pristine structure and increases as higher number of Sn atoms doped for Cu sites.

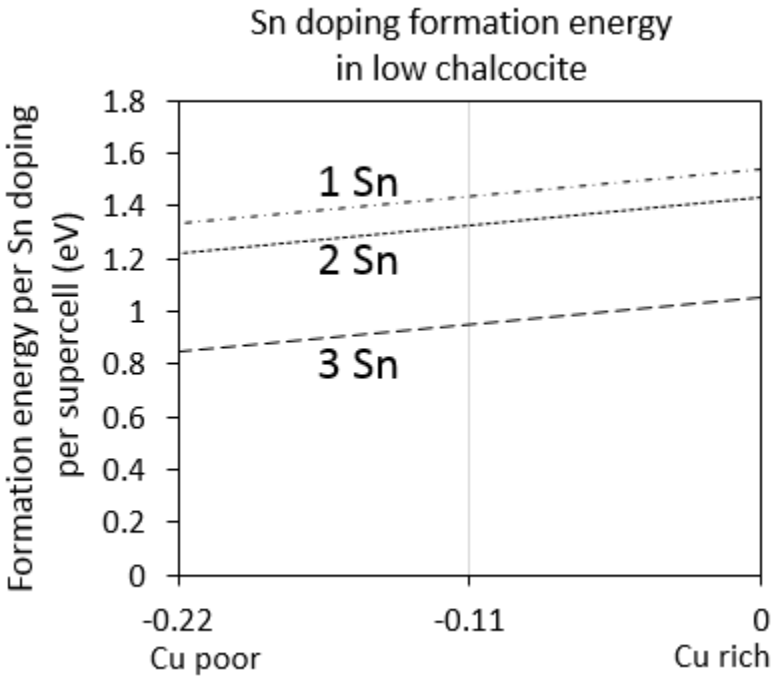

Figure 4. 8 Formation energy for Sn doping in low chalcocite calculated per Sn atom in a 144-atom crystal structure. The formation energy landscape shows that thermodynamic cost decreases as number of Sn atoms increases, which follows a similar trend like Sn doping in acanthite structures.

4.3.1 Single-phase stability of $Cu_{2-x}Sn_xS$

In addition, we have also calculated the single-phase stability zone for Sn doped acanthite systems, $Cu_{2-x}Sn_xS$ for x = 0.03, 0.19 and 0.31 to check if secondary sulfide phases are formed by Cu and Sn cations which may co-exist at any given growth conditions. To do this, we have considered possible compounds such as pure acanthite Cu_2S, low chalcocite Cu_2S, α-SnS, β-SnS, SnS_2, Sn_2S_3 and Cu_2SnS_3. To avoid these possible secondary phases to occur in the equilibrium growth condition of $Cu_{2-x}Sn_xS$ the following conditions need to be satisfied:

Acanthite Cu_2S: $2\Delta\mu_{Cu} + \Delta\mu_S < \Delta H_{Cu_2S} = -0.44$ (4.6)

Low chalcocite Cu_2S: $2\Delta\mu_{Cu} + \Delta\mu_S < \Delta H_{Cu_2S} = -0.41$ (4.7)

Cu_2SnS_3: $2\Delta\mu_{Cu} + \Delta\mu_{Sn} + 3\Delta\mu_S < \Delta H_{Cu_2SnS_3} = -2.11$ (4.8)

α-SnS: $\Delta\mu_{Sn} + \Delta\mu_S < \Delta H_{\alpha-SnS} = -0.97$ (4.9)

β-SnS: $\Delta\mu_{Sn} + \Delta\mu_S < \Delta H_{\beta-SnS} = 0.03$ (4.10)

SnS_2: $\Delta\mu_{Sn} + 2\Delta\mu_S < \Delta H_{SnS_2} = -1.24$ (4.11)

Sn_2S_3: $2\Delta\mu_{Sn} + 3\Delta\mu_S < \Delta H_{Sn_2S_3} = -2.19$ (4.12)

To form a stable $Cu_{2-x}Sn_xS$ system in equilibrium, Equation (4.4.3) has to be satisfied where the upper and lower bounds for each atomic species are following:

$$\frac{\Delta H_{Cu_{2-x}Sn_xS}}{2-x} \leq \Delta\mu_{Cu} \leq 0\ eV \quad (4.13)$$

$$\frac{\Delta H_{Cu_{2-x}Sn_xS}}{x} \leq \Delta\mu_{Sn} \leq 0\ eV \quad (4.14)$$

$$\Delta H_{Cu_{2-x}Sn_xS} \leq \Delta\mu_{S} \leq 0\ eV \quad (4.15)$$

The calculated chemical potential landscapes for three cases (x = 0.03, 0.19 and 0.31) are presented in Figure 4. 9. The respective formation enthalpies for such $Cu_{2-x}Sn_xS$ systems are -0.3940, -0.3415 and -0.3516 eV, respectively.

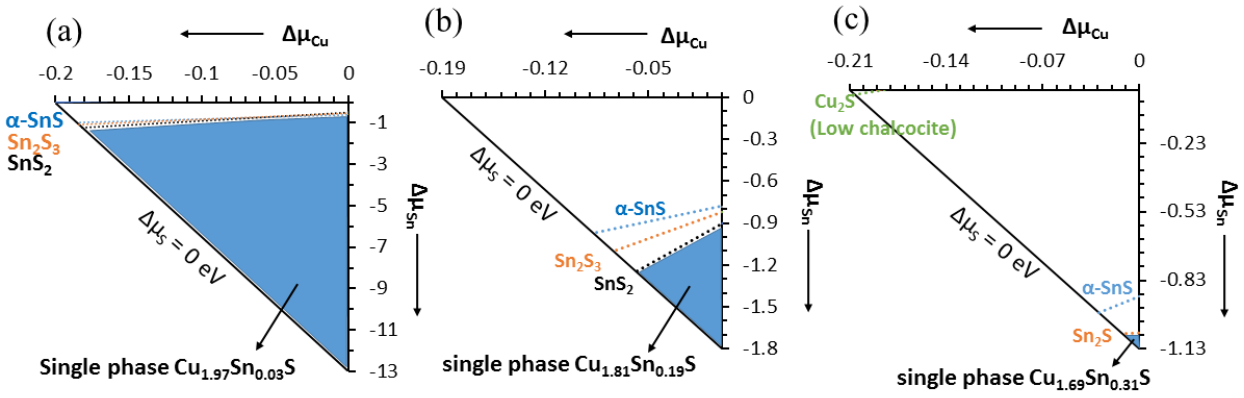

Figure 4. 9 Chemical potential landscape for the Sn doped acanthite Cu_2S systems, $Cu_{2-x}Sn_xS$, for (a) x = 0.03, (b) x = 0.19 and (c) x = 0.31 calculated at thermodynamic equilibrium conditions and represented with triangles. The shaded area represents the single-phase stability zone for $Cu_{2-x}Sn_xS$ and the dotted lines are for the possible secondary phases which may occur during doped systems formation.

The reason that three different Sn doping concentrations are considered here is to check how the stability zone along with secondary phases change as Sn doping concentration increases from the lowest to the highest doping limit. The figure shows that the area for the single-phase stability zone (blue shaded area) decreases as Sn doping

concentration increases. For the first two cases (x = 0.03 and 0.19), the possible secondary phases that may form are α-SnS, SnS_2 and Sn_2S_3. In this case, no Cu_2S phases, either acanthite or low chalcocite is found, as well as, β-SnS and Cu_2SnS_3 do not appear within the triangle. The single-phase stability zone for $Cu_{1.97}Sn_{0.03}S$ and $Cu_{1.81}Sn_{0.19}S$ are significantly large. For the first case, Cu1.97Sn0.03S, the single phase stability zone forms within the area enclosed by the vertices (0, -0.53), (0, -13) and (-0.18, -1.13) while for $Cu_{1.81}Sn_{0.19}S$, these are (0, -0.9), (-0.05, -1.25) and (0, -1.8). On the other hand, when Sn doping concentration is increased to 10.42% (x = 0.31), low chalcocite phase formation is visible for $\Delta\mu_{Cu}$ ≤ -0.19 eV which is very close to Cu poor and Sn rich limit. However, the zone area for low chalcocite phase is negligible. The single-phase stability zone in this case is quite small compared to the previous case. The zone is visible near the Cu rich and Sn poor limit only. The reason that the area in this case appears even at Sn poor limit is probably since higher concentration of Sn in the system distorts the local doped environment more and facilitates higher portion of secondary sulfide phases to form. In addition, only α-SnS and Sn_2S_3 phases are found in the triangle and β-SnS, SnS_2 and Cu_2SnS_3 do not appear within the given thermodynamic conditions. Out of the three-doping scenario, it is evident that the least number of Sn doping in the systems results in the highest probability for single-phase stability of a Sn doped system at a given growth condition.

4.3.2 Electronic structures of $Cu_{2-x}Sn_xS$

Since we have now established that Sn doping for Cu sites in acanthite Cu_2S is thermodynamically favorable, we are now interested to the electronic structures for $Cu_{2-x}Sn_xS$. The GGA + U calculated band structures for different Sn concentrations are presented in Figure 4. 10. It is found that Sn doping introduces defect bands at or near the Fermi level. Similar outcome is also found for Sn doped low chalcocite phase as in Figure 4. 11. As the doping concentration increases, number of defect bands also increases. Note that, defect bands in Figure 4. 10(a) and (b) are found for one and two Sn doped structures, respectively.

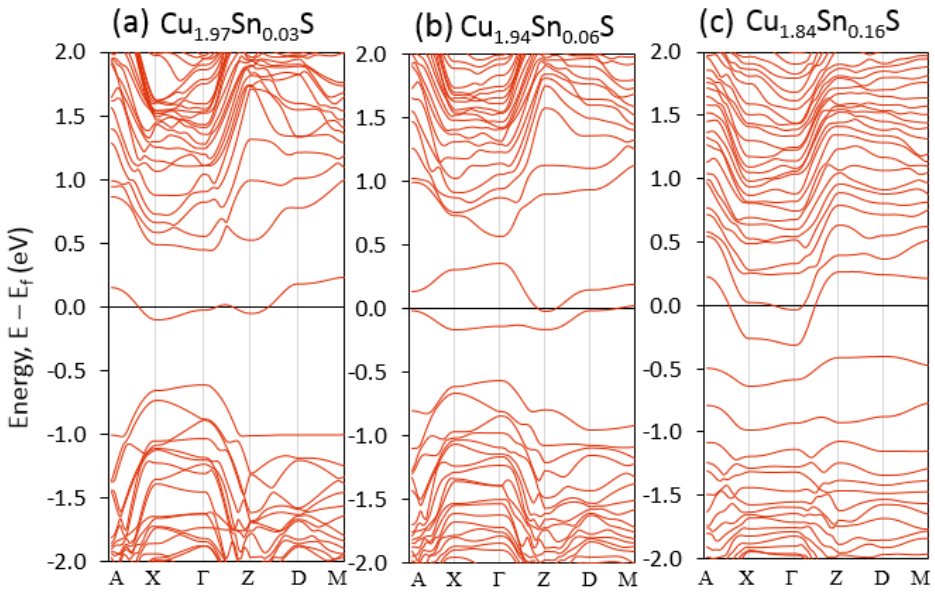

Figure 4. 10 GGA + U calculated band structures for Sn doped acanthite Cu_2S. U_{eff} = 7 and 4 are applied on Cu d and Sn p, respectively. The Fermi level is set at 0 eV. $Cu_{2-x}Sn_xS$ structures for (a) one, (b) two, and (c) five Sn atoms doped cases are presented here to show the doping effect. As it can be seen, Sn doping introduces defect bands at or near the Fermi level. The number of defect bands increases as Sn concentration increases.

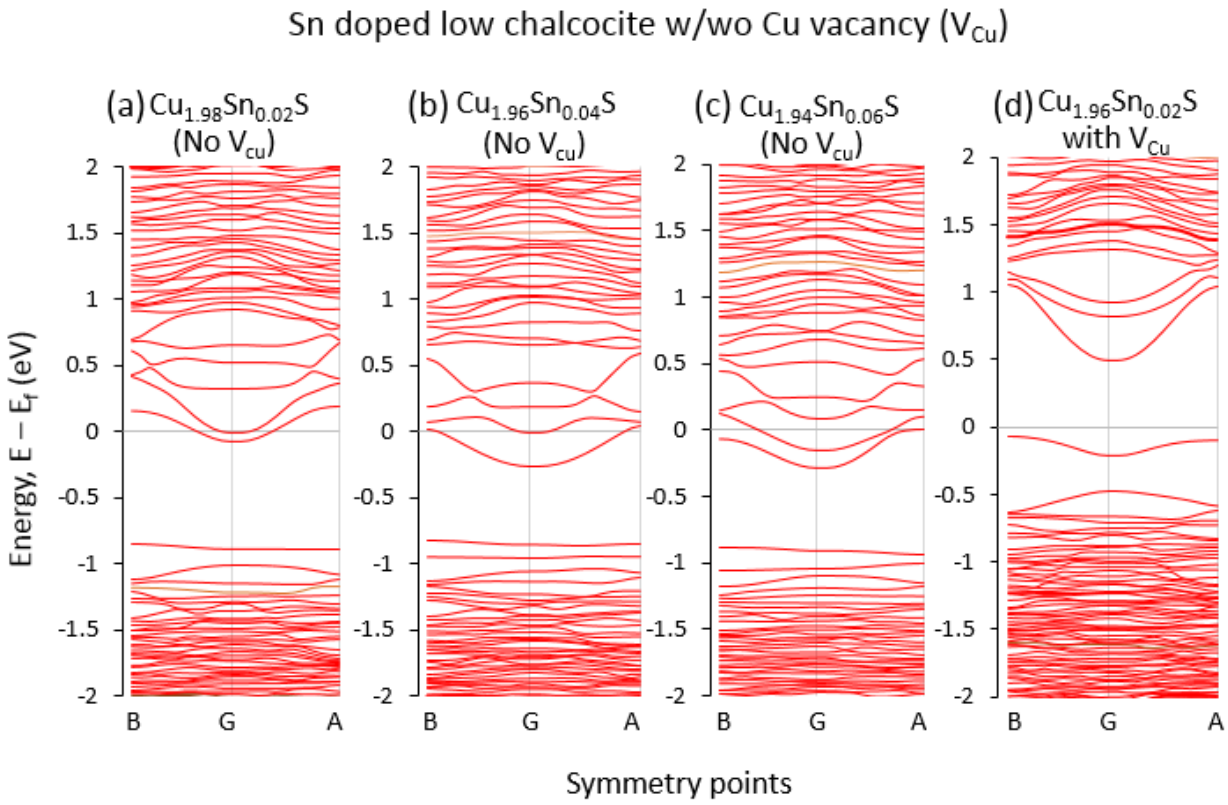

Figure 4. 11 GGA+U (U = 8 on Cu d and 5 on Sn p, J = 1) calculated band structures for Sn doped low chalcocite structures. (a) One, (b) two, and (c) three Sn atoms doped for Cu sites in a 144-atom low chalcocite structure. (d) One Sn atom is doped along with a Cu vacancy in same size cell. The figures show that Sn doping introduces defect bands below the Fermi level. Generous contributions from doped Sn occupy the bottom of the conduction band and pulls down the states at or below the Fermi level. The defect states are generally composed of heavily hybridized Cu d, Sn p and S p states. The number of defect bands increases with higher Sn doping concentrations. (d) The band structure for $Cu_{1.96}Sn_{0.02}S$ shows that the defect band generated from the combined effect of Sn doping and Cu vacancy is just below the Fermi level. The Fermi level is set at 0 eV.

To understand the nature of the defect bands as to how they originate and their contribution in the lattice, we calculated the band decomposed charge density, partial density of states (p-DOS) and the partial orbital contribution associated to the defect bands for the first two cases of Figure 4. 10. The details are presented in Figure 4. 12 and Figure 4. 13. The band decomposed charge density isosurface for both cases show

that the defect bands are mainly due to the charges accumulated around the doped Sn atoms. Contributions from Cu and S atoms in the doping environment are less. Neighboring Cu and S atoms displaced from their original lattice sites due to the doping effect gain little charge in their basins. As a result, the contributions from nearby atoms add up and eventually contribute to defect bands. This can be understood better from the partial density of states plots. Figure 4. 12(b) and Figure 4. 13(b) show the predominant contribution to the defect bands are from Sn p and Cu d orbitals. However, Cu p and S p also contribute significantly. Here, it is worth to mention that, the top of the valance bands for both pristine acanthite [104] and low chalcocite (Figure 4. 14) are dominated by Cu d. The second dominant contribution is from S p which hybridize with Cu d. This is a common characteristic in other Cu-chalcogenides such as CZTS [110], $CuGaS_2$, $CuInS_2$ etc. as well [71,111–114]. Interestingly, the bottom edge of the conduction band in acanthite is composed of Cu p. A little above the conduction band edge, Cu s and d hybridize with S p. The details about the conduction band edge will be discussed later. Since the defect bands shown in the figures are composed of both occupied and unoccupied states, where the empty states from bottom of the conduction bands get occupied partially or in full depending on the doping concentrations, almost all orbitals are present at the Fermi level as defect states. To quantify the orbital contribution in defect states further, we calculated the percentage of s, p, and d character of the defect bands for each k-point along the symmetry lines from orbital-projected wave functions for the above mentioned two cases. Figure 4. 12(c) shows that the single defect band is 66% p, 24% d, and only 10% s. When number of Sn atoms are doubled, p contribution is not affected much. Figure 4. 13(c) shows two defect bands are 63% p, 27% d, and 10% s in character. The d contribution increases when Sn atoms are doubled since Sn doped local environment is distorted more. Consequently, higher number of Cu atoms are displaced from their original lattice sites which eventually introduce Cu d character in defects. Also, Sn d contribution increases with higher number of Sn atoms. As it can be found from the band structures in Figure 4. 10, number of defect bands increases with higher number of Sn atoms, and the doped material starts to behave almost metallic for $Cu_{1.84}Sn_{0.16}S$. It is known that the digenite phase ($Cu_{1.84}S$) is metallic due to its highly p-type nature [36]. In the acanthite phase, when Sn is doped for Cu sites, higher doping concentrations make

the material metallic as well, but it possesses now n-type characteristics. The nature of defect bands for Sn doped low chalcocite phase is like the Sn doped acanthite phase as well, which can be found in detail from the density of states plot as presented in Figure 4. 15.

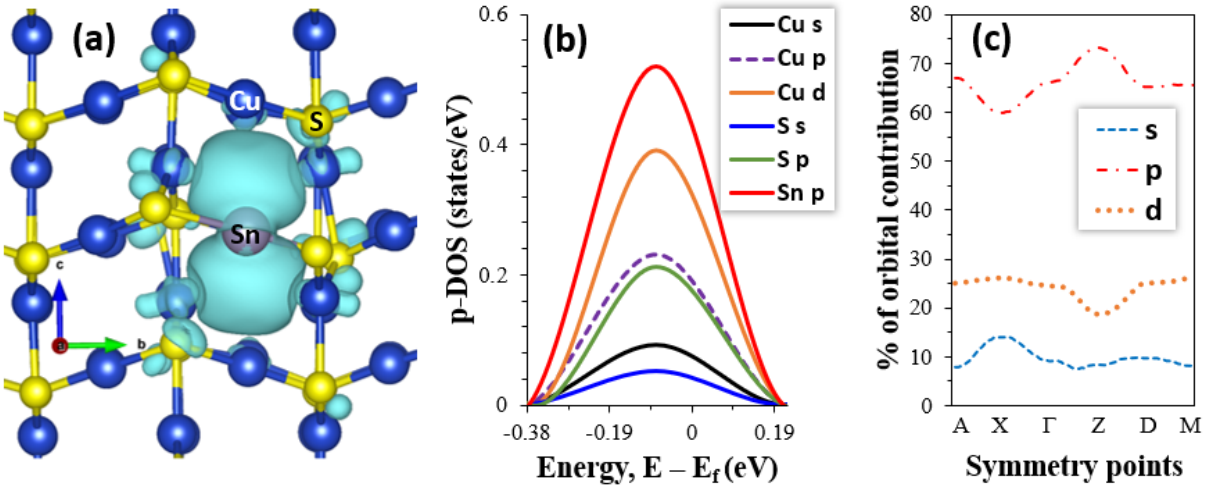

Figure 4. 12 (a) Band decomposed charge density isosurface (∼10% of the maximum density) for the defect band, originated due to a single Sn atom doped for a Cu site in acanthite Cu_2S supercell, $Cu_{1.97}Sn_{0.03}S$. The band decomposed charge density is calculated for all the k-points along the symmetry lines used in the band structure calculations. This figure shows that the defect band is mainly due to the substituted Sn atom and the lattice distortion created due to the substitution. Cu and S atoms contributing to the defect band are displaced from their original sites to some extent. (b) The partial density of states (p-DOS) derived from GGA + U DOS calculation for the whole cell, $Cu_{1.97}Sn_{0.03}S$, shows that Sn p and Cu d dominate the defect band while (c) the defect bands decomposed partial orbital calculations show that p orbital contribution is about 66%. d and s orbitals contribute nearly 24% and 10%, respectively.

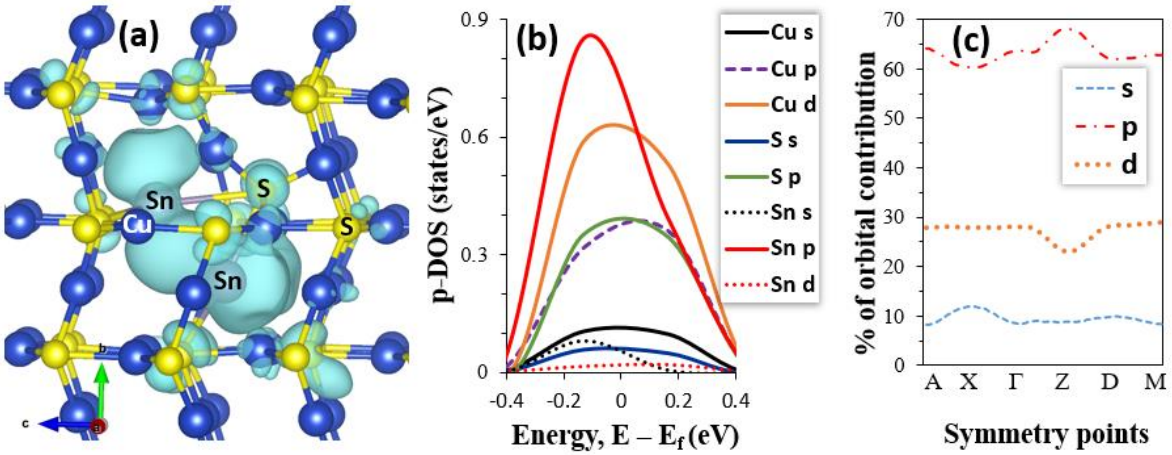

Figure 4. 13 (a) Band decomposed charge density isosurface (∼10% of the maximum density) for defect bands located at the Fermi level, originated due to 2 Sn atoms doped for two Cu sites in acanthite Cu_2S supercell, $Cu_{1.94}Sn_{0.06}S$. This defect bands decomposed charge density is calculated for all the k-points along the symmetry lines used in the band structure calculations. This figure shows that the defect band is mainly due to the substituted Sn atoms and the lattice distortion created due to this substitution. Cu and S atoms contributing to the defect band are displaced from their original sites to some extent. (b) The partial density of states (p-DOS) derived from GGA + U DOS calculation for the whole cell, $Cu_{1.94}Sn_{0.06}S$, shows that Sn p and Cu d dominate defect bands while (c) the defect bands decomposed partial orbital calculations show that p orbital contribution is about 63%. d and s orbitals contribute nearly 27% and 10%, respectively.

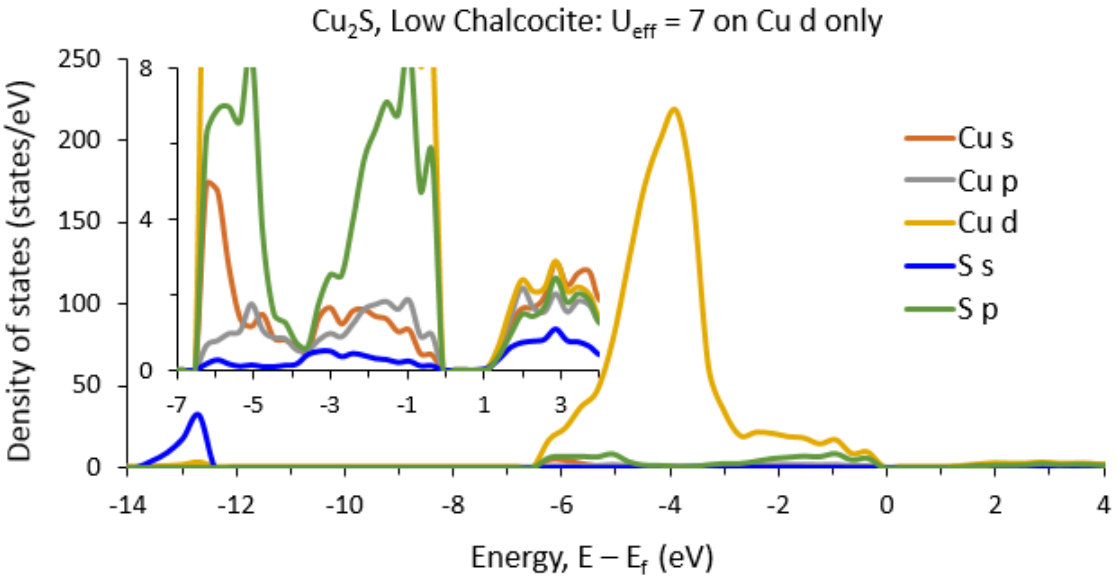

Figure 4. 14 GGA + U (U = 8 on Cu d and J = 1) density of states (DOS) plot for the low chalcocite phase of Cu_2S. Inset is the magnified partial density of states plotted from a 144-atoms unit cell. The Fermi level is set at 0 eV.

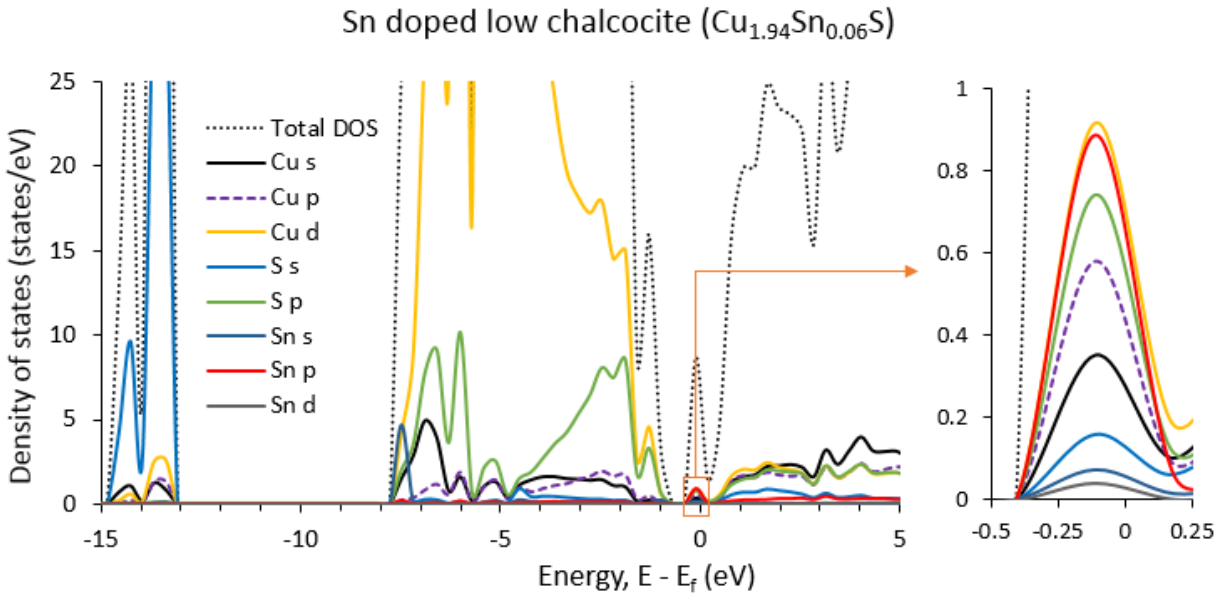

Figure 4. 15 GGA + U (U = 8 on Cu d and 5 on Sn p, J = 1) calculated density of states (DOS) plot for a low chalcocite system doped with Sn atoms ($Cu_{1.94}Sn_{0.06}S$). Inset is the magnified view of the defect states of the system. It shows that the top of the valance band is mostly composed of Cu d and S p as like the pristine case. The defect bands

created due to Sn doping is mainly composed of heavily hybridized Cu d, Sn p and S p. The contribution from Cu s and p at the defect level is also appreciable. However, the overall composition of the defect states due to Sn doping in low chalcocite system is very similar to the case of acanthite phase.

4.3.3 Charge states of Cu, S and Sn in crystal structures

Table 4. 1 DFT calculated Bader charge states in electronic charge unit (e) for atomic species in pristine and doped crystals of acanthite Cu_2S.

		Average Bader Charge states (*e*)		
Number of Sn atoms	Crystal stoichiometry	Cu	S	Sn
0	Cu_2S	+ 0.37	- 0.75	
1	$Cu_{1.97}Sn_{0.03}S$	+ 0.37	- 0.74	+ 0.66
5	$Cu_{1.84}Sn_{0.16}S$	+ 0.36	- 0.75	+ 0.57
10	$Cu_{1.69}Sn_{0.31}S$	+ 0.33	- 0.76	+ 0.62

To explore the above behavior, we need to understand the cationic role of Sn atom in the crystal structure. Hence we employed Bader charge analysis [115–118] to get the charge states of the atomic species in pristine and doped crystal structures, which is reported in Table 4. 1. The table shows that the average charge states for Cu and S in pristine crystal are + 0.37 e and – 0.75 e, respectively. They remain almost unchanged for Sn doped crystals. However, the charge state for Sn atoms is almost twice of Cu. A similar scenario is also found for Sn doped low chalcocite phase as given in Table 4. 2. It

shows that Sn donates twice as much electrons than corresponding the Cu atom, to the bonded S atom. Hence, a substitutional Sn atom for Cu site creates charge defects to some extent. This extra charge from Sn is accumulated in the doping environment and creates defect bands. From the band structure plots as in Figure 4. 10, it can be found that the defect bands are derived from the bottom of the conduction band. In our band structures, the bands below Fermi level (E_f) are all occupied, and above are all empty. A defect band at the Fermi level is composed of occupied and unoccupied states. Hence, it can be stated in short that a Sn atom provides extra electrons which eventually occupy empty bands from the bottom of the conduction band. As a result, when Sn concentration increases, more empty bands are occupied and pulled down to the Fermi level, which eventually fill up the band gap. This phenomenon leads to a metallic characteristic for highly doped systems.

Table 4. 2 The GGA-DFT calculated Bader charge states for species in low chalcocite systems with and without Sn doping. It shows that the average charge states of Sn in the system are almost twice of Cu atoms which is like the case of Sn doping in acanthite phase of Cu_2S. As Sn doping concentration varies, overall charge states remain similar.

		Average Bader Charge states (e) in Low chalcocite		
Number of Sn atoms	Crystal stoichiometry	Cu	S	Sn
0	Cu_2S	+ 0.38	– 0.76	
1	$Cu_{1.98}Sn_{0.02}S$	+ 0.38	– 0.76	+ 0.72
2	$Cu_{1.96}Sn_{0.04}S$	+ 0.38	– 0.79	+ 0.76
3	$Cu_{1.94}Sn_{0.06}S$	+ 0.37	– 0.76	+ 0.61

4.3.4 Conduction band-edge of $Cu_{2-x}Sn_xS$

At this point, we come back again to study the composition of the bottom of the conduction band of a Sn doped system. To do this in the simplistic form, we compare the band decomposed charge density of the first conduction band from a pristine system with the same from a single Sn doped system. Details are presented in Figure 4. 16 (a, b). The figures show that the first conduction band in pristine Cu_2S are mainly contributed by charges around S atoms and interstitial sites. On the other hand, when a Sn atom is doped for a Cu site, the doped atom with distorted neighbors and highly accumulated interstitial charges make the first conduction band. In Figure 4. 16 (c, d), it is found that the orbital contribution changes along the symmetry lines. Around Γ point, total s and d contributions are the maximum while p is the minimum. This explains the presence of Cu d at the bottom of the conduction band. Interestingly, when higher number of conduction bands are considered, the overall contribution around the conduction band edge is dominated by Cu p for pristine case (Figure 4. 16 (e)). For a Sn doped case, it's a compound effect from Sn p and Cu p orbitals (Figure 4. 16 (f)).

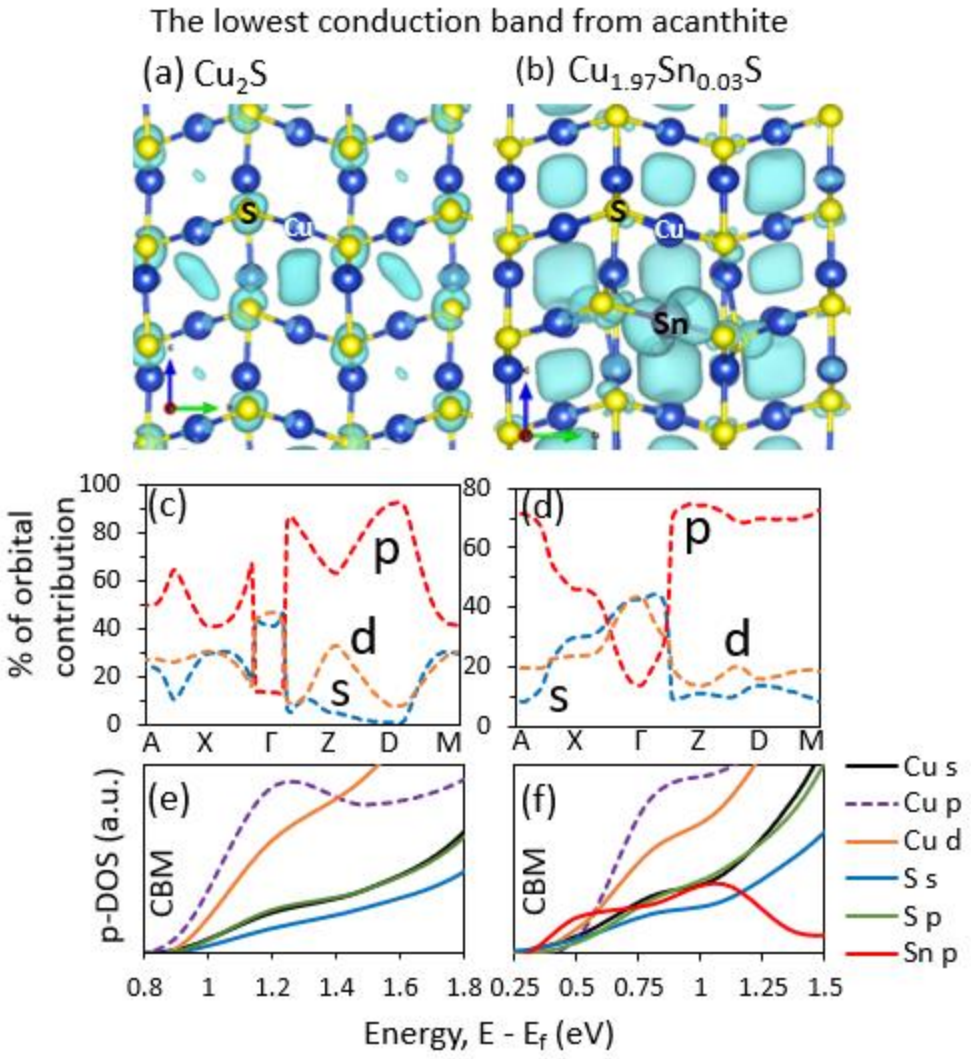

Figure 4. 16 The first conduction band from a pristine (a, c) and a Sn doped (b, d) systems are compared with help of band decomposed charge density and partial orbital contribution calculated from orbital projected wave functions. For (a) and (b) the charge density isosurface correspond to ∼25% of the maximum. (e) and (f) are the partial density of states (p-DOS) near the bottom of the conduction band for the whole pristine and a Sn doped system, respectively.

4.3.5 Cu-vacancy in $Cu_{2-x}Sn_xS$

It is well known that almost all the known phases of Cu_2S suffer from spontaneous Cu vacancy formation, and it is also evident for this acanthite phase [37,104]. In this section, we would focus on the thermodynamics and electronic structures for simultaneous Cu vacant and Sn doped structures. We considered the least and the maximum number of Sn doped structures to calculate for the Cu vacancy formation energy. To make a Cu vacancy, a Cu atom was removed from its site. Then the energy of such a relaxed structure was used to calculate for the Cu vacancy formation per supercell. The energy landscape is given in Figure 4. 17. The figure shows that Cu vacancy formation at Cu poor condition is always favorable, as expected. However, the energy for the second one is less negative which means that the second Cu vacancy in a pristine structure is less favorable than the first one even though thermodynamically, it is possible to form. Interestingly, we get two extreme scenarios for Sn doped cases. For a single Sn doped supercell, we find that the Cu vacancy formation becomes more probable than any other cases at both Cu rich and poor conditions, but this probability decreases and becomes the least for the heavily Sn-doped case, $Cu_{1.69}Sn_{0.31}S$. Such scenario was also observed for Ag doped acanthite Cu_2S as in ref. [104].

It is also well-known that Cu vacancies in pristine Cu_2S introduce p-type defects. In that case, the top of the valance band intercepts the Fermi level. However, our investigation shows that a Cu vacancy can interplay with the defect originated from Sn doping, and depending on the concentrations, the valance band edge moves closer to or

far from the Fermi level as in Figure 4. 18. This figure presents the band structures for Cu-vacancy contained Sn doped cells. When a Cu vacancy is made to a single Sn doped cell, the p-type characteristic of the system is compensated, and the top of the valance band is located just below the Fermi level. In Figure 4. 18(a), the defect band related to Sn doping is now pushed from the Fermi level to more positive energy and composed of unoccupied states only. If the number of Cu vacancy is doubled in the same cell, hole states are now found at the top of the valance band. The first defect band is relatively at the same energy state as the previous case, but a new defect like band is seen to originate at the bottom edge of the conduction band which looks like the first one. The hole states at the Fermi level due to the Cu-vacancies can now be compensated with suitable Sn-doping. Since Cu-vacancies are supposed to be found in Cu_2S due to the intrinsic nature of this material, this study indicates that Sn-doping can be a viable alternative to reduce the vacancy formation tendencies while the defect states in band structures can be mitigated with remaining Cu-vacancy states.

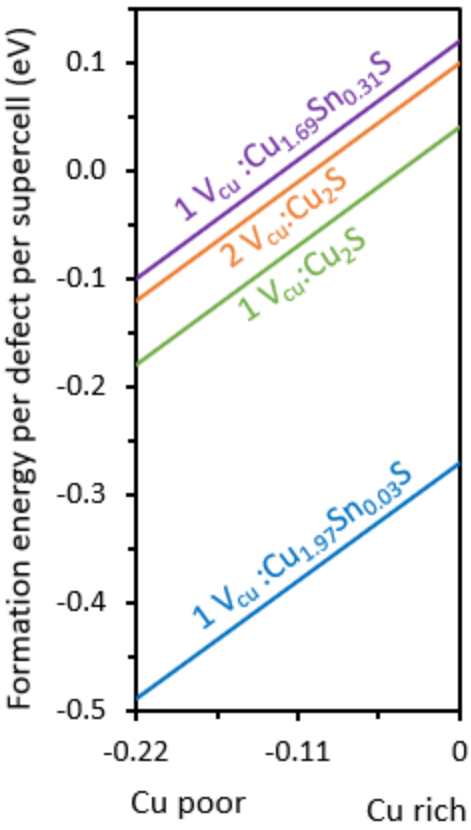

Figure 4. 17 The formation of energy per Cu vacancy in pristine and Sn doped 96 atoms supercell. The figure shows that a Cu vacancy formation is thermodynamically favorable for a pristine structure (green line) at Cu poor condition and the energy is slightly positive at Cu rich. In the same structure, a second vacancy formation (orange line) is less probable than the first one. This vacancy formation becomes highly favorable in a single Sn doped supercell (blue line) at both Cu rich and poor condition. On the other hand, for highly Sn doped case, $Cu_{1.69}Sn_{0.31}S$, Cu vacancy formation probability decreases and the least (purple line) for all the cases considered here.

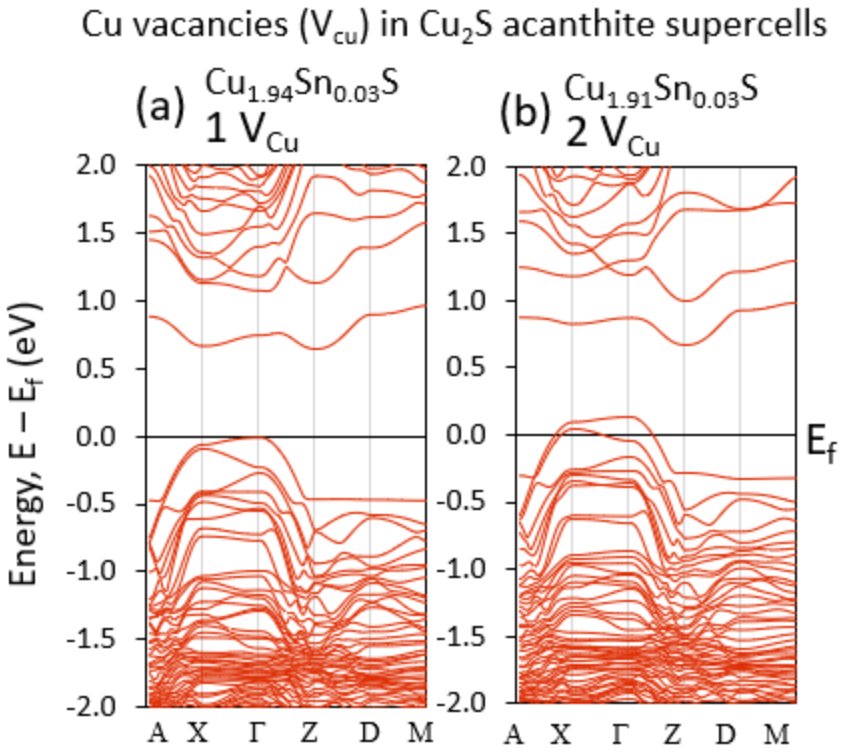

Figure 4. 18 GGA + U band structures for different number of Cu vacancy contained $Cu_{2-x}Sn_xS$. (a) and (b) for one and two Cu vacancies in a single Sn doped cell, respectively. The Fermi level is set at 0 eV. All the states below the Fermi level are occupied.

4.4 Conclusion

In summary, we have employed the first principle calculations to study the stability, electronic and optical properties of Sn doped acanthite Cu_2S. From the ab-initio molecular dynamics study we have found that there is a good structural correspondence between the low chalcocite and acanthite phases of Cu_2S at room temperature. Sn was doped in acanthite for different concentrations and in different configurations. The calculated thermodynamic landscape shows that Sn doping in acanthite phase is thermodynamically favorable. The chemical potential landscape calculation shows that the single-phase

stability zone for low concentration Sn doping is significantly large at thermodynamic growth condition. However, the single-phase stability zone area decreases as Sn doping concentration increases. Since Cu_2S phases suffer from Cu vacancy formation, we also calculated the vacancy formation energy for Sn doped systems and found that even though the Cu vacancy formation probability increases in low Sn doped system, the probability decreases with higher Sn concentration. From the electronic structures, it is found that Sn doping introduces defect bands at the Fermi level, mostly contributed by Sn *p*. The number of defect bands increases as Sn doping concentration increases and the fill in the band gap. Hence, heavily Sn doped systems show metallic characteristics. The electronic structure also shows that the *p*-type characteristic which originates due to Cu vacancy in pure Cu_2S can be compensated with suitable amount of Sn doping. In such case, the top of the valance band lies exactly below the Fermi level. Similar studies are also carried out for low chalcocite phase to some extent in this work and found that there is good correspondence for the thermodynamic properties and electronic structures with the cases of acanthite phase.

Chapter 5

Conclusion

In this dissertation, the goal was to stabilize Cu_2S against the formation of excessive Cu vacancy in the crystal and to control the diffusion of the vacancy forming Cu ions. Photovoltaic devices based on Cu_2S showed deteriorating performance over the time due to this intrinsic and spontaneous Cu vacancy formation tendency. However, the promise of this material in the photovoltaics community never fade away completely since Cu_2S has suitable bandgap energy and it consists of earth abundant, non-toxic elements. Besides, Cu_2S in single junction solar cells showed nearly 10% efficiency in the past. So, this material meets the primary criteria of being used in the arena intended for clean and renewable energy alternatives to fight the global warming and the climate change. A cost-effective solution to tackle the well-known problem of this material should enable proper usage of the p-type nature of this semiconductor as an efficient solar absorber material.

Even though Cu_2S has a simple stoichiometric composition, it's a complex material with several crystalline phases, where low chalcocite is experimentally known the most stable stoichiometric phase at or below room temperature. This phase has 96 Cu and 48 S atoms in its unit cell, where Cu atoms are distributed in 24 inequivalent symmetric sites. The Cu sites in Cu_2S are not very well defined in the low chalcocite phases. Studying a low symmetry crystal system is not very straight forward either experimentally or theoretically. Hence studying phase stabilities and modelling for related electronic properties are quite challenging. In that case, a relatively new stoichiometric phase of Cu_2S, derived computationally from crystal structure database search with density

functional theory (DFT), has an acanthite like simple crystal structure, and been found thermodynamically more stable than low chalcocite in the ground state, have shown promise to serve as a viable alternative to model for relevant Cu vacancy and diffusion studies in low chalcocite. Nowadays, DFT is the state-of-the-art method to study the ground state thermodynamic and electronic structure properties of many body quantum mechanical systems, and with the advent of sophisticated computational technologies, DFT can be implemented in supercomputing facilities with relative ease. Hence, the DFT as implemented in VASP was used as the theoretical framework for a systematic quantum mechanical study of both acanthite and low chalcocite phases of Cu_2S. Since DFT underestimates the band gaps, a post-DFT method such as DFT + U was employed to calculate the band structures and the density of states for all the necessary cases.

We have discovered good structural correspondence between the low chalcocite and acanthite crystal structures by ab initio molecular dynamics simulations at room temperature. For both structures, S atoms mainly build the frames of the crystal structures. The average nearest neighbor distances up to fifth nearest neighbor are very close even though Cu atoms in low chalcocite phase have low symmetry compared to the acanthite phase. The calculated radial distribution function (RDF) shows the atoms' overall packing follow a similar pattern except Cu atoms beyond the second nearest neighbor. After that the crystallinity of Cu in low chalcocite is very low. However, cumulative RDF shows that the total number of atoms packed in neighboring shells are similar for both structures. Such correspondence allows cost-effective and time saving computational modeling on acanthite like structure compared to low chalcocite. In

addition, the valence states of Cu in both structures have almost the same electronic signature.

To stabilize Cu_2S, our first approach was to alloy this material in its acanthite structure with suitable doping element having similar charge state as like Cu. Since acanthite Cu_2S was derived computationally from acanthite Ag_2S and both Cu and Ag possess similar charge states and belong to the same group of the periodic table, we doped Ag at Cu sites at various concentrations and searched for the thermodynamically stable crystal configurations. Reduced Cu vacancy formation tendency was found for Ag doped systems $Cu_{1.69}Ag_{0.31}S$ with higher energy band gaps than the pristine acanthite Cu_2S, which indicates the potential for higher photo-voltage efficiency as well. In addition, the calculated Cu diffusion energy barrier showed that Cu diffusion could be controlled in the Ag doped environment of the system. However, the thermodynamic calculations showed that Cu vacancy would prevail in such systems to some extent albeit in a lesser concentration compared to the pristine Cu_2S.

In the next step, we considered a cost effective alternative than Ag which would limit the Cu vacancy formation and preserve the electronic properties suitable for efficient solar absorption as well. It is worth to mention that limited Cu vacancy in Cu_2S is necessary to preserve the p-type nature for its use in photovoltaics. From the Bader charge analysis for substitutional doping at Cu sites by different element such as Zn, Sn, Bi, Nb and Ta shows that Sn has twice the charge states of Cu in Sn_{Cu}:Cu_2S. Hence a single Sn doping at a Cu site with no vacancy introduces a defect band mostly contributed by Sn *p*. On the other hand, there are unoccupied states at the top of the valence band for a Cu vacancy contained Cu_2S system. When Sn is doped near a Cu vacancy site, the

vacancy related defect at the top of the valence band is eased, which shows that suitable amount of Sn doping coupled with Cu vacancies in the crystals of Cu_2S is another viable alternative to mitigate the Cu vacancy related defects in this material. Chemical potential landscapes for Sn doping also confirmed that single phase synthesis of Sn_{Cu}:Cu_2S at low Sn doping concentrations is highly favorable. For comparison, Sn doping effects in low chalcocite were also studied where similar trends on the thermodynamics and the electronic structures were found as that in the acanthite phase.

In conclusion, a systematic theoretical study on the aspect of limiting the Cu vacancy formation in acanthite and hence the low chalcocite phase of Cu_2S by incorporating Ag ang Sn impurities is presented within the density functional theory framework. The thermodynamics and the electronic properties were studied for both pristine and defect structures which present a detail landscape of the material. The reasons as of why Ag and Sn limit the Cu vacancy formation in Cu_2S are different: while Ag improves the integrity of the structure, Sn compensates the defect states created by the Cu vacancies. A further complex alloy study for $Cu_{2-x-y}Ag_xSn_yS$ will be necessary in the future to benefit from both the features by optimizing x and y. The methodologies developed for controlling Cu vacancy formation and the diffusion should aid experimental studies as well and open new opportunity for materials based on Cu_2S to be extensively used in photovoltaics in near future.

Chapter 6

Future direction

At present, this work has considered only the bulk phases of Cu_2S. It is usual to have quantum size effect on the electronic properties of materials and since Cu_2S are used mostly for thin film PV cells, systematic theoretical studies on different thickness of Cu_2S thin film should also be carried out as well.

When thin film solar cells are made, different layers of metal oxides are used, and their heterojunction interfaces play a crucial role on the overall performance of devices. Hence, interfacial studies to determine the band off set and the detail mechanism of charge transports should be investigated carefully.

Appendix A

Electronic band structures and density of states plots for doped acanthite systems, X_{Cu}:Cu_2S (X = Ag, Zn, Sn, Bi, Nb and Ta) and calculated Bader charges states of different species in their crystal structures.

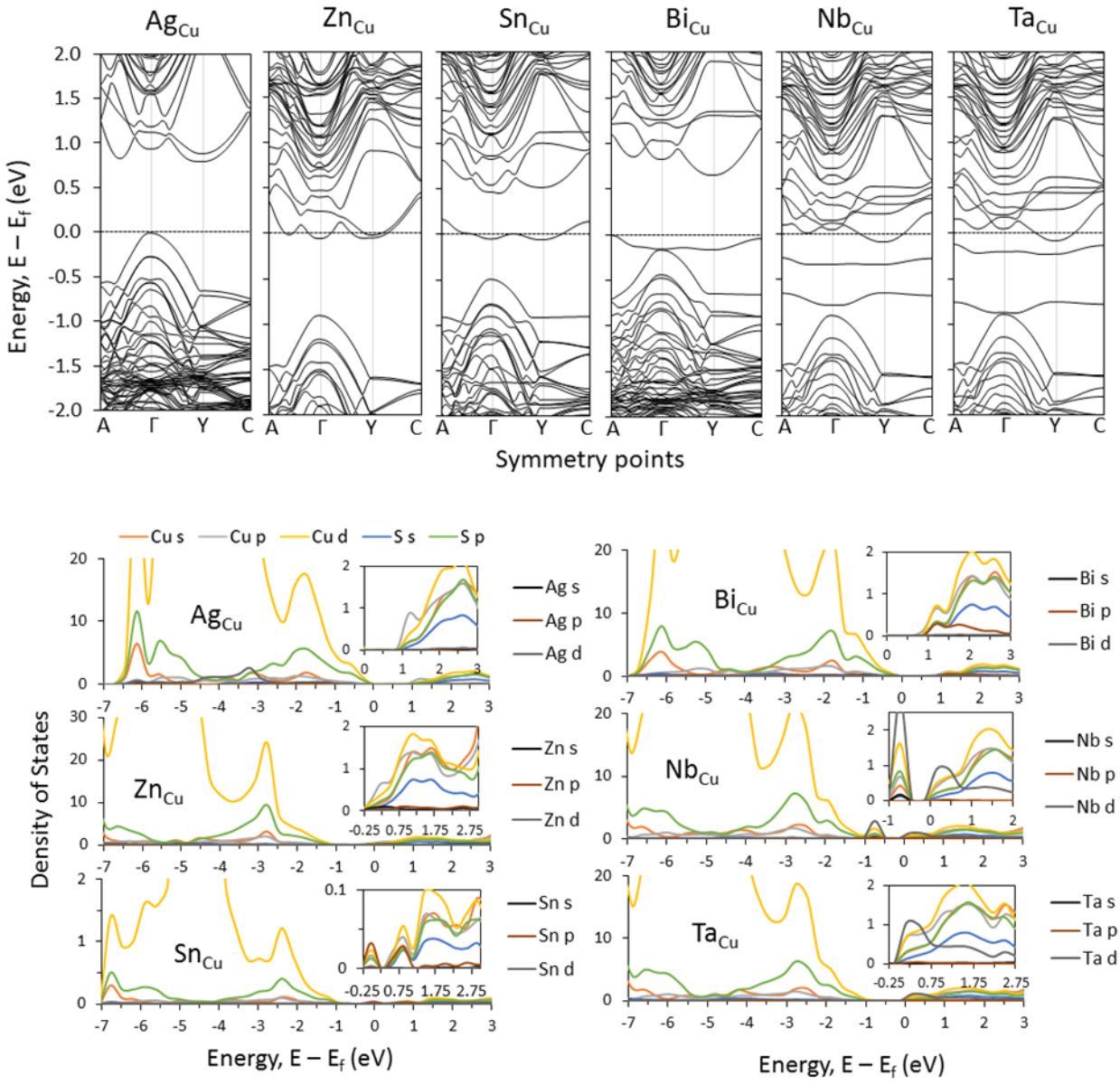

Figure 1 GGA+U calculated band structures (top) and density of states plots (bottom) for Ag, Zn, Sn, Bi, Nb, and Ta doping (Separately) of a single Cu site, denoted as X_{Cu}, in 2 × 2 × 2 supercells (64 Cu and 32 S atoms) of Cu_2S acanthite. The Fermi level is set to 0 eV. The density of states (DOS) is given in arbitrary unit. Ag_{Cu} and Zn_{Cu} introduce no intermediate or defect mid-gap states. However, the CBM in Zn_{Cu} shifts to a lower energy and intercepts the Fermi level. For Sn_{Cu}, an intermediate band is introduced at the Fermi level, which is composed of both occupied and unoccupied states. Meanwhile, Bi_{Cu} occupies a band from the CBM and moves it below the Fermi level. For Nb_{Cu} and Ta_{Cu}, the system shows near-metallic characteristics.

Table 1 Calculated average Bader charge states of different species in doped acanthite Cu_2S.

Average Bader charge states							
Cu	Ag	Zn	Sn	Bi	Nb	Ta	S
+ 0.37	+ 0.30	+ 0.71	+ 0.66	+ 0.52	+ 1.23	+ 1.28	- 0.74

Appendix B

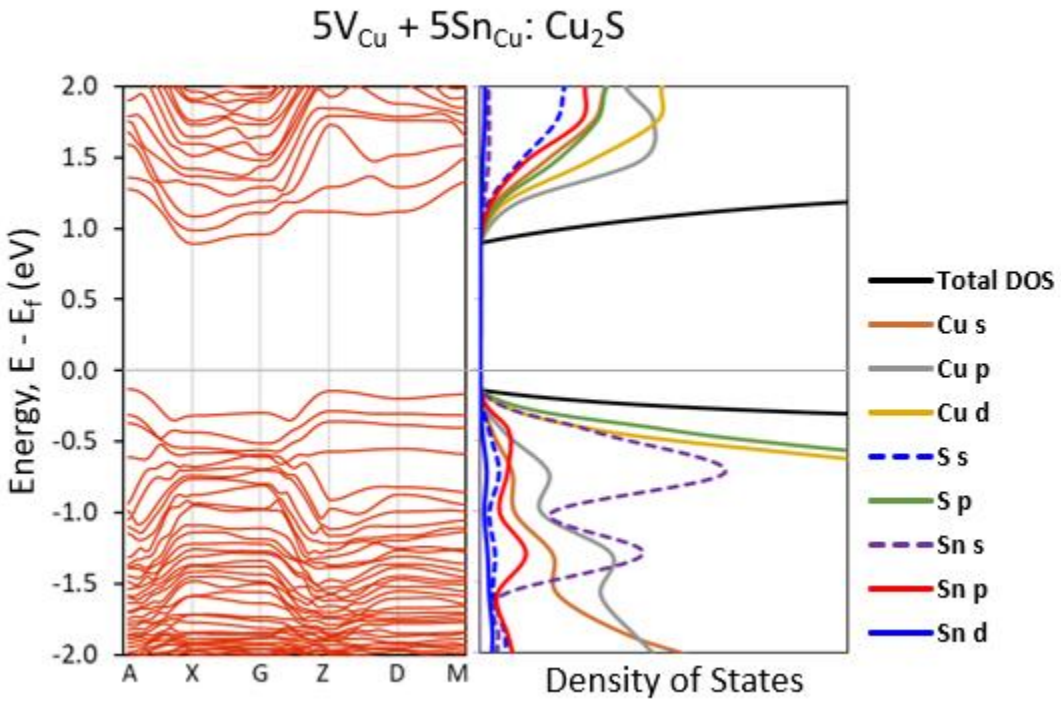

Figure 1 GGA + U (U_{eff} = 7 on Cu d and 4 on Sn p) calculated band structure and density of states of a Cu vacancy contained Sn alloyed acanthite Cu_2S system, $Cu_{1.69}Sn_{0.16}S$.

In the following appendices, abstracts for some of the projects completed alongside this dissertation work are added as supplements.

List of projects not included in the main body of this dissertation:

1. Electronic structure basis for enhanced overall water splitting photocatalysis with aluminum doped strontium titanite in natural sunlight.
   Zhao, Z., Goncalves, R., **Barman, S.K**., Willard, E.J., Byle, E., Perry, R., Wu, Z., Huda, M.N., Osterloh, F.E. **Energy Environ. Sci.**, 2019,**12**, 1385-1395 **DOI**:10.1039/C9EE00310J

2. One-step hydrogen extraction and storage in plasma generated palladium nanoparticles.
   Chaudhary, R.P., **Barman, S.K.**, Huda, M.N., Koymen, A.R. **J Nanopart Res** (2018) **20** 227 **DOI**:10.1007/s11051-018-4322-3

3. Mechanism behind the easy exfoliation of Ga_2O_3 ultra-thin film along (100) surface.
   Barman, S.K., Huda, M.N. **Phys. Status Solidi RRL** (2019) 1800554 **DOI**: 10.1002/pssr.201800554

4. Crystal structures and their electronic properties of silicon-rich silicon carbide materials by first principle calculation.
   Alkhaldi, N.D., **Barman, S.K.**, Huda, M.N. (submitted for journal publication and under peer review)

5. Photovoltaic materials design by computational studies.
   Bainglass, E., **Barman, S.K.**, Huda, M.N. (submitted for book chapter and under peer review)

Appendix C

Electronic structure basis for enhanced overall water splitting photocatalysis with aluminum doped strontium titanite in natural sunlight

Abstract

Overall water splitting with photocatalyst particles presents a potentially cost-effective pathway to hydrogen fuel, however, photocatalysts that can compete with the energy conversion efficiency of photovoltaic and photoelectrochemical cells are still lacking. Recently, Goto et al. reported (Joule, 2018, 2(3), 509–520) that Al-doped $SrTiO_3$ microparticles, followed by modification with $Rh_{2-y}Cr_yO3$ support overall water splitting with 0.4% solar to hydrogen efficiency and with 56% apparent quantum yield at 365 nm. Earlier, based on transient IR spectroscopy results, the improved activity of Al:$SrTiO_3$ had been attributed to the removal of Ti^{3+} deep recombination sites by the Al^{3+} ions. Here we use X-ray photoelectron spectroscopy to show that Al^{3+} incorporation not only reduces the Ti^{3+} concentration but also diminishes the n-type character of $SrTiO_3$ and shifts the Fermi level to more oxidizing potentials. According to DFT, the electronic structure of Al-doped $SrTiO_3$ depends sensitively on the relative locations of Al^{3+} and oxygen vacancies sites, with Al^{3+} ions next to the oxygen vacancies being most effective at suppressing the sub-band gap states. Reduced hole and electron trapping resulting from the elimination of Ti^{3+} states is confirmed by surface photovoltage spectroscopy and electrochemical scans. These findings not only provide an experimental basis for the superior water splitting activity of Al-doped $SrTiO_3$, under ultraviolet and solar irradiation, but they also suggest that aliovalent doping may be a general method to improve the solar energy conversion properties of metal oxides. Additionally, overall water splitting with a type 1 single bed particle suspension ‘baggie’ reactor under direct sunlight illumination with 0.11% solar to hydrogen efficiency is also demonstrated for the first time.

This provides a proof of concept for one of the models in the 2009 US Department of Energy Technoeconomic analysis for photoelectrochemical hydrogen production.

Appendix D

One-step hydrogen extraction and storage in plasma generated palladium nanoparticles

Abstract

This study demonstrates a novel way of hydrogen extraction from toluene and direct storage in plasma generated palladium (Pd) nanoparticles in onestep. Monodispersed Pd nanoparticles with a narrow particle-size distribution have been successfully synthesized, for the first time, by a plasma discharge between Pd electrodes in the cavitation field of toluene. The resulting well-dispersed Pd nanoparticles embedded in carbon are stabilized against agglomeration. The effect of experiment time on the particle size and the expansion of lattice spacing due to hydrogen are investigated by experimental and computational studies using density functional theory (DFT). Using X-ray diffraction and high-resolution transmission electron microscopy measurements, it was found that particle size and lattice expansion increase with experiment time. Pd nanoparticle synthesis for in situ hydrogen storage in one step using plasma discharge in an appropriate solvent emphasizes the importance of adopting this methodology which offers several advantages. These include rapid reaction rate, ability to form very small nanoparticles with narrow size distribution and hydrogen extraction from the solvent for direct storage in the Pd nanoparticle lattice.

Appendix E

Mechanism behind the easy exfoliation of Ga_2O_3 ultra-thin film along (100) surface

Abstract

The transparent wide band gap semiconductor β - Ga_2O_3 has gained wide attention due to its suitability to a wide range of applications. Despite not being a van der Waals material and having highly strong ionic bonding, the material can be mechanically cleaved and exfoliated easily along favorable surfaces to make ultra-thin layers and used in device fabrications. One of the interesting properties of this material is that thin layers preserve the pristine bulk-like electronic properties, which makes it even more promising for applications in power devices. However, very little is known about the mechanism why such ultra-thin film or even single bilayer exfoliation is favorable from the bulk. In this letter, we have explained the mechanism of such phenomenon by detailed analyses of different types of Ga – O bonding character. The protocol of methodology used and developed in this study can be utilized in general to understand bond breaking and forming of other complex materials as well. This understanding will give us a better control to fabricate thin film 2D devices.

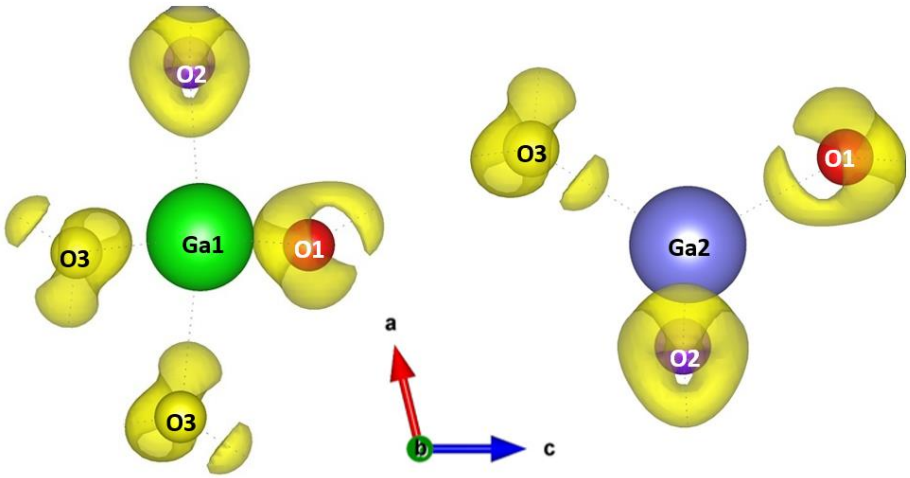

Figure 1: Positive charge density difference (isosurface value ~ 0.02 e/Å^3) for Ga_{oct} – O octahedra (Ga1 – O) and Ga_{tet} – O tetrahedra (Ga2 – O) in bulk β - Ga_2O_3. Bonds those break during exfoliations are Ga1 – O3 bonds. Ga2 – O3 and Ga2 – O1 bonds are on (100)B surface which remain unbroken. In this bulk charge density difference plot, the distinct charge accumulation in between the Ga2 – O3 and Ga2 – O1 bonds indicate their covalent nature.

Appendix F

Crystal structures and their electronic properties of silicon-rich silicon carbide materials by first principle calculation.

Abstract

Materials design for next generation solar cell technologies requires an efficient and cost-effective research approach to supplement experimental efforts. Computational research offers a theoretical guide by applying cutting edge methodologies to the study of electronic structures of newly predicted materials. In this chapter, we present a brief discussion on oxides and sulfides, two promising material groups for photovoltaic applications, and conduct a density functional theory study on two sulfide systems: acanthite Cu_2S, and S-doped triclinic $CuBiW_2O_8$. In Cu_2S, we show that Ag alloying can minimize intrinsic Cu vacancies and diffusion, as well as increase the band gap without introducing detrimental mid-gap trap states. For $CuBiW_2O_8$, we show that 50% S-in-O anion doping clustered on Cu narrows the band gap and reduces overall charge carrier effective masses with respect to the pristine cell. Results highlight the potential of sulfides as a mechanism for engineering suitable band gaps for photovoltaics.

Appendix G

Crystal structures and their electronic properties of silicon-rich silicon carbide materials by first principle calculations

Abstract

Silicon carbide has been used in a variety of applications including solar cells due to its high stability. The high bandgap of pristine SiC, necessitate nonstoichiometric silicon carbide materials to be considered to tune the band gap for efficient solar light absorptions. In this regards, thermodynamically stable Si-rich Si_xC_{1-x} materials can be used in solar cell applications without requiring the expensive pure grade silicon or pure grade silicon carbide. In this work, we have used density functional theory (DFT) to examine the stability of various polymorphs of silicon carbide such as 2H-SiC, 4H-SiC, 6H-SiC, 8H-SiC, 10H-SiC, wurtzite, naquite, and diamond structures to produce stable structures of Si-rich Si_xC_{1-x}. We have systematically replaced the carbon atoms by silicon to lower the band gap and found that the configurations of these excess silicon atoms play a significant role in the stability of Si-rich Si_xC_{1-x}. Hence, we have investigated different configurations of silicon and carbon atoms in these silicon carbide structures to obtain suitable Si_xC_{1-x} materials with tailored band gaps. The results indicate that 6H-Si_xC_{1-x} is thermodynamically the most favorable structure within the scope of this study. In addition, Si substitution for C sites in 6H-SiC enhances the solar absorption, as well as shifts the absorption spectra toward the lower photon energy region.

References

[1] U.S. Energy Inf. Adm. Mon. Energy Rev. **April**, 1 (2019).

[2] A. Marx, R. Kumar, S. Thober, O. Rakovec, N. Wanders, M. Zink, E. F. Wood, M. Pan, J. Sheffield, and L. Samaniego, Hydrol. Earth Syst. Sci. **22**, 1017 (2018).

[3] M. L. Roderick, F. Sun, W. H. Lim, and G. D. Farquhar, Hydrol. Earth Syst. Sci. **18**, 1575 (2014).

[4] J. Mika, P. Forgo, L. Lakatos, A. B. Olah, S. Rapi, and Z. Utasi, Curr. Opin. Environ. Sustain. **30**, 151 (2018).

[5] M. Pacifici, W. B. Foden, P. Visconti, J. E. M. Watson, S. H. M. Butchart, K. M. Kovacs, B. R. Scheffers, D. G. Hole, T. G. Martin, H. R. Akçakaya, R. T. Corlett, B. Huntley, D. Bickford, J. A. Carr, A. A. Hoffmann, G. F. Midgley, P. Pearce-Kelly, R. G. Pearson, S. E. Williams, S. G. Willis, B. Young, and C. Rondinini, Nat. Clim. Chang. **5**, 215 (2015).

[6] M. Burke, S. M. Hsiang, and E. Miguel, Nature **527**, 235 (2015).

[7] J. Bartholy and R. Pongrácz, Curr. Opin. Environ. Sustain. **30**, 123 (2018).

[8] N. Obradovich, R. Migliorini, S. C. Mednick, and J. H. Fowler, Sci. Adv. **3**, 1 (2017).

[9] W. Shockley and H. J. Queisser, J. Appl. Phys. **32**, 510 (1961).

[10] N. Taylor, *PV Power Measurement Compiled by Partners in the Performance FP6 Integrated Project* (2010).

[11] S. Ru, Sol. Energy **130**, 139 (2016).

[12] K. T. Fountaine, H. J. Lewerenz, and H. A. Atwater, Nat. Commun. **7**, 1 (2016).

[13] H. Döscher, J. F. Geisz, T. G. Deutsch, and J. A. Turner, Energy Environ. Sci. **7**, 2951 (2014).

[14] S. Haussener, S. Hu, C. Xiang, A. Z. Weber, and N. S. Lewis, Energy Environ. Sci. **6**, 3605 (2013).

[15] S. Hu, C. Xiang, S. Haussener, A. D. Berger, and N. S. Lewis, Energy Environ. Sci. **6**, 2984 (2013).

[16] S. Haussener, C. Xiang, J. M. Spurgeon, S. Ardo, N. S. Lewis, and A. Z. Weber, Energy Environ. Sci. **5**, 9922 (2012).

[17] M. C. Hanna and A. J. Nozik, J. Appl. Phys. **100**, (2006).

[18] J. R. Bolton, S. J. Strickler, and J. S. Connolly, 2 (1985).

[19] M. N. Huda, M. M. Al-Jassim, and J. A. Turner, J. Renew. Sustain. Energy **3**, 053101 (2011).

[20] M. A. Green, Y. Hishikawa, E. D. Dunlop, D. H. Levi, J. Hohl-Ebinger, M. Yoshita, and A. W. Y. Ho-Baillie, Prog. Photovoltaics Res. Appl. **27**, 3 (2019).

[21] I. Repins, M. A. Contreras, B. Egaas, C. DeHart, J. Scharf, C. L. Perkins, B. To, and R. Noufi, Prog. Photovoltaics Res. Appl. **16**, 235 (2008).

[22] W. Wang, M. T. Winkler, O. Gunawan, T. Gokmen, T. K. Todorov, Y. Zhu, and D. B. Mitzi, Adv. Energy Mater. **4**, 1301465 (2014).

[23] P. Sarker, M. M. Al-Jassim, and M. N. Huda, J. Appl. Phys. **117**, 035702 (2015).

[24] D. Shin, B. Saparov, and D. B. Mitzi, Adv. Energy Mater. **7**, 1602366 (2017).

[25] D. Shin, B. Saparov, T. Zhu, W. P. Huhn, V. Blum, and D. B. Mitzi, Chem. Mater. **28**, 4771 (2016).

[26] P. Roy and S. K. Srivastava, CrystEngComm **17**, 7801 (2015).

[27] A. E. Rakhshani, Solid State Electron. **29**, 7 (1986).

[28] T. Minami, Y. Nishi, and T. Miyata, Appl. Phys. Express **9**, 052301 (2016).

[29] L. C. Olsen, R. C. Bohara, and M. W. Urie, Appl. Phys. Lett. **34**, 47 (2003).

[30] R. B. Hall and J. D. Meakin, Thin Solid Films **63**, 203 (1979).

[31] H. Raebiger, S. Lany, and A. Zunger, Phys. Rev. B **76**, 045209 (2007).

[32] D. O. Scanlon, B. J. Morgan, G. W. Watson, and A. Walsh, Phys. Rev. Lett. **103**, 096405 (2009).

[33] D. O. Scanlon, B. J. Morgan, and G. W. Watson, J. Chem. Phys. **131**, (2009).

[34] J. A. Phys, **123717**, (2012).

[35] Q. Xu, B. Huang, Y. Zhao, Y. Yan, R. Noufi, and S. H. Wei, Appl. Phys. Lett. **100**, (2012).

[36] P. Lukashev, W. R. L. Lambrecht, T. Kotani, and M. van Schilfgaarde, Phys. Rev. B **76**, 195202 (2007).

[37] P. Khatri and M. N. Huda, Int. J. Photoenergy **2015**, 1 (2015).

[38] R. W. Potter, Geol. Econ. **72**, 1524 (1977).

[39] H. T. Evans, Zeitschrift Für Krist. **150**, 299 (1979).

[40] H. T. Evans, Z. Krist. **150**, 299 (1979).

[41] G. Will, E. Hinze, and A. R. M. Abdelrahman, Eur. J. Mineral. **14**, 591 (2002).

[42] K. Koto and N. Morimoto, Acta Crystallogr. Sect. B Struct. Crystallogr. Cryst. Chem. **B26**, 915 (1970).

[43] L.-W. Wang, Phys. Rev. Lett. **108**, 085703 (2012).

[44] K. W. Böer, Phys. Status Solidi **66**, 11 (1981).

[45] K. W. BÖER, Phys. Status Solidi **40**, 355 (1977).

[46] K. W. Bo¨er, J. Cryst. Growth **59**, 111 (1982).

[47] A. M. Al-dhafiri, G. J. Russell, and J. Woods, Semicond. Sci. Technol. **7**, 1052 (1992).

[48] A. B. F. Martinson, S. C. Riha, E. Thimsen, J. W. Elam, and M. J. Pellin, Energy Environ. Sci. **6**, 1868 (2013).

[49] R. E. Agbenyeke, B. K. Park, T. M. Chung, C. G. Kim, and J. H. Han, Appl. Surf. Sci. **456**, 501 (2018).

[50] R. Mandal, G. Basu, and B. Ghosh, in *Mater. Today Proc.* (Elsevier, 2018), pp. 23099–23106.

[51] M. Mousavi-Kamazani, Z. Zarghami, and M. Salavati-Niasari, J. Phys. Chem. C **120**, 2096 (2016).

[52] S. C. Riha, R. D. Schaller, D. J. Gosztola, G. P. Wiederrecht, and A. B. F. Martinson, J. Phys. Chem. Lett. **5**, 4055 (2014).

[53] M. Lotfipour, T. MacHani, D. P. Rossi, and K. E. Plass, Chem. Mater. **23**, 3032

(2011).

[54] J. Tang, Z. Huo, S. Brittman, H. Gao, and P. Yang, Nat. Nanotechnol. **6**, 568 (2011).

[55] W. Ma, A. P. Alivisatos, Y. Wu, C. Wadia, and B. Sadtler, Nano Lett. **8**, 2551 (2008).

[56] S. C. Riha, S. Jin, S. V. Baryshev, E. Thimsen, G. P. Wiederrecht, and A. B. F. Martinson, ACS Appl. Mater. Interfaces **5**, 10302 (2013).

[57] M. Patil, D. Sharma, A. Dive, S. Mahajan, and R. Sharma, Procedia Manuf. **20**, 505 (2018).

[58] E. Thimsen, U. R. Kortshagen, and E. S. Aydil, Chem. Commun. **50**, 8346 (2014).

[59] A. B. Wong, S. Brittman, Y. Yu, N. P. Dasgupta, and P. Yang, Nano Lett. **15**, 4096 (2015).

[60] D. Zimmer, J. Ruiz-Fuertes, W. Morgenroth, A. Friedrich, L. Bayarjargal, E. Haussühl, D. Santamaría-Pérez, S. Frischkorn, V. Milman, and B. Winkler, Phys. Rev. B **97**, 1 (2018).

[61] A. Mikuła and A. Koleżyński, Solid State Ionics **334**, 36 (2019).

[62] L. Zhao, F. Y. Fei, J. Wang, F. Wang, C. Wang, J. Li, J. Wang, Z. Cheng, S. Dou, and X. Wang, Sci. Rep. **7**, 1 (2017).

[63] S. Ballikaya, H. Chi, J. R. Salvador, and C. Uher, J. Mater. Chem. A **1**, 12478 (2013).

[64] T. Zhao, Y. A. Wang, Z. Y. Zhao, Q. Liu, and Q. J. Liu, Mater. Res. Express **5**,

016305 (2018).

[65] C. Du, Y. Zhao, X. Liu, and G. Shan, J. Phys. Condens. Matter **30**, 425502 (2018).

[66] Y. Zhang, B. Sa, J. Zhou, and Z. Sun, Comput. Mater. Sci. **81**, 163 (2014).

[67] A. D. Davletshina, R. A. Yakshibaev, N. N. Bikkulova, Y. M. Stepanov, and L. V. Bikkulova, Solid State Ionics **257**, 29 (2014).

[68] Y. Guo, Q. Wu, Y. Li, N. Lu, K. Mao, Y. Bai, J. Zhao, J. Wang, and X. C. Zeng, Nanoscale Horizons **4**, 223 (2019).

[69] Y. Zhang, Y. Wang, L. Xi, R. Qiu, X. Shi, P. Zhang, and W. Zhang, J. Chem. Phys. **140**, (2014).

[70] B. Li, L. Huang, G. Zhao, Z. Wei, H. Dong, W. Hu, L.-W. Wang, and J. Li, Adv. Mater. **28**, 8316 (2016).

[71] Y. Zhang, L. Xi, Y. Wang, J. Zhang, P. Zhang, and W. Zhang, Comput. Mater. Sci. **108**, 239 (2015).

[72] K. Lejaeghere, G. Bihlmayer, T. Björkman, P. Blaha, S. Blügel, V. Blum, D. Caliste, I. E. Castelli, S. J. Clark, A. Dal Corso, S. De Gironcoli, T. Deutsch, J. K. Dewhurst, I. Di Marco, C. Draxl, M. Dułak, O. Eriksson, J. A. Flores-Livas, K. F. Garrity, L. Genovese, P. Giannozzi, M. Giantomassi, S. Goedecker, X. Gonze, O. Grånäs, E. K. U. Gross, A. Gulans, F. Gygi, D. R. Hamann, P. J. Hasnip, N. A. W. Holzwarth, D. Iuşan, D. B. Jochym, F. Jollet, D. Jones, G. Kresse, K. Koepernik, E. Küçükbenli, Y. O. Kvashnin, I. L. M. Locht, S. Lubeck, M. Marsman, N. Marzari, U. Nitzsche, L. Nordström, T. Ozaki, L. Paulatto, C. J. Pickard, W. Poelmans, M. I.

J. Probert, K. Refson, M. Richter, G. M. Rignanese, S. Saha, M. Scheffler, M. Schlipf, K. Schwarz, S. Sharma, F. Tavazza, P. Thunström, A. Tkatchenko, M. Torrent, D. Vanderbilt, M. J. Van Setten, V. Van Speybroeck, J. M. Wills, J. R. Yates, G. X. Zhang, and S. Cottenier, Science (80-.). **351**, (2016).

[73] J. Heyd, G. E. Scuseria, and M. Ernzerhof, J. Chem. Phys. **118**, 8207 (2003).

[74] J. Heyd and G. E. Scuseria, J. Chem. Phys. **121**, 1187 (2004).

[75] J. Heyd, G. E. Scuseria, and M. Ernzerhof, J. Chem. Phys. **124**, 219906 (2006).

[76] A. Seidl, A. Görling, P. Vogl, J. A. Majewski, and M. Levy, Phys. Rev. B **53**, 3764 (1996).

[77] O. Access, Long-Haul Travel Motiv. by Int. Tour. to Penang **i**, 13 (2018).

[78] J. Z. A. I. Liechtenstein, V. I. Anisimov, Phys. Rev. B **52**, 5467 (1995).

[79] S. L. Dudarev, S. Y. Savrasov, C. J. Humphreys, and a. P. Sutton, Phys. Rev. B **57**, 1505 (1998).

[80] W. D. Gill and R. H. Bube, J. Appl. Phys. **41**, 3731 (1970).

[81] B. G. Caswell, G. J. Russell, and J. Woods, J. Phys. D. Appl. Phys. **8**, 1889 (1975).

[82] L. L. Kazmerski, F. R. White, G. K. Morgan, L. L. Kazmerski, F. R. White, and G. K. Morgan, Appl. Phys. Lett. **29**, 27 (1976).

[83] R. B. Hall and J. D. Meakin, Thin Solid Films **63**, 203 (1979).

[84] P. Kumar, R. Nagarajan, and R. Sarangi, J. Mater. Chem. C **1**, 2448 (2013).

[85] M. Lotfipour, T. Machani, D. P. Rossi, and K. E. Plass, Chem. Mater. **23**, 3032

(2011).

[86] T. MacHani, D. P. Rossi, B. J. Golden, E. C. Jones, M. Lotfipour, and K. E. Plass, Chem. Mater. **23**, 5491 (2011).

[87] P. Hohenberg and W. Kohn, Phys. Rev. B **136**, 864 (1964).

[88] W. Kohn and L. J. Sham, Phys. Rev. **140**, 1133 (1965).

[89] G. Kresse and J. Furthmüller, Phys. Rev. B **54**, 11169 (1996).

[90] G. Kresse and J. Furthmüller, Comput. Mater. Sci. **6**, 15 (1996).

[91] P. E. Blöchl, Phys. Rev. B **50**, 17953 (1994).

[92] M. Gajdoš, K. Hummer, G. Kresse, J. Furthmüller, and F. Bechstedt, Phys. Rev. B - Condens. Matter Mater. Phys. **73**, 1 (2006).

[93] J. Perdew, K. Burke, and Y. Wang, Phys. Rev. B **54**, 16533 (1996).

[94] V. I. Anisimov, J. Zaanen, and O. K. Andersen, Phys. Rev. B **44**, 943 (1991).

[95] S. H. Wei, Q. Xu, B. Huang, Y. Zhao, Y. Yan, and R. Noufi, Conf. Rec. IEEE Photovolt. Spec. Conf. **100**, 118 (2012).

[96] G. Liu, T. Schulmeyer, J. Brötz, A. Klein, and W. Jaegermann, Thin Solid Films **431**–**432**, 477 (2003).

[97] H. JÓNSSON, G. MILLS, and K. W. JACOBSEN, in *Class. Quantum Dyn. Condens. Phase Simulations* (WORLD SCIENTIFIC, 1998), pp. 385–404.

[98] A. C. Rastogi and S. Salkalachen, Sol. Cells **9**, 185 (1983).

[99] H. Matsumoto, N. Nakayama, K. Yamaguchi, and S. Ikegami, Jpn. J. Appl. Phys.

15, 1849 (1976).

[100] S. I. Hitoshi Matsumoto, Nobuo Nakayama, Kazufumi Yamaguchi, Jpn. J. Appl. Phys. **15**, (1976).

[101] K. W. Bo¨er, J. Cryst. Growth **59**, 111 (1982).

[102] J. A. Bragagnolo, A. M. Barnett, J. E. Phillips, R. B. Hall, A. Rothwarf, and J. D. Meakin, IEEE Trans. Electron Devices **27**, 645 (1980).

[103] R. B. Hall, R. W. Birkmire, J. E. Phillips, and J. D. Meakin, Appl. Phys. Lett. **38**, 925 (1981).

[104] S. K. Barman and M. N. Huda, J. Phys. Condens. Matter **30**, 165701 (2018).

[105] W. Kohn and L. J. Sham, Phys. Rev. **140**, A1133 (1965).

[106] D. Joubert, Phys. Rev. B - Condens. Matter Mater. Phys. **59**, 1758 (1999).

[107] J. P. Perdew, K. Burke, M. Ernzerhof, D. of Physics, and N. O. L. 70118 J. Quantum Theory Group Tulane University, Phys. Rev. Lett. **77**, 3865 (1996).

[108] S. Curtarolo, W. Setyawan, G. L. W. Hart, M. Jahnatek, R. V. Chepulskii, R. H. Taylor, S. Wang, J. Xue, K. Yang, O. Levy, M. J. Mehl, H. T. Stokes, D. O. Demchenko, and D. Morgan, Comput. Mater. Sci. **58**, 218 (2012).

[109] K. Momma and F. Izumi, J. Appl. Crystallogr. **44**, 1272 (2011).

[110] P. Sarker, M. M. Al-Jassim, and M. N. Huda, J. Appl. Phys. **117**, 035702 (2015).

[111] A. Soni, V. Gupta, C. M. Arora, A. Dashora, and B. L. Ahuja, Sol. Energy **84**, 1481 (2010).

[112] H. Chen, C.-Y. Wang, J.-T. Wang, X.-P. Hu, and S.-X. Zhou, J. Appl. Phys. **112**,

084513 (2012).

[113] S. Chen, X. G. Gong, A. Walsh, and S.-H. Wei, Appl. Phys. Lett. **94**, 041903 (2009).

[114] J. Paier, R. Asahi, A. Nagoya, and G. Kresse, Phys. Rev. B **79**, 115126 (2009).

[115] G. Henkelman, A. Arnaldsson, and H. Jónsson, Comput. Mater. Sci. **36**, 354 (2006).

[116] E. Sanville, S. D. Kenny, R. Smith, and G. Henkelman, J. Comput. Chem. (2007).

[117] W. Tang, E. Sanville, and G. Henkelman, J. Phys. Condens. Matter (2009).

[118] M. Yu and D. R. Trinkle, J. Chem. Phys. (2011).

Biographical Information

Sajib Kumar Barman received his Bachelor of Science with Honors from Department of Physics and Master of Science from Department of Theoretical Physics of University of Dhaka, Bangladesh. Then he came to USA in Fall 2011 for another Master of Science degree from Department of Physics of The University of Texas at El Paso. After successfully completing this degree, he joined the Department of Physics of The University of Texas at Arlington in Fall 2013 to start his doctoral studies. There, he worked in the theoretical condensed matter division under the supervision of Professor Muhammad Nurul Huda to study the electronic structures and crystal phase properties of various metal oxides and sulfides focusing on their efficient applications in solar cell devices. Alongside his focus, he also conducted research for hydrogen storage in palladium nanoparticles, thin film and surface properties of gallium oxides, and aluminum doped strontium titanate for enhanced water splitting in natural sunlight. For this, he collaborated with various experimental groups and completed successful projects.